

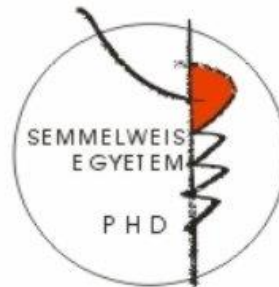
# Functional diversity and connectivity of hippocampal inhibitory cells

PhD thesis

**Viktor János Oláh**

János Szentágothai Doctoral School of Neurosciences

Semmelweis University



Supervisor: János Szabadics, Ph.D.

Official reviewers: Zita Puskár, Ph.D.  
Magor László Lőrincz, Ph.D.

Head of the Final Examination Committee: Péter Enyedi, MD, DSc

Members of the Final Examination Committee: László Köles, MD, Ph.D.  
Péter Barthó, Ph.D

Budapest  
2019

## TABLE OF CONTENTS

LIST OF ABBREVIATIONS .....	4
1. INTRODUCTION .....	8
1.1 General introduction .....	8
1.2 Hippocampal formation .....	9
1.3 The DG-CA3 interface .....	11
1.4 Characterization of hippocampal interneurons .....	17
1.5 Hippocampal cholecystinin expressing interneurons .....	20
1.6 Patch clamp electrophysiology .....	25
2. OBJECTIVES.....	28
3. METHODS .....	29
3.1 Preparation of acute brain slice for <i>in vitro</i> electrophysiology .....	29
3.2 Acute in vitro patch clamp recordings .....	30
3.2.1 Somatic recordings .....	31
3.2.2 Paired recordings .....	33
3.2.3 Dendritic patch clamp and outside-out patch recordings .....	34
3.2.4 Axonal recordings .....	37
3.3 Immunohistochemical processing .....	37
3.4 Post hoc identification of interneuronal cell types (for objective 3.2) .....	38
3.5 Morphological reconstruction .....	39
3.6 Analysis of potassium channel subunits using immunohistochemistry .....	39
3.7 Single-cell mRNA.....	41
3.8 Computational modelling.....	41
3.9 Constraining the amplifier model .....	46

3.10 Pipette parameter measurements.....	47
3.11 Validation of voltage- and current clamp model adequacy .....	48
3.12 Data analysis and statistics .....	49
4. RESULTS .....	50
4.1 Feedforward inhibition is randomly wired from individual granule cells onto CA3 pyramidal cells .....	50
4.2 Functional specification of CCK+ interneurons by alternative isoforms of Kv4.3 auxiliary subunits.....	56
4.2.1 Half of the CA3 CCK+INs show state-dependent firing.....	56
4.2.2 TOR and RS firing types do not correlate with previously known subtypes of CCK+ cells .....	59
4.2.3 Differences in low-voltage-activated potassium currents ( $I_{SA}$ ) underlie the heterogeneity of CCK+IN firing .....	62
4.2.4 Realistic models of TOR and RS firing .....	64
4.2.5 TOR cells are selectively silenced by $I_{SA}$ TOR in a narrow range of oscillatory states .....	69
4.2.6 Kv4 channels are responsible for both types of $I_{SA}$ currents in CCK+INs.....	71
4.2.7 Auxiliary subunits of Kv channels in TOR and RS cells .....	76
4.3 Small size of recorded neuronal structures constrain the accuracy of voltage measurements .....	81
4.3.1 Model implementation of extracted amplifier features .....	81
4.3.2 Pipette implementation considers the observed nonuniform $C_{pip}$ and $R_{pip}$ distributions .....	85
4.3.3 Reconstitution of the undisturbed membrane dynamics of a recorded axon .....	87

4.3.4 Distinct APs recorded from the same axon under different conditions predict similar native spike shapes .....	92
4.3.5 Instrumental and structural parameters jointly define signal distortion in recordings from small neuronal structures .....	93
5. DISCUSSION .....	97
5.1 Global thresholding of CA3 activity through FFI .....	97
5.2 Molecular mechanisms of GABAergic diversity with CA3 CCK+INs .....	101
5.3 Overcoming the limitations of voltage recordings from small neuronal structures.....	105
6. CONCLUSIONS.....	108
7. SUMMARY .....	109
8. ÖSSZEFOGLALÁS .....	110
9. REFERENCES .....	112
10. BIBLIOGRAPHY OF CANDIDATES PUBLICATIONS.....	123
11. ACKNOWLEDGEMENTS .....	124

## LIST OF ABBREVIATIONS

4-AP – 4-Aminopyridine

ACSF - Artificial cerebrospinal fluid

AIS – Axon initial segment

AP – Action potential

BB – Bridge balance

BC – Basket cell

CA1/2/3 – Cornu Ammonis 1/2/3 hippocampal regions

CB1 - Cannabinoid-receptor type 1

CC - Current clamp

$C_{\text{cell}}$  – Cellular capacitance

CCK – Cholecystokinin

CCK+IN – Cholecystokinin-expressing interneuron

$C_m$  – Specific membrane capacitance

CNQX - 6-Cyano-7-nitroquinoxaline-2,3-dione

CNS – Central Nervous System

$C_p$  - Measured membrane capacitance

CPf – Fast capacitance compensation

$C_{\text{pip}}$  - Pipette capacitance

CPN – Capacitance neutralization

$CPN_{\text{max}}$  - Maximal level of capacitance neutralization without generating voltage oscillations

CPs – Slow capacitance compensation

D-AP5 - D-(-)-2-Amino-5-phosphonopentanoic acid

DG – Dentate gyrus

DIC - Differential interference contrast

diIPSC - Disynaptic inhibitory synaptic current

DPP – Dipeptidyl peptidase-like protein

$dV/dt$  – First derivate of voltage divided by the first derivate of time

EC – Entorhinal cortex

EPSC - Excitatory postsynaptic current

$E_{rev}$  - Reversal potential

FFI - Feed-forward inhibition

FF-IN - Feed-forward inhibitory neurons

GABA - Gamma-aminobutyric acid

GC - Granule cell

$g_L$  – Passive/leak conductance

gMFB - Giant mossy fiber bouton

*hinf* - Steady-state inactivation

HpTX - Heteropodatoxin

*htau* – Inactivation time constant

$I_h$  – Current flowing through hyperpolarization activated cyclic nucleotide gated nonselective cation channel

IN – Interneuron

$I_{NA}$  - Sodium current

$I_{peak}$  – Maximal amplitude of the measured current

IPSC - Inhibitory postsynaptic currents

$I_{SA}$  – Subthreshold A-type potassium current

$I_{SARS}$  - Subthreshold A-type potassium current of cells exhibiting transient outward rectification

$I_{SA}RS$  - Subthreshold A-type potassium current of regular spiking cells

$I_{SA}TOR+RS$  – Mixed subthreshold A-type potassium current of regular spiking cells and cells exhibiting transient outward rectification

$I_{SS}$  – Amplitude of the steady-state current

KChiP – Potassium channel interacting protein

Kv – Voltage-dependent potassium channel

MF – Mossy fiber

MFA – Mossy fiber associated cell

$minf$  - Steady-state activation

MP – Membrane potential

MRF - Multiple run fitter

$mtau$  – Activation time constant

OLM - Oriens-lacunosum moleculare

PB - Na-phosphate buffer

PC – Pyramidal cell

PP - Perforant Path

PV – Parvalbumin

$R_{ax}$  - Axial resistance

$R_{input}$  - Input resistance

$R_m$  - Membrane resistance

RNA – Ribonucleic acid

$R_{OI}$  - Ratio of outer and inner diameters

$R_{pip}$  - Pipette resistance

$R_{pip}$  – Pipette resistance

RS - Regular spiking

$R_s$  - Series resistance

Satb1 - Special AT-rich sequence-binding protein-1

SCA – Schaffer-collateral associated cell

SC-RNAseq - Single cell RNA sequencing

sMFB - Small MF terminals

SR 95531 hydrobromide - 6-Imino-3-(4-methoxyphenyl)-1(6H)-pyridazinebutanoic acid hydrobromide

TEA – Tetraethylammonium

tmKChIPs - Transmembrane potassium channel interacting protein3

TOR – Transient outward rectification

TTX -tetrodotoxin

VC – Voltage clamp

VGluT3 - Vesicular Glutamate Transporter 3

$V_{step}$  - Voltage command

ZD7288 - 4-(N-Ethyl-N-phenylamino)-1,2-dimethyl-6-(methylamino)-pyrimidinium chloride

$\tau_M$  - membrane time constant



# 1. INTRODUCTION

## 1.1 General introduction

Complex behaviors require fast and efficient information processing, which is achieved in the mammalian brain by precise communication between specialized neuronal circuits. These circuits consist of distinct cell types endowed with highly specific connectivity rules enabling unique information processing capabilities (Gigg, 2006; Guzman et al., 2019; Guzman et al., 2016). However, the number of available circuit components sets an upper limit to the ability of the central nervous system (CNS) for responding to the myriad of arriving inputs, which theoretical limitation is partly overcome by the CNS by diversities between and within cell types. Neuronal diversity is well documented at level of connectivity and subcellular features as well (the number, length and complexity of subcellular processes, voltage and ligand gated channels expression and passive electrical properties). These heterogeneities can lead to substantial differences in the information processing capabilities and the impact on the network for distinct cell types, which multiplies the computational power of the whole nervous system. Therefore, to understand the physiological roles of certain brain areas, it is imperative to characterize two key features, cellular diversity and the connectivity of these circuit components.

These features of the neuronal circuits inspired my doctoral work and prompted me to investigate the wiring scheme of feed forward inhibition in the hippocampal CA3 region and to examine the physiological heterogeneities of hippocampal INs. First, we investigated the wiring arrangement of the feed-forward inhibition (FFI) originating from a single hippocampal granule cell (GC). Next, we uncovered a novel IN diversity in the firing behavior one of the major IN groups of the hippocampus, which is based on the alternative splicing of only a few genes. Finally, as most of my thesis relies on data gathered by patch clamp recordings, we investigated the technical limitations of voltage recordings using a computational approach.

## 1.2 Hippocampal formation

The hippocampus is one of the most widely studied region of the brain, due to the evolutionarily conserved architecture, the straight-forward sequential information processing in different subregions and its well-defined roles in normal behavior and pathophysiological conditions. In rodents the hippocampus, which is a double-C shaped structure (Figure 1), spans from the midline of the brain to the temporal lobe (Lorente de Nó, 1934). The two C-shaped areas are the dentate gyrus (DG) and the hippocampus proper, which can be further divided to the CA3, CA2 and CA1 regions (in the order of distance from the DG) based on morpho-functional differences. In each hippocampal region the excitatory cells representing the main functional output of the given region, form a single layer. The principal cell layers are coupled with a tightly structured laminar organization, which is divided into three main layers; the polymorph deep layer, the principal cell layer and the superficial layer. The polymorph deep layer of the hippocampus proper consists of the stratum oriens, while the superficial layer can be subdivided into the stratum lucidum (only present in the CA3), the stratum radiatum and the stratum lacunosum moleculare. Similarly, the DG has three layers; the molecular layer, the principal cell layer and a polymorphic layer (also referred to as the hilar region).

Since the first illustrations of Ramon y Cajal (Cajal, 1893), information transfer within the hippocampal formation has been traditionally considered to be largely unidirectional, taking place in a clear sequential manner between several subregions. Importantly, recent publications have shown that hippocampal regions are abundantly interconnected (Kohara et al., 2014; Scharfman, 2007; Xu et al., 2016) and these connections have a profound effect on signal processing within the hippocampal network, however these connections are out of the scope of my thesis, therefore a more simplified connectivity scheme is discussed below.

Traditionally, the DG is regarded as the gate of the hippocampus, receiving the majority of excitatory afferents arriving from the entorhinal cortex (EC). Superficial cells of the EC give rise to the perforant path (PP), which conveys processed neocortical information

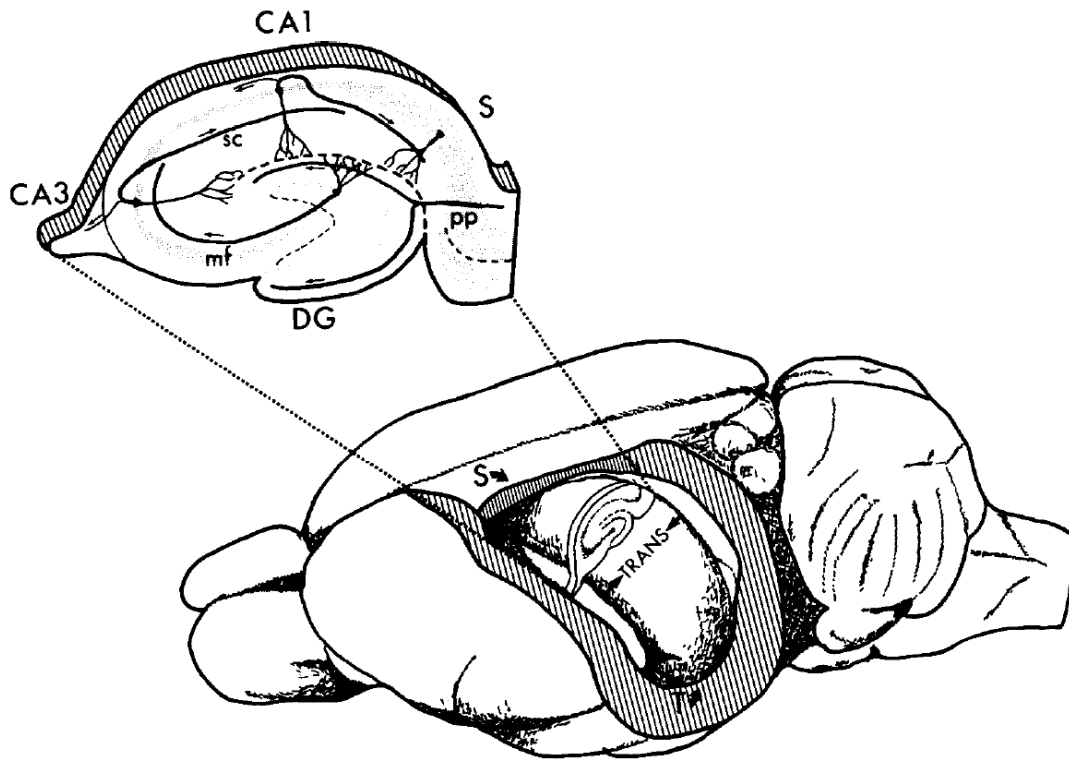


**Figure 1.** Schematic illustration of the crosssection of the hippocampus taken from approximately midway along the septotemporal axis, along with the location of the hippocampal subregions and the main excitatory fibers. Abbreviations: DG, dentate gyrus; mf, mossy fibers; pp, perforant path; SC, Schaffer collaterals; S: septal axis; T: temporal axis; TRANS: short or traverse axis. Reference: (Amaral et al., 1989)

to the DG and the entire hippocampal formation as well. However, depending on whether PP axons originate from the lateral or the medial part of the EC, they carry different information content. Specifically, the lateral EC conveys content specific information to the distal dendritic parts of the DG granule cells (DG GCs) in the outer molecular layer, while the medial EC conveys spatial information onto more proximal dendritic regions of DG GCs in the medial part of the molecular layer (Knierim et al., 2014). The output of DG GCs is an axonal fiber - termed mossy fibers (MF) – traversing through the hilar region (which separates the DG and the CA3), terminating on the proximal apical dendrites of CA3 pyramidal cells (PCs). Although the topology of these axons guarantees unidirectional information flow, as the MF system does not overlap with the dendrites of DG GCs, feedback

excitation is made possible through the involvement of hilar mossy cells (the other main excitatory cell type of the DG, which are known to directly excite (Scharfman, 1995) and disynaptically inhibit (Bilkey et al., 1987; Buzsaki et al., 1981) DG GCs). In contrast to DG GCs, CA3 PCs are known for their extensive recurrent collaterals which has important functional consequences in memory recall (Kesner, 2007). The main output of the CA3 is the Schaffer collateral system, which is one of the major excitatory inputs of the CA1 region, in addition to the EC. The main output of the hippocampus proper originates from the CA1 region of the hippocampus and conveys information to the subiculum and the EC (among other cortical and subcortical regions). Although the subiculum gives rise to axons projecting to the presubiculum and the parasubiculum, the CA1 region also projects to the EC, thereby closing the hippocampal information processing loop. As my thesis mainly focuses on the DG and the CA3 regions, the function of these hippocampal regions will be discussed later in more detail.

From a physiological perspective, the hippocampus has been a neural Rosetta Stone. The astounding discovery, that excision of the medial temporal lobe of H. M. patient resulted in relatively pure memory deficits (Scoville et al., 1957) had an unfathomable impact on the understanding of memory formation (Squire, 2009), which discovery prompted neuroscientists to look for the circuit and cellular substrate of memory in the hippocampal formation. Through the rigorous investigation of the hippocampus, this brain area has been shown to play a crucial role in memory formation (Olton, Becker, et al., 1979), spatial navigation (Olton & Paras, 1979) and furthermore, it plays a key role in Alzheimer disease (Ball, 1977), epilepsy (Scheibel et al., 1974) and schizophrenia (J. R. Stevens, 1973) as well.

### **1.3 The DG-CA3 interface**

Communication between the DG and the CA3 hippocampal regions is primarily routed through the MF pathway. The MF is an excitatory fiber bundle consisting of the axonal projections of DG GCs, with numerous side-branches in the hilar region, but with only a single main axonal branch advancing to the CA3, in the stratum lucidum. Early theoretical studies suggested that based on the anatomical features of the DG (see below), this hippocampal region is ideally suited for fulfilling network functions in specific aspects of

memory processing (E. Rolls, 1990; E. T. Rolls, 1990), which were later confirmed by physiological studies (Clelland et al., 2009; Leutgeb et al., 2007; McHugh et al., 2007). Therefore, to understand the reasons why certain features of the communication between the DG and the CA3 through the MF pathway are crucial, it is important to consider them in the context of one of their main function, the pattern separation.

Pattern separation is a term which refers to the cellular and circuit mechanisms responsible for the clear distinction of highly similar inputs and the subsequent transformation of these inputs into dissimilar output patterns (Albus, 1971; Marr, 1969), a process which is also referred to as orthogonalization. According to the Marr-Albus theory, pattern separation can be achieved by extensively divergent excitation from a small number of cells onto a much larger population (expansion coding). Although to the best of our knowledge there is no consensus about the ratio of DG GCs and the number upstream excitatory neurons, the previously mentioned prerequisite of expansion coding is not satisfied by the DG to the same extent as in other classical pattern separating circuits, such as the cerebellar cortex (Wu et al., 1999). Despite the absence of expansion coding, several other mechanisms are at their disposal for sufficient orthogonalization. One key feature of these cells is their extremely low resting membrane potential (MP, (Kowalski et al., 2016; Staley et al., 1992)), which allow them to integrate a vast amount of incoming information before they transmit signals via action potentials (AP). Additionally, extensive lateral inhibition has also been shown to limit the activity of DG GCs (Espinoza et al., 2018; Stefanelli et al., 2016). These features result in an extremely sparse DG GC firing, which enables representation of highly similar input patterns with non-overlapping cell populations. It has to be noted however, that recently the classical view suggesting that pattern separation is mediated by DG GCs came under scrutiny by papers showing that unforeseen technical limitations may have caused an underestimation of the fraction of silent cells in the DG (Diamantaki et al., 2016; Jung et al., 1993; Neunuebel et al., 2012; O'Keefe, 1976), and many *in vivo* extracellular recordings did not take into consideration the presence of the highly active mossy cells (Danielson et al., 2017; GoodSmith et al., 2017; Neunuebel et al., 2012; Senzai et al., 2017). Regardless, the basic principle of the “thresholding” effect of the resting MP and lateral inhibition persists, resulting in a unique output pattern from DG GCs. The pattern can be characterized by long silent periods, interrupted by single APs or AP bursts

(several APs elicited in high, 100-200 Hz frequency packages) of varying length (Henze et al., 2002). These bursts are thought to carry specific information (Lisman, 1997), as single presynaptic APs do not reliably translate to synaptic output of postsynaptic PCs, MF AP burst can reliably discharge them due to the robust short-term facilitation. Thereby MFs are often referred to as “conditional detonators” (Henze et al., 2002).

The aptly named mossy fibers were rigorously examined by László Acsády, who described that the two morphologically different types of terminals along these axons (Figure 2) show target-cell-specificity (Acsady et al., 1998). Accordingly, terminals that synapse onto excitatory cells are large (furthermore referred to as giant mossy fiber boutons, gMFB), ranging from 4-10  $\mu\text{m}$  in diameter, and contain ~25 active zones and several thousand vesicles (Acsady et al., 1998; Rollenhagen et al., 2007).

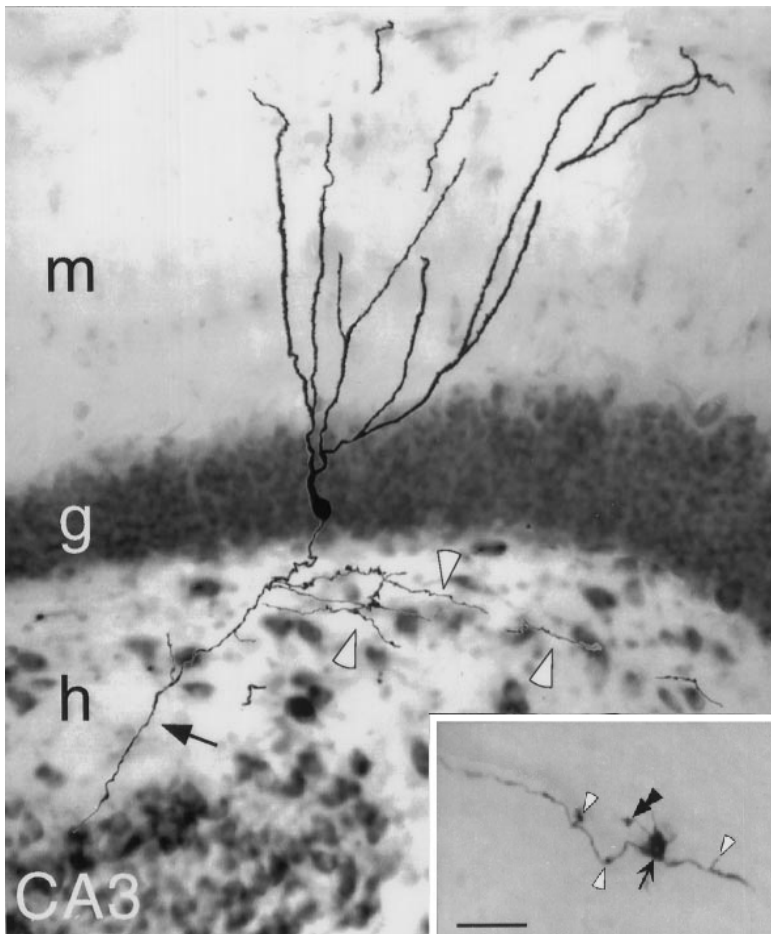


**Figure 2.** Granule cell labelled with biocytin *in vivo*. Arrow indicates mossy fiber; white arrowheads indicate local collaterals in the hilar region. *m*, Molecular layer; *g*, granule cell layer; *h*, hilus; CA3, pyramidal layer of CA3c. High magnification of a mossy terminal (arrow) in the hilar region. Double arrowhead indicates filopodial extension; white arrowheads indicate small *en passant* and drumstick-like boutons. Scale bar, 10  $\mu\text{m}$ . Modified from: (Acsady et al., 1998)

Although the release probability from a single active zone in gMFBs is low, the large number of active zones together with an enormous pool of readily releasable vesicles (~1400)

are able to generate large postsynaptic responses in the range of 5-10 mV (Urban et al., 2001; Vyleta et al., 2016). It has been shown, that release probability is inversely correlated with the facilitating nature of the synapse (Dobrunz et al., 1997; C. F. Stevens et al., 1995), which is true for the gMFB-CA3 PC synapse as well (Goussakov et al., 2000; Salin et al., 1996). The large depolarization upon a single AP coupled with the prominent facilitation of the connection and the bursting activity of the DG GCs, therefore, enables highly reliable information transfer from the DG to the CA3. In addition to the gMFBs, regular sized (0.5 - 2  $\mu\text{m}$  in diameter) axon terminals are also present along MFs, and in fact, the number of small axon terminals is higher than the number of gMFBs. Based on whether these terminals are located along the axonal branch or at the end of a smaller axonal protrusion (which is usually in the vicinity of gMFBs), they can be categorized as *en passant* and filopodial boutons respectively. Although the two types of small terminals differ in morphology, both of them innervate inhibitory neurons and so far no functional difference has been described among them. In contrast to the gMFBs, these small MF terminals (sMFB) have much less active zones and readily releasable vesicles, possibly due to spatial restrictions. The release probability at these synapses is much larger than for a single gMFB active zone (Lawrence et al., 2003), which supports reliable synaptic transmission from fewer active zones. Consequently, these connections mostly show synaptic depression (Neubrandt et al., 2018; Szabadics et al., 2009), therefore they can differently exploit the activity patterns elicited by GCs than gMFBs.

Importantly, a great disparity can be found in the number of gMFBs and sMFBs. Specifically, direct *in vivo* intracellular labelling and rigorous electron microscopic validation revealed that sMFBs are 10-times more frequent than gMFB in the CA3 region (Acsady et al., 1998), thereby establishing interneurons (INs) as the major postsynaptic targets of MF in the rat hippocampus. Taken together, although the CA3 region receives potent excitation from the DG, the activity of the MF pathway results in the powerful activation of local inhibitory cells as well, which enables dynamic control over transferred information (Mori et al., 2004).

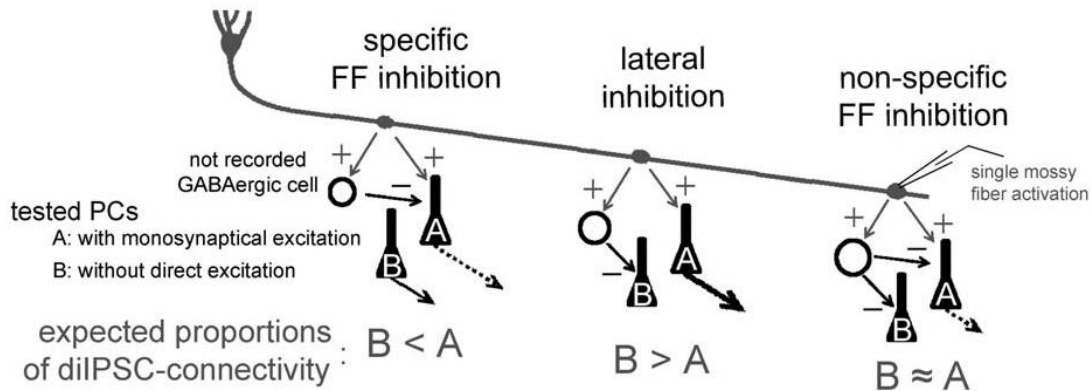


**Figure 3.** Schematic figure representing the three alternative hypotheses for the possible wiring arrangements of the DG-CA3 FFI involving individual GCs, PCs, and intermediate FF-INs with excitatory and inhibitory synaptic connections. The letters A and B depict the two PC groups, which either receive or lack monosynaptic excitation from a single MF, respectively. The expected relationships between the relative proportions of pairs with disynaptic inhibitory connections in the three wiring schemes are shown below (e.g.,  $B < A$ ,  $B > A$ ,  $B \approx A$ ). Thicker or, dashed arrows, or the absence of arrows originating from the PCs indicate stronger, temporally structured, or inhibited CA3 PC output, respectively. diIPSC: disynaptic inhibitory postsynaptic current

The DG – CA3 interface is a prototypical feed-forward inhibitory circuit due to the mainly unidirectional excitation, the preferred innervation of inhibitory neurons over excitatory cells and the physiological characteristics of the MF pathway described above, which suggests that in the CA3, local GABAergic (types of cells using gamma-aminobutyric acid – GABA as a neurotransmitter) INs have a prominent role in shaping the excitation arriving from GCs onto CA3 PCs (Acsady et al., 1998; Henze et al., 2002; Lawrence et al., 2004; Szabadics et al., 2009; Toth et al., 2000). Due to the different functional implications to whether single GC triggered FFI prefers or avoids the PCs that are directly innervated by the same MF, it is important to establish the wiring scheme of DG-CA3 FFI system. Accordingly, three possible connectivity arrangements exist, all of which could support different physiological functions (Figure 3) (Acsady et al., 2007).

First, FFI and direct excitation from a single GC can converge onto the same population of CA3 PCs. The ensemble-specific innervation would result in a precise temporal modulation of specific information transmission (Pouille et al., 2001) from the DG to the



CA3, due to the synaptic delay imposed by the disynaptic loop of the FFI. It has to be noted however, that the different short-term plasticity mechanisms present in sMFB and gMFB synapses would, in theory counteract the temporal precision, as the facilitating excitation could only slowly counter the depressing inhibition, thereby resulting in a delayed activation of CA3 PCs. The second possibility is called lateral inhibition, which is a widely used term for innervation schemes where feed-forward inhibitory neurons (FF-INs) specifically avoid the innervation of PCs that share the same excitatory source (Espinoza et al., 2018; Stefanelli et al., 2016). The silencing of neighbouring PCs and the lack of temporally aligned inhibition onto the excited ones therefore leads to potent excitation of a selected few PCs. Although lateral inhibition is an arrangement that is favourable in relay-type synapses, where the main purpose of the connection is the uncompromised information transmission, this wiring scheme leaves little-to-no room for possible plasticity mechanisms offered by other participants of the microcircuitry. Finally, FF-INs might nonselectively innervate their targets, with no considerations to the possible shared inputs, thereby dynamically setting the level of excitability of a large population of CA3 PCs (Ferrante et al., 2009; Pouille et al., 2001). The nonselective innervation arrangement has the lowest developmental cost, as no specific rules need to be taken into consideration during synapse formation. Furthermore, by utilizing the local IN circuit, a plethora of plasticity mechanisms can finely tune the system to a desired state that can be governed by ongoing activity. Despite the functional implications these possibilities carry, we currently have no information regarding the governing elementary rules of FFI at the DG-CA3 interface.

Taken together, the significantly different functional implications of different wiring schemes was our motivation with my colleagues to identify the predominant FFI connectivity imposed by single GCs onto CA3 PCs.

## 1.4 Characterization of hippocampal interneurons

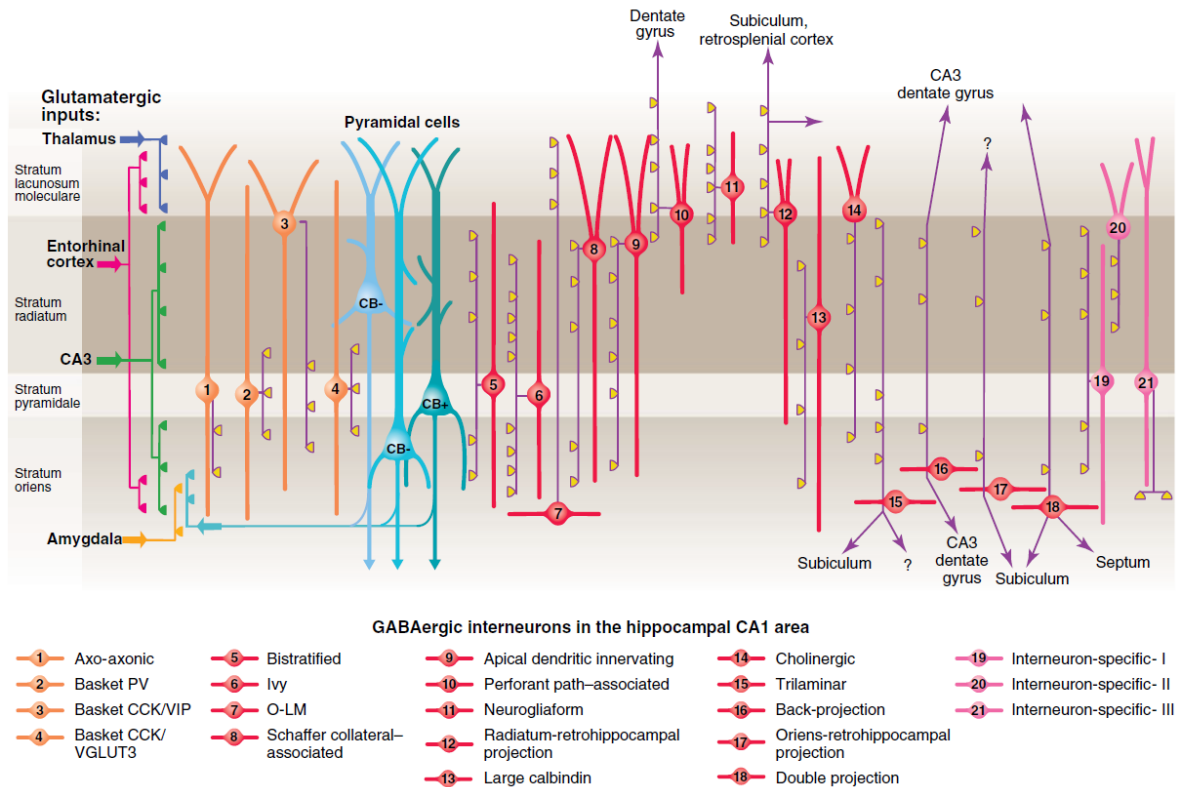


**Figure 4.** Three types of PCs are accompanied by at least 21 classes of IN in the hippocampal CA1 area. The main termination of five glutamatergic inputs are indicated on the left. The somata and dendrites of INs innervating PCs (blue) are orange, and those innervating mainly other INs are pink. Axons are purple; the main synaptic terminations are yellow. Note the association of the output synapses of different IN types with the perisomatic region (left) and either the Schaffer collateral/commissural or the entorhinal pathway termination zones (right), respectively. VIP, vasoactive intestinal polypeptide; VGLUT, vesicular glutamate transporter; O-LM, oriens lacunosum moleculare. Reference: (Klausberger et al., 2008)

To harness on the full operational potential of the aforementioned FFI circuit, a functionally diverse population of GABAergic INs is needed, from which presynaptic cells can dynamically select the optimal subpopulation for given tasks. In the hippocampus GABAergic inhibitory neurons represent only 10-15% of the local cell population, however, the remarkable physiological and anatomical diversity of these cells allow them to precisely control various aspects of circuit and cellular functions (Figure 4) (Klausberger et al., 2003; Klausberger et al., 2008; P. Somogyi et al., 2005).

For the unambiguous description of IN cell types, it is widely accepted to consider various anatomical, molecular and physiological features of GABAergic neurons (Ascoli et al., 2008). The combinatorial use of these methods is necessary, as neither of these methods can unequivocally differentiate between the more than twenty different inhibitory cell types that is described in the hippocampus (Klausberger et al., 2008).

Classification of INs based on anatomical features mainly focuses on the axonal arborization of these cells as the termination zone of their output can serve as a general indication for the function of a given cell (Klausberger et al., 2008; P. Somogyi et al., 2005). In case of the hippocampus, differences in the axonal arborisation for a given IN can be clearly defined due to the previously mentioned layered structure of the hippocampus. These layers contain different subcellular compartments of the principal cells, therefore layer-specific innervation of certain INs can either limit the availability of information from certain inputs (Klausberger, 2009; Leão et al., 2012; Miles et al., 1996; Royer et al., 2012), or regulate the general excitability of their target PCs (Miles et al., 1996; Pouille et al., 2001; Royer et al., 2012). Accordingly, INs can be subdivided into dendrite-targeting, soma- (or somatodendritic domain) targeting and axon initial segment targeting cells. The innervation of the somatic region (for example by basket cells – (Cajal, 1893; Lorente de Nó, 1934)) and the axon initial segment (by axo-axonic or otherwise known as “chandelier” cells – (Gulyás et al., 1993; Szentagothai et al., 1974)) has profound effects on the output of the target cell (Cobb et al., 1995; Szabadics et al., 2006; Veres et al., 2014). These subcellular regions are responsible for the final integration steps of all incoming information and the conversion of these inputs into an AP. Therefore, inhibition of these compartments in a large population of principal cells can have a profound effect on the timing and synchronization of APs, as well as the number of APs (Buhl et al., 1994; Cobb et al., 1995; Pouille et al., 2001). The distal dendritic branches of principal cells on the other hand - which are innervated by dendrite targeting INs - are regarded as distinct computational units, capable of generating regenerative electrical signals that propagate to the soma far more efficiently than passive signals (Branco et al., 2010; Larkum et al., 2009; Major et al., 2013). Dendrite targeting INs, such as oriens-lacunosum moleculare INs (OLM cells - (Cajal, 1893; Lorente de Nó, 1934)) inhibit this subcellular compartment, and can substantially raise the threshold for dendritic regenerative events, therefore limiting the influence of excitatory events arriving to distal

dendritic segment (in case of one of the major distal-dendrite-targeting IN types of the CA1 - the OLM cells-, the inputs from the EC – (Kepecs et al., 2014; Leão et al., 2012; Lovett-Barron et al., 2014)).

Physiological characterization of certain cell-types relies mainly on the discharge pattern of *in vitro* electrophysiologically recorded cells in response to square pulse current injection. From these firing patterns standardized parameters of the recorded action potentials (such as AP width, peak, threshold, etc.) can be measured and some of these features can clearly delineate a defined subpopulation of INs, such as the extremely narrow AP halfwidth of parvalbumin (PV) expressing INs. Although physiological characterization can be useful for comparing certain IN types (Hosp et al., 2014), it has been shown that even when two IN types can be distinguished in one region of the hippocampus, they can be regarded as a homogenous population in others (cholecystokinin+ basket cells and Schaffer Collateral Associated cells can be reliably distinguished based on the amplitude of rebound depolarization in the CA1, while they behave similarly in the CA3 (Evstratova et al., 2011; Szabó et al., 2014)). The ambiguity of physiological cell type characterization originates from the immense repertoire of discharge patterns that has been characterized in the hippocampus, most of which cannot be clearly assigned to specific IN types. Therefore, physiological characterization is best used in conjunction with other types of classifications.

Similar to morphological and physiological features, the molecular content-based classification of cell types rarely be used to identify IN types (for example in case of the presence of Satb1 and PV, for the identification of axo-axonic cells in the CA3 region (Viney et al., 2013)), rather it is used to delineate IN groups (i.e. a cluster of IN types) based on the presence of a molecular marker. Traditionally, these molecular markers included calcium binding proteins (for example PV and calbindin), neuropeptides (such as cholecystokinin - CCK and somatostatin), and many others, however the set of molecules that can characterize distinct cell types is rapidly extending, due to recent advancements in the field of RNA sequencing, which allows quick and comprehensive estimation of the whole transcriptome of neuronal cells (Monyer et al., 2004). It has to be noted however, that although independent application of morphological, physiological and molecular content-based classifications is useful in the majority of cases for identifying specific groups of INs, their combined

application is necessary for unequivocal characterization of all described cell types. As such, one interesting example for this is the existence of two types of functionally distinct basket cells (BC) in the hippocampus (Klausberger et al., 2005). Both of these cell types specifically innervate the soma of their target cells with multiple terminals, establishing a basket-shaped axonal envelop (Cajal, 1893; Lorente de N6, 1934). Despite the similar morphology, they can be properly discriminated by immunohistochemical labelling against either CCK or PV, or by looking at their firing pattern. PV positive BCs fire at high frequencies, therefore they are otherwise known as fast-spiking BCs, while CCK positive BCs discharge at substantially lower frequencies. Taken together, several methods can be used to distinguish between certain groups of cells in the hippocampus, such as the morphology-, anatomical marker- and physiology-based characterization, the combined application of these techniques is needed for reliable distinction of all the heterogeneous cell types of the hippocampus.

### **1.5 Hippocampal cholecystokinin expressing interneurons**

A prominent fraction of hippocampal INs expressing cholecystokinin (CCK+IN) forms a physiologically homogenous, yet anatomically heterogeneous IN subpopulation (Szab6 et al., 2014). The morphological diversity of these cells is most discernible at the level of their axonal arborisation. The collective output of the CCK+IN cell population covers all of the hippocampal sublayers, thereby controlling every key subcellular compartment of their target PCs besides the axon (Tamas F Freund et al., 1996; Klausberger et al., 2008; P. Somogyi et al., 2005). Accordingly, we can distinguish classical soma targeting BCs (DeFelipe et al., 1986), proximal dendrite targeting mossy fiber associated cells (MFA (Vida

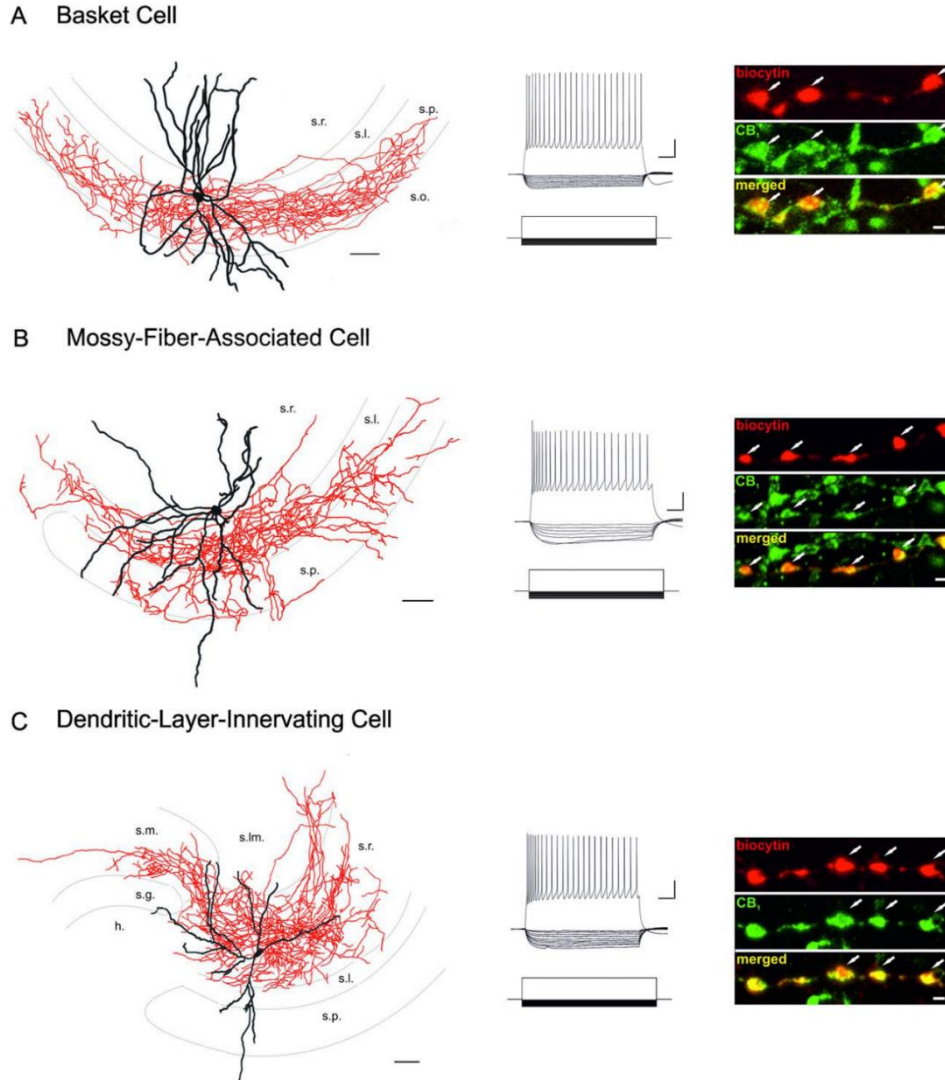


**Figure 5.** Three typical CB1-expressing INs; basket cells, mossy fiber-associated cells and dendritic-layer-innervating cells. In the camera lucida reconstructions of these neuron types, the cell bodies and the dendrites are shown in black, while the axon collaterals are in red (scale bars: 50  $\mu$ m). For each example, voltage responses to depolarizing (300 pA) and hyperpolarizing current steps (from 210 to 2100 pA in increments of 10 pA) are indicated (calibrations, 20 mV, 100 ms). In each case, CB1 expression was confirmed in their axon collaterals intracellularly labeled with biocytin (scale bars, 1 mm). s.lm.: stratum lacunosum-moleculare; s.r.: stratum radiatum; s.l.: stratum lucidum; s.p.: stratum pyramidale; s.o.: stratum oriens; s.m.: stratum moleculare; s.g.: stratum granulosum; h.: hilus. Modified from: (Szabó et al., 2014)

et al., 2000), present only in the CA3 region, as MFAs selectively innervate the proximal dendritic region of the CA3 in the stratum lucidum, which layer is missing from other

hippocampal areas), and several dendrite targeting cell types, such as Schaffer-collateral associated cells (SCA: whose axonal projections co-align with glutamatergic inputs from the CA3, therefore ramifying primarily in the stratum radiatum and to a lesser extent in the stratum oriens (Cope et al., 2002)). Despite these clear differences in the projection pattern of CCK+INs, their physiological properties are largely similar (Figure 5) (Lasztóczy et al., 2011; Szabó et al., 2014).

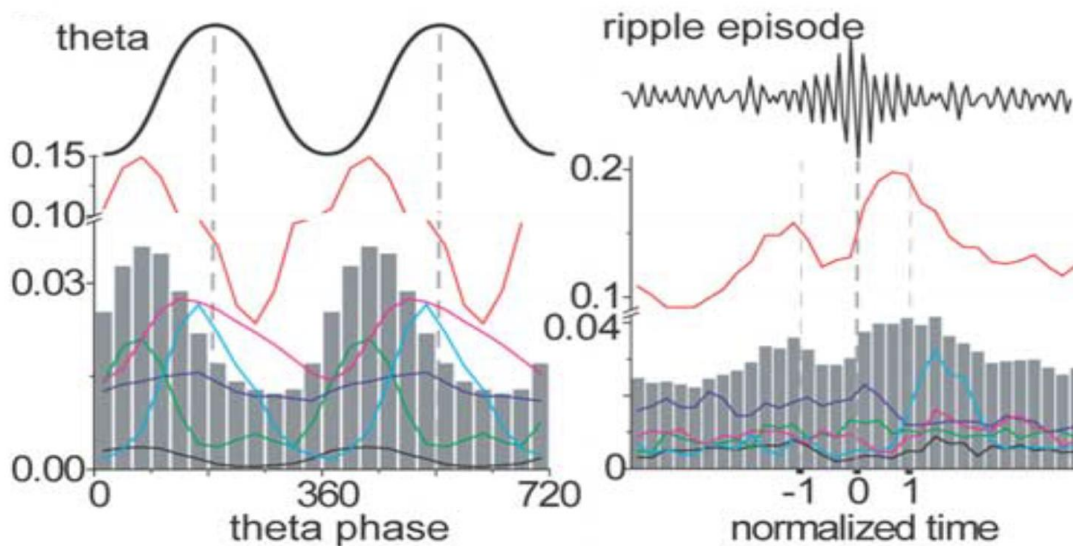


**Figure 6.** The firing probability of six CCK+ *in vivo*-recorded cells (color traces) is shown during theta oscillation (6-12 Hz network oscillation) and ripple oscillations (fast network synchronization around 120-200 Hz); the mean is shown as gray columns. Note the large differences in the baseline firing, peak firing and the firing preference (with regards to the phase of the theta cycle indicated by the x axis of the left panel) of individual cells. Reference: (Klausberger et al., 2005)

A comprehensive study regarding the physiological features of these cells found that most of the passive (input resistance) and active cellular properties (AP amplitude, AHP amplitude etc.) were indistinguishable among *in vitro* recorded and identified BCs, MFAs, SCAs and performant path associated cells. Specifically, their firing is believed to be always falling into the regular firing properties, which include intermediate AP widths (between that of PCs and classical fast-spiking INs) and clear spike frequency accommodation (Cea-del Rio et al., 2011; Glickfeld et al., 2006; Szabadics et al., 2009). These excitability parameters

can be crucial for the generation of unique activity patterns during various circuit oscillatory states.

Despite these similarities, several *in vivo* recordings suggested, that individual CCK+INs are differentially active during various oscillatory states, with distinctive preference for lower or higher frequency ranges (Figure 6) (Klausberger et al., 2005; Lasztóczy et al., 2011) .

An important functional distinguishing factor between CCK+INs and other major IN types is the enrichment of axon terminals with cannabinoid-receptor type 1 (CB1, (Tamás F Freund et al., 2007)). CB1 receptor provides a delicate feedback control over synaptic release by the regulation of individual synapses in an activity-dependent manner (Katona et al., 1999; S.-H. Lee et al., 2010; Neu et al., 2007; Ohno-Shosaku et al., 2001; Wilson, Kunos, et al., 2001; Wilson & Nicoll, 2001). A good example for the influence of CB1 dependent modulation can be observed in the case of MFA – CA3 PC connections (Losonczy et al., 2004). During the testing of MFA – CA3 PC synaptic connection, high frequency stimulation of the presynaptic partner is needed, because of the lack of detectable postsynaptic response upon low frequency stimulation (< 25 Hz), in contrast to when the same MFA cell is discharged at higher frequencies (50-100 Hz). Cannabinoid receptor antagonists, however convert these “mute” synapses into high-fidelity ones suggesting that selective, activity dependent regulation of specific GABAergic INs is achieved by presynaptic cannabinoid receptor activation.

In addition to the powerful self-regulatory mechanism of CCK+INs by presynaptic CB1 receptor activation, their transmitter release machinery has functionally important and uniquely distinctive features as well. The precision of transmitter release is an important determinant of the functional impact of a given IN on its target cells (Stanley, 2016). Most synapses in the CNS release transmitter in a tightly synchronised (phasic) manner after a presynaptic AP (Bucurenciu et al., 2008; Eggermann et al., 2012), however CCK+INs have been shown to release GABA asynchronously as well, meaning that transmitter can be released after APs for an extended time period (Hefft et al., 2005). Fast “phasic” synapses (Bartos et al., 2002) are generally thought to synchronise the activity of principal populations and therefore contribute to high-frequency oscillations (Bartos et al., 2007), whereas slower



“tonic” inhibition has a modulatory effect on the general excitability of the innervated cells, by setting the gain or offset of the input-output relationship of postsynaptic target cells (Farrant et al., 2005). Therefore, the asynchronous transmitter release from CCK+INs, which can generate long lasting inhibition, is ideally suited for the postsynaptic gain control.

Concerning the circuit function of CCK+INs, several important discoveries have been made recently, which confirms the role of these cells as highly sensitive fine-tuning devices. First, CCK+INs in general are preferentially active during low frequency network oscillations (theta rhythm: 6-12 Hz, (P. Somogyi et al., 2005)) and their silencing has only a minor effect on network oscillatory dynamics at high frequency states (del Pino et al., 2017). Second, they receive a far less efficient excitatory drive from local sources, compared to classical fast spiking BCs (Gulyás et al., 1999), however they are exposed to modulatory effects of extrinsic inputs. These inputs include serotonergic modulation from the median raphe (Férezou et al., 2002) and cholinergic modulation from the medial septum – diagonal band of Broca (File et al., 2000). Due to the tonic nature of the inhibitory output of CCK+INs and the various neuromodulatory systems converging to these cells, it was hypothesised, that they are much more sensitive to the emotional, motivational and general physiological state of the animal (Tamás F Freund, 2003). This hypothesis is supported by the presence of CB1 cannabinoid receptors, which are specifically expressed by CCK+INs as it is widely known that cannabinoid ligands in specific concentrations have an anxiolytic effect (Fabre et al., 1981). Altogether, CCK+INs in the hippocampus consists of anatomically heterogeneous cell types, exerting their action through tonic inhibition of principal cells. As a result of the automodulatory effect of CB1 receptors and the convergence of subcortical neuromodulatory inputs, CCK+INs are ideally suited to dynamically control a subset of principal cells by inhibiting them based on the context of ongoing activity.

In recent decades a plethora of scientific studies reported within-cell heterogeneities of principal cells, for example in case of the CA3 and CA1 PCs ((Danielson et al., 2016; Graves et al., 2012; Hunt et al., 2018; H. Lee et al., 2015), for review see (Cembrowski et al., 2019)). Focusing on hippocampal INs, the aforementioned anatomically diverse population of CCK+ INs are ideally suited to investigate question of cell type boundaries. Hints for functional diversity came from publications showing that CCK+INs are differentially active during various network oscillatory states (Klausberger et al., 2005; Lasztóczy et al., 2011).

Therefore, our aim was to investigate the CCK+INs from a larger perspective, beyond the standard recording conditions used for physiological characterization, to see whether a previously undescribed functional diversity can make them suitable for specific physiological roles.

## **1.6 Patch clamp electrophysiology**

The availability of techniques largely constrains our understanding of biological systems. In the advent of modern neuroscience the squid axon (Cole et al., 1939; Cole et al., 1960) or giant snail neurons (Amoroso et al., 1964) were chosen for studying basic mechanisms of electrical excitability using rudimentary electrophysiological techniques, such as silver vires thrust down the axis of the axon and early versions of intracellular microelectrodes. The ground-breaking work of Erwin Neher and Bert Sakmann (Neher et al., 1976) however opened a new horizon in the field of neuroscience by the development of the patch-clamp technique (Figure 7), which allowed the investigation of rules that govern neuronal communication between connected cells, to explore the signal processing of excitable cells and the previously discussed (section 2.4) functional characterization of neurons. Patch clamp relies on the accessibility of cellular compartments and membranes by direct targeting of these with a glass pipette containing a measuring electrode and filled with appropriate recording solution, under microscopic supervision. In these recording conditions either the membrane voltage (current clamp) or ionic currents (voltage clamp) can be monitored. By the early 1990s, the general familiarity with the constraints of the technique, together with advancements made in the field of optics and microscopy allowed targeting small, subcellular processes (Davie et al., 2006; Stuart et al., 1993; Usowicz et al., 1992), which was an important step toward the understanding of the neuronal behavior, because the dendritic (Branco et al., 2010) and axonal compartment (Alle et al., 2006; Sasaki, 2013; Shu

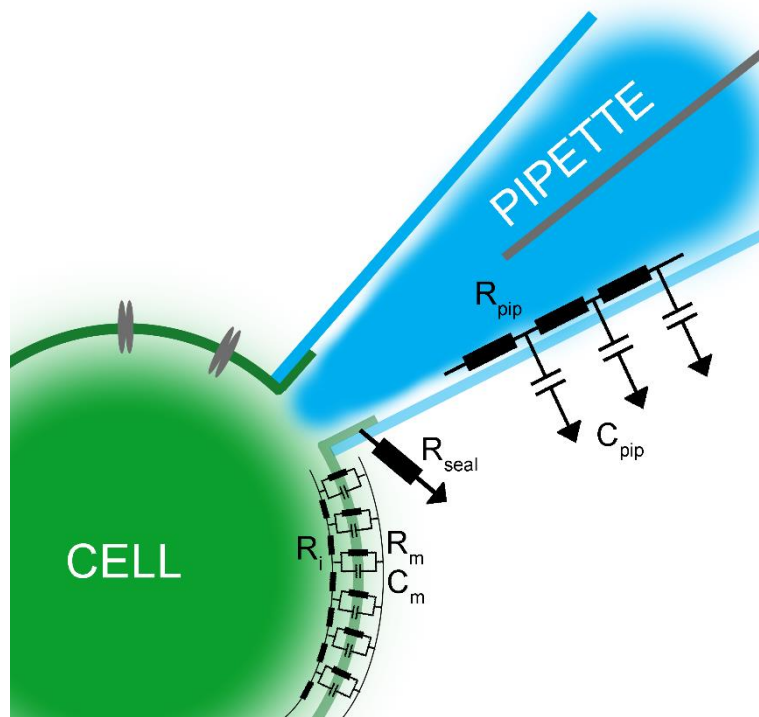


**Figure 7.** *Passive electrical environment of the whole cell patch-clamp configuration*

In case of recording from small structures, the recorded signal can be distorted by the significant contribution of pipette components.  $R_{ax}$  : intracellular or axial resistance,  $R_m$  : membrane resistance,  $C_m$  : membrane capacitance,  $R_{pip}$  : pipette resistance,  $C_{pip}$  : pipette capacitance

et al., 2006) of a given cell can act as an independent computational unit, which cannot be explored in full extent based on somatic recordings (Rall et al., 1985).

Although the importance of recordings from small neuronal compartments is indisputable in the understanding of the cellular level neuronal functions, similarly to all measuring methods, patch clamp technique has its own limitations. These limitations mostly arise from the physiological properties of the pipette, namely the resistance and substantial capacitive surface. The presence of these electrical components can distort electrical signals in two different ways. First, the pipette resistance ( $R_{pip}$ ) and pipette capacitance ( $C_{pip}$ ) acts as a low-pass filter, which restricts the frequency domain in which signals can be measured accurately. Second, due to the direct connection between the measured surface and the recording pipette, the whole electrical measuring system is electrically merged with the

recorded structure, thereby substantially altering the local passive environment and the native signal genesis. In somatic recordings the measurement error is negligible due to the overwhelming contribution of structural capacitance and resistance to the electrically merged “circuit”. However, in case of subcellular recordings structural passive parameters are proportional to the pipette, causing substantially altered local excitability.

Axons were traditionally regarded as simple relays possessing exclusively the role of the precise and efficient conduction of thresholded MP information in a form of an AP. However, using direct axonal recordings, researchers have challenged this view by demonstrating several cellular and circuit mechanisms for the activity dependent modulation of the transmitted axonal signal, resulting in a hybrid information transfer that include information about the state of the presynaptic cell (Alle et al., 2006; Sasaki, 2013; Shu et al., 2006). These direct recordings are crucial for understanding neuronal communication, however they are exceptionally sensitive for the previously mentioned distortions of patch clamp recordings due to the particularly small axonal surface, large structural resistance and the extremely fast AP waveform. Previously it was shown that it is possible to correct for the filtering effects of the pipette offline if we knew the frequency profile of the filter formed by the recording instrumentation (Brette et al., 2008; Jayant et al., 2017). However, offline correction for the disruption of the local electrical environment is more challenging because this large effect depends on the recorded structure. However, theoretically it is possible to recover the native electrical signal from heavily disturbed MP measurements if the precise morphological and electrical features of the recorded structure and the phenomenologic behavior of the recording instrumentation is known. Therefore, my third aim was to build a computational model that combines these features and allows for the correction of distorted recordings from small biological structures.

## 2. OBJECTIVES

**2.1** The first goal of my PhD thesis was to investigate the wiring scheme of the feedforward inhibition arriving from the DG to the CA3 hippocampal region. For this goal, we used *in vitro* whole cell patch clamp recordings from giant mossy fiber terminals and CA3 PCs simultaneously in acute brain slices of Wistar rats. To identify the fundamental connectivity rules, we directly compared the portion of PCs which received monosynaptic excitation and disynaptic inhibition from the same presynaptic MF to the portion of PCs receiving only disynaptic inhibition.

**2.2** The second goal of my thesis was to address the question of boundaries of interneuronal cell classes from a broad perspective, including genes, molecular content, morphology, excitability and potential contributions to specific physiological functions. We focused on one of the most numerous and diverse inhibitory cell class of the CA3 region, the CCK+ INs, as these cells are heterogeneous in anatomical terms, including their axonal arborization and molecular marker content and *in vivo* recordings suggested that individual CCK cells may be active during different oscillatory states. In order to explore whether anatomical and physiological heterogeneities of the CCK+ INs can be linked to potential differences in the excitability of individual cells, we employed a variety of techniques, which allowed the investigation of a wide range of parameters from ionic currents to single cell transcriptomes.

**2.3** My third objective was to investigate the extent of the instrumental distortion on current clamp recordings from small neuronal structures. By creating a combined model of the phenomenologic representation of the recording instrumentation and the measured structure I aimed to recover the native, undisturbed electrical signal from heavily distorted patch clamp measurements.

### 3. METHODS

Animal protocols and husbandry practices were approved by the Institute of Experimental Medicine Protection of Research Subjects Committee (MÁB-7/2016 for slice recording and anatomy experiments and MÁB-2/2017 for immunolabelling experiments in perfusion fixed brains) and by the Veterinary Office of Zurich Kanton (ZH241/15, single cell RNAseq experiments).

#### 3.1 Preparation of acute brain slice for *in vitro* electrophysiology (for aim 2.1, 2.2 and 2.3)

For acute hippocampal slice preparations 21-36 days old Wistar rats were used from both sexes. Animals were decapitated under deep anaesthesia by isoflurane and the brains were removed from the cranium. 350  $\mu\text{m}$  thick brain slices were cut with a vibratome (VT 1200S, Leica) in a solution containing (in mM) 85 NaCl, 75 sucrose, 2.5 KCl, 25 glucose, 1.25  $\text{NaH}_2\text{PO}_4$ , 4  $\text{MgCl}_2$ , 0.5  $\text{CaCl}_2$ , and 24  $\text{NaHCO}_3$ , bubbled with 95%  $\text{O}_2$  and 5%  $\text{CO}_2$  for keeping the slices constantly oxygenated and to control the pH. The angle, in which slices were cut was adjusted to preserve the integrity of the MF pathway and their postsynaptic targets (Szabadics et al., 2006). Therefore, this cutting angle was parallel with the MF system and the apical dendrites of CA3 PCs as well, allowing the investigation of both dorsal and ventral hippocampus. The temperature of the cutting medium was ice-cold to help the survival of the cells. Slices were kept in a chamber filled with the mixture of the cutting and recording solution and were kept at 32,5 C°. For electrophysiological recordings, a standard artificial cerebrospinal fluid (ACSF) was used, which consisted of (in mM) 126 mM NaCl, 2.5 mM KCl, 26 mM  $\text{NaHCO}_3$ , 2 mM  $\text{CaCl}_2$ , 2 mM  $\text{MgCl}_2$ , 1.25 mM  $\text{NaH}_2\text{PO}_4$ , and 10 mM glucose. For standard recordings (aim 3.2), pipettes were filled with an intracellular solution containing 90mM K-gluconate, 43.5 mM KCl, 1.8 mM NaCl, 1.7 mM  $\text{MgCl}_2$ , 0.05 mM EGTA, 10 mM HEPES, 2 mM Mg-ATP, 0.4 mM  $\text{Na}_2$ -GTP, 10 mM phosphocreatine, and 8 mM biocytin (pH 7.2; 270–290 mOsm). The high intracellular chloride concentration is necessary for two reasons. First, by changing the reversal

potential of chloride for the recorded cell, inhibitory inputs are detectable when cells are clamped at their resting MP (the MP at which the cells required no holding current in current-clamp mode). Second, we found that recordings made with intracellular chloride concentrations closer to the physiological level are less stable than the ones made with high concentrations. In the first project however (section 3.1), one of our aims was to record inhibitory and excitatory synaptic events at the same time, which would have been impeded by the intracellular solution described above. Therefore, we used an intracellular solution with low chloride concentration, which was composed of (in mM): 133.5 Kgluconate, 1.8 NaCl, 1.7 MgCl<sub>2</sub>, 0.05 EGTA, 10 HEPES, 2 Mg-ATP, 0.4 Na<sub>2</sub>-GTP, 10 phosphocreatine-disodium (pH 7.25). Chemicals for the intra- and extracellular solutions were purchased from Sigma-Aldrich, ion channel blockers were from Tocris or Alomone and fluorophores were from Invitrogen.

### **3.2 Acute in vitro patch clamp recordings (for aim 2.1, 2.2 and 2.3)**

For recordings, cells in slices were visualized with an upright microscope (Eclipse FN-1; Nikon) with infrared (900 nm) Nomarski differential interference contrast (DIC) optics (Nikon 40x NIR Apo N2 NA0.8W objective). Slices were kept in the recording chamber at 34.5-36°C and were perfused with artificial cerebrospinal fluid (ACSF) with the speed of 1-2 ml/minute. For targeted recordings infrared differential interference contrast video-microscopy was used and the infrared signal was visualized by a Hamamatsu C-7500-50 CCD camera. Neuronal processes (soma, dendrite or axon) were targeted by a borosilicate pipette (World Precision Instruments Inc., Hilgenberg GmbH, Sutter Inc.), pulled by a horizontal micropipette-puller (P-1000, Sutter Inc.). Recordings were made using a software guided (Clampex 10.4) two-channel amplifier (Multiclamp 700B, Molecular Devices). Traces were low pass filtered at 6–100 kHz and digitized at 40–250 kHz using a Digidata 1440 A interface (Molecular Devices).

Whole-cell patch clamp recordings guided by DIC visualization were established by following the same basic steps. After visually confirming the lack of observable membrane damage of the selected neuron, the pipette was lowered into the recording chamber with applied pressure to avoid the contamination of the pipette solution with ACSF

and the pipette was pushed against the soma of the targeted cell. To achieve a tight connection of the two surfaces (a so-called “giga-seal” configuration, which refers to the extremely large electrical resistance between the pipette and the membrane), the pressure was relieved and a slight negative pressure was applied. By applying brief, but large negative pressure to the pipette, the membrane can be torn, and a direct electrical connection is established between the pipette and the cell, which is referred to as whole-cell configuration. To control the quality of our recordings, current responses to -5/-10 mV voltage steps were monitored, allowing the estimation of the resistance between the pipette and the contacted medium. Current responses to small voltage steps are informative about several different aspects of the recordings. First, when the pipette is lowered into ACSF, the time-independent current response to the seal test is used to calculate the tip resistance based on Ohm’s law. After establishing a tight connection with the cellular membrane, the current response is used to confirm the “giga-seal” configuration based on the same principle. When whole-cell configuration is achieved, the voltage commands elicit response from structural elements as well and the peak current reflects the series resistance ( $R_s$ ), where the steady-state current is determined primarily by input resistance ( $R_i$ ) of the recorded structure.

### **3.2.1 Somatic recordings (for aim 2.2)**

Current clamp (CC) recordings were made using thin walled pipettes (1.12 mm inner diameter and 1.5 mm outer diameter) with capacitance neutralization (CPN - the remaining capacitance was reduced by not fully neutralized) and bridge balance compensation was set to eliminate apparent voltage offsets upon current steps. The obtained voltage values were not corrected for the liquid junction potential (theoretically: -15.4mV). Firing patterns were elicited by square pulse current injections with different amplitudes (from -100 pA to 700 pA with 20 pA increment, 1 s long) from two different MPs (-60 and -80 mV). To characterize the effect of different holding MPs on the discharge patterns, current steps were set to elicit firing between 10-20 Hz and the 3-second-long preceding current step was varied to reach MPs between -90 and -50 mV. AP distributions were calculated from all recorded traces which contained APs, and binned by 50 ms for each cell independently.



Voltage clamp (VC) recordings of the potassium currents of CCK+INs were made with thick-walled pipettes (0.86 or 0.75 mm inner diameter and 1.5 mm outer diameter), because these pipettes have lower capacitance, which is imperative for correct elimination. Full pipette capacitance compensation and partial  $R_s$  compensation was applied. The degree of  $R_s$  compensation was set to lower values to avoid oscillation upon voltage steps (75-80% compensated with 53  $\mu$ s lag).  $R_{pip}$  was between 2–5 M $\Omega$ .  $R_s$  were between 6-20 M $\Omega$  (75-80% compensated with 53  $\mu$ s lag), and were constantly monitored. Data were discarded if the  $R_s$  changed more than 25%. In the recordings of potassium currents from CCK+INs, cells were patched in normal recording solution to obtain their firing pattern, and then 2.5  $\mu$ M TTX and 10  $\mu$ M ZD7288 was added to block sodium and  $I_h$  (non-selective cation) currents respectively. These conditions were used for the isolation of potassium currents. The protocol for these recordings consisted of several voltage steps for the measurement of MP dependence and kinetic parameters of the recorded current. First, a 300 ms long conditioning voltage step to -120 mV was applied to the cell, which aided the complete recovery from inactivation of the potassium channels. Next, a voltage step to more positive MPs was applied (ranging from -120 to -20 mV with a 10 mV increment) and the MP dependent activation and decay kinetics were measured. Last, the cell was clamped to -30 mV for 100 ms to obtain the voltage-dependence of channel inactivation. As the availability of potassium currents during non-steady-state conditions is determined by rate of recovery from inactivation a separate protocol was applied to obtain this crucial feature. The test protocol consisted of four voltage steps: (1) -120 mV for 345 ms, allowing full recovery, (2) -30 mV for 500 ms, allowing complete inactivation, (3) -65, -75, -85 or -120 mV steps with variable duration between 1-233 ms, (4) -30 mV test pulse, where the area of current was analyzed according to the voltage and duration of the preceding recovery step. Control traces were subtracted offline from each recording (control steps are identical, however steps 1 and 3 were set to -50 mV), which allowed the isolation of inactivating potassium currents. These recordings were conducted in the presence of TTX, 1 mM 4-AP and 10 mM TEA to reduce contamination from non-Kv4 channels. Leak and capacitive current components were subtracted during potassium current recordings using online P/-4 method.

### 3.2.2 Paired recordings (for aim 2.1)

*Paired recordings from CA3 GCs, gMFBs and CA3 PC were done by Dr Máté Neubrandt, Dr János Brunner and myself.*

The aim of paired PC-CA3 GC and PC – gMFB recordings was to measure elicited direct excitatory and disynaptic inhibitory responses. To this end, we used an intracellular solution with low chloride concentrations (section 4.1), which was necessary for the reliable distinction of disynaptic inhibitory and excitatory events as in low chloride concentrations the polarity of the two becomes opposite. It is important to note that tested PCs were not labelled with biocytin, as these cells can be unequivocally identified based on their firing pattern and passive membrane properties (Szabadics et al., 2010), and furthermore their labelling would have rendered the *post-hoc* identification of recorded gMFBs more difficult due to the number of filled structures in close proximity. Postsynaptic PCs were voltage clamped at -55 to -45 mV, which is above the reversal potential ( $E_{rev}$ ) of chloride, but still below the AP threshold. In cases when the amplitude of monosynaptic excitatory postsynaptic currents (EPSCs) was large and potential masking of the disynaptic inhibitory synaptic currents (diIPSC) had to be considered, we depolarized the PCs further towards the  $E_{rev}$  of EPSCs. To verify the viability of the recorded PC and healthy circuit conditions, we checked the presence of spontaneous inhibitory postsynaptic currents (IPSCs) and in their absence the recording was discarded.  $R_s$  (5–30 M $\Omega$ ) was monitored by the capacitive artifact in response to a 5-mV step in each trace. During the recordings, gMFBs were preferentially assessed in cell-attached configuration (without establishing whole-cell configuration), to preserve their synaptic release (Vyleta et al., 2014). Pipettes used for axonal recordings contained normal (high-chloride) intracellular solution (Szabadics et al., 2009). To increase the chance of recording monosynaptically connected gMFB – PC pairs, gMFBs were targeted on or near the apical dendrite of the recorded PC (exclusively in the stratum pyramidale and stratum lucidum). We also took advantage of the existence of ectopic GCs located in the CA3 stratum radiatum (CA3 GCs: (Szabadics et al., 2010)), which project morphologically indistinguishable axons to the stratum lucidum and elicit similar responses in their target cells. The depth of the recorded structures from the slice surface varied, gMFB – PC pairs were 30-50  $\mu$ m deep (to ensure healthy, but still visible boutons), while CA3 GCs were

located at the depth of 30-100  $\mu\text{m}$  to avoid cut axons. In some cases, presynaptic MFs were tested with multiple PCs ( $n = 82$  gMFBs with 2 PCs,  $n = 12$  with 3 PCs,  $n = 6$  gMFBs with 4 PCs). Presynaptic gMFBs were stimulated by squared pulse commands in either VC or CC mode. The command amplitudes were set to a level which was enough for observing AP current consistently for every delivered pulse. In order to obtain the biocytin labeled structure of the tested gMFB, we attempted to establish whole-cell recording configuration after sufficient number of recorded traces (at least 5). Some giant MF terminals however were recorded in whole-cell CC mode from the onset of the experiment, without cell-attached recordings ( $n = 18$ ). Presynaptic CA3 GCs were always recorded using somatic CC with normal (high-chloride) intracellular solution (including biocytin). All simultaneously recorded gMFBs, CA3 PCs and CA3 GCs were less than 300  $\mu\text{m}$  apart.

For the analysis of diIPSCs a predefined time window was selected, 2-7 ms after the peak of the presynaptic AP. Although it is possible that few spontaneous events were included in the analysis, recordings were discarded if the detection time window did not contain significantly more events than the spontaneous rate and the event kinetics, amplitude and delay were not consistent. There was a slightly higher probability for observing disynaptic connections from CA3 GCs (11.8%, 26 out of 219 CA3 GC pairs vs. 9.03%, 13 out of 144 MF pairs). Disynaptic delay was calculated from the peak of the presynaptic AP (in whole cell recordings) or the negative peak of the AP currents in cell attached recordings, which might introduce a slight difference for the measurement, however none of the final conclusions are affected by it as the rise of the AP is several times faster than the delay of diIPSCs. For kinetic parameters, 10-90% rise times and decay time constants were calculated from single exponential fits.

### **3.2.3 Dendritic patch clamp and outside-out patch recordings (for aim 2.2)**

Dendritic patch clamp recordings were performed to estimate the dendritic distribution of low-voltage activated, inactivating potassium currents in CCK+INs. First, whole-cell somatic CC recordings were made from CCK+INs, to confirm their cellular identity. During these recordings, cells were loaded with 20  $\mu\text{M}$  Alexa-594 fluorescent dye. After at least a 5-minute long loading period, the pipette was slowly retracted, to allow

resealing of the somatic membrane. Intact dendrites (with no visible “beading” or cut end) were selected 30-50  $\mu\text{m}$  deep from the slice surface, with varying distances from the soma under epifluorescent illumination. Thick walled pipettes ( $R_{\text{pip}}$ : 20-55  $\text{M}\Omega$ ) were filled with normal (high chloride) recording solution and 5  $\mu\text{M}$  Alexa-594 for the targeted, epifluorescent-guided dendritic patch clamp recording. The lower fluorescent dye concentration was necessary for the visualization of the target dendrite, even when positive pressure is applied to the pipette while advancing through the slice (which causes fluorescent dye to leak into the slice, thereby masking the fluorescent signal of the dendrite). To avoid photodamage, recordings where the total time of fluorescent illumination was more than 30 seconds, were discarded. After the whole-cell configuration was achieved, it was confirmed that no neighbouring structure was loaded by the dye. By slow retraction of the pipette, the outside-out configuration was established (meaning that only a small membrane area excised from the dendrite is connected to the pipette). The “seal-test” protocol was continuously recorded during the retraction of the pipette, to confirm the complete excision of a membrane patch, to monitor the stability of the recording, and importantly, to record the capacitive responses of the membrane. Patch potassium currents were evoked by similar voltage steps as described for whole-cell VC configurations, without pharmacological isolation (we did not observe significant  $I_h$ , calcium or sodium currents in the recorded patches with the applied voltage protocol). Inactivating potassium currents were isolated offline, by the subtraction of currents obtained with a -50 mV prepulse from currents measured with a prepulse of -80 mV. Leak and capacitive current components were subtracted during potassium current recordings using online P/-4 method. After outside-out patch recordings the pipette was pushed into a Sylgard ball (Sylgard 184, Merck), which allowed the isolation of capacitive currents associated with the pipette during the “seal-test” protocol. This recorded trace was used as a control and was subtracted from the “seal-test” recordings obtained before patch potassium currents were measured. The excised membrane area was estimated from the capacitive currents of the patch. Specific membrane capacitance ( $C_m$ ) was determined in nucleated patch experiments ( $n = 18$ ). During these recordings somatic whole-cell configuration is established, followed by a slight negative pressure applied to the pipette to attach the nucleus together with the retracted membrane to the tip of the pipette. Slow retraction of the recording electrode resulted in a relatively large isolated

membrane surface, which enveloped the nucleus. The attained membrane area is large enough to clearly visualize with DIC optics, therefore the surface area can be calculated by the following equation (Gentet et al., 2000):

$$surface\ area = (major\ axis + minor\ axis)^2 * \left(\frac{\pi}{4}\right) \quad (1)$$

A simplified circuit can be used to describe the nuclear patch configuration. The recorded capacitive transients are affected by two different resistances, therefore we calculated them independently. First, the  $R_s$  is estimated using the voltage command ( $V_{step}$ ) and the peak of the recorded current transient ( $I_{peak}$ ):

$$R_s = \frac{V_{step}}{I_{peak}} \quad (2)$$

Next, the membrane resistance ( $R_m$ ) is derived from  $V_{step}$ , the steady state amplitude of the current ( $I_{SS}$ ) and the  $R_s$  as follows:

$$R_m = \frac{V_{step}}{(I_{SS} - R_s)} \quad (3)$$

Using the calculated  $R_m$  and  $R_s$  values, the membrane capacitance ( $C_p$ ) is:

$$C_p = \tau * \left(\frac{1}{R_s} + \frac{1}{R_m}\right) \quad (4)$$

Where  $\tau$  is the time constant of the capacitive transient (not including the first 10  $\mu$ s of the trace, as these sample points are sensitive to the fast pipette capacitance). One requirement of capacitance calculation is the lack of active voltage-dependent conductances in the recordings. The “passiveness” of the traces was confirmed by the comparison of the positive-going and negative-going capacitive transients at the onset and the end of the small voltage step. The estimated capacitive current was then divided by the calculated surface area, which resulted in  $C_m = 1.015 \pm 0.014 \mu\text{F}/\text{cm}^2$ . As the membrane area cannot be calculated in outside-out recordings using this method due to the extremely small excised surfaces,  $C_p$  was estimated using the previous equations (equations 2,3 and 4) and were divided by  $C_m$ . Distances of the recording sites from the soma were measured based on posthoc epifluorescent or confocal images with the help of *in-situ* epifluorescent images captured during the recordings. For the comparison of somatic and dendritic current densities, somatic outside-out patches were obtained using the same protocol, with

similar pipettes. Current traces were low pass filtered at 10 kHz and digitized at 100 kHz. Capacitive membrane responses were digitized at 250 kHz, without filtering.

### **3.2.4 Axonal recordings (for aim 2.3)**

*All of the axonal recordings from sMFBs were made by Dr János Brunner. These results are indispensable for the interpretation of my results.*

According to electron microscopic data, the small axon terminals of the MFs can be classified as clear axonal varicosities with less than 2  $\mu\text{m}$  in diameter, therefore visually identifiable axonal structures were targeted in this size range at the stratum lucidum of the hippocampal CA3 region under DIC optics for sMFB recordings. To reduce the instrumental capacitance, which could theoretically alter native electrogenesis in small structures, thick borosilicate pipettes were used (inner diameter: 0.75 mm, outer diameter: 1.5 mm, Sutter Inc.) and pipette capacitance was compensated carefully in VC mode. Seal test responses were recorded with -20 mV voltage steps. After establishing the whole-cell configuration, passive and active membrane responses from the axon were measured in CC mode with different levels of CPN. At the end of the experiment, we collected morphological data by imaging the Alexa Fluor 594 with the confocal system. The obtained z stack image was then used to identify the recording position in the reconstructed axon. All data were collected without filtering (filter bypassed) at 250 kHz sampling rate.

### **3.3 Immunohistochemical processing (for aims 2.1, 2.2 and 2.3) and cell type characterization (for aim 2.2)**

*Immunohistochemical processing was done by Andrea Szabó, Dóra Kókay, Anrdrea Juszel and Dóra Hegedűs and the data analysis were done by myself. These results are indispensable for the interpretation of my results.*

Recorded cells were filled with biocytin for immunohistochemistry and morphology, except for the CA3 PC for objective 3.1 (see above). After electrophysiological recordings, slices were fixed in 0.1 M phosphate buffer containing 2% paraformaldehyde and 0.1%

picric acid at 4 °C overnight. The next day slices were re-sectioned at 50 or 60 µm thickness. Biocytin labelling was visualized with either Alexa 350-, Alexa 488-, Alexa 594- or Alexa 647-conjugated streptavidin. Immunopositivity for CCK was tested in all recorded cells for objective 3.2 with a primary antibody raised against CCK (1:1000, CCK, Sigma-Aldrich, Cat# C2581, RRID:AB\_258806, rabbit polyclonal). Several neurochemical markers were tested in CCK expressing INs: Vesicular Glutamate Transporter 3 (1:2000, VGluT3; Merck, Cat#AB-5421, RRID:AB\_2187832; guinea pig polyclonal), Cannabinoid receptor type 1 (1:1000, CB1R, Cayman Cat#10006590, RRID:AB\_10098690, rabbit polyclonal), special AT-rich sequence-binding protein-1 (1:400, Satb1; Santa-cruz Cat#sc-5989, RRID:AB\_2184337, goat polyclonal, 1:400), Reelin (1:400, Merck Cat#MAB5364, RRID:AB\_2179313, mouse monoclonal) and calbindin (1:1000, Calb1; Swant Cat#300, RRID:AB\_10000347, mouse monoclonal).

### **3.4 Post hoc identification of interneuronal cell types (for aim 2.2)**

CCK+INs can be further categorized based on their axonal projections in the CA3. Cells with immunopositivity for CCK and axonal projections restricted to the stratum radiatum were classified as SCA cells, named after their similar axonal projection pattern to an IN type described in the CA1 region (Cope et al., 2002), and the clear distinctions compared to other dendrite targeting types described in the literature (Lasztóczy et al., 2011). We found no unequivocally identifiable perforant-path associated cells. Based on the classical description the axonal arborisation of BC and MFA types (Hendry et al., 1985; Vida et al., 2000) can be clearly distinguished, as BCs cover the soma of their PCs and MFA cells innervate their proximal dendrites in the stratum lucidum. In practice, however their axonal projection is highly overlapping in close proximity of the parent IN soma, therefore clear distinction can only be made if distal (>200 µm) axonal branches were recovered. Accordingly, axons of BCs were found mainly in the stratum pyramidale and in substantially lower density in the stratum lucidum (close to the soma). In a complementary fashion, MFA axonal branches were mainly located in the termination zone of MFs; the stratum lucidum, the stratum oriens in the CA3c and even in the hilar region of the DG. With lower incidence, MFA axon invaded the stratum pyramidale close

to their somatic location, and the stratum oriens in the vicinity of the infrapyramidal blade of the DG. Therefore, MFAs and BCs were only categorized as such, if the axons were recovered in at least 200  $\mu\text{m}$  distance from the IN soma, or in cases if the axons invaded the hilar region.

### **3.5 Morphological reconstruction (for aims 2.2 and 2.3)**

The detailed morphology of the recorded and biocytin-filled structures were investigated with high-resolution microscopy. Sections were imaged using a Nikon C2 confocal system (60X objective, Plan Apo VC, NA=1.45, Nikon). Several steps were taken in order to capture the optimal images. First, we applied the Nyquist theorem to estimate the optimal pixel size and z-step size for the confocal image stacks (which corresponds to values that capture all the available information for the used optical system without over- or under sampling). Next, using the ImageJ software, the acquired image stacks were processed to achieve optimal signal-to-noise ratio; brightness and contrast, outlier removal (noise with the size of 1 pixel), and subtraction of background. Reconstruction of CCK+INs (for objective 3.2) was done by NeuroLucida (version 11, MFB Bioscience). Due to the thin diameter of the recorded axons (for objective 3.3) and large changes in diameter, these structures were reconstructed by an automatic tracing algorithm (Peng et al., 2010; Peng et al., 2014). The parameters of the reconstruction algorithm were tuned by hand and were tested in larger, well defined structures. Both the path of the recorded axon, and the diameter values were extracted by the algorithm automatically, however, every stage of the automatic reconstruction was manually corrected for if it was necessary (confirmed by visual inspection by the observed path and diameter ratios of the recorded fluorescent images).

### **3.6 Analysis of potassium channel subunits using immunohistochemistry (for aim 2.2)**

*All of the immunohistochemical processing and analysis of potassium channel subunits and auxiliary proteins were done by Dr Andrea Lőrincz and Dóra Rónaszéki,*



*analysis of the obtained data was done by Dr Andrea Lőrincz and myself. These results are indispensable for the interpretation of my results.*

Wistar rats (P25 and P45) were perfused through the aorta with 4 % paraformaldehyde and 15 v/v% picric acid in 0.1M Na-phosphate buffer (PB, pH = 7.3) for 15 min and 70  $\mu$ m thick coronal sections were prepared. For acute hippocampal slices, a different fixation was used. These slices were transferred to fixative containing 2% paraformaldehyde and 15 v/v% picric acid in 0.1 M PB for 2 hours at room temperature. After slices were washed in PB and subsequently embedded in agarose, they were resectioned to 70-100  $\mu$ m thick sections. Blocking was done in 10% normal goat serum (NGS) in 0.5 M Tris buffered saline (TBS) for one hour and incubated in a mixture of primary antibodies for one overnight at room temperature. The following antibodies were used in these experiments: rabbit polyclonal anti-CCK antibody (1:500, Sigma-Aldrich Cat# C2581, RRID:AB\_258806) mixed either with a mouse monoclonal anti-KChIP1 (1:500, IgG1, UC Davis/NIH NeuroMab Facility Cat# 75-003, RRID:AB\_10673162), a mouse monoclonal anti-KChIP4 (1:400, IgG2a, UC Davis/NIH NeuroMab Facility Cat# 75-406, RRID:AB\_2493100), or a mouse monoclonal anti-Kv4.3 antibody (1:500, IgG1, UC Davis/NIH NeuroMab Facility Cat# 75-017, RRID:AB\_2131966). To more reliably characterize labeled cells, a rabbit polyclonal anti-CB1 receptor (1:2000, Cayman Chemical Cat# 10006590, RRID:AB\_10098690) was also used together with the CCK antibody in some sections. Potential cells exhibiting transient outward rectification (TOR cells – see section 5.2) were identified by Satb1 immunolabelling in the perfusion fixed sections. To maximize the number of detected proteins, Satb1 and Kv4.3 were visualized by the same secondary antibody, because, their labelling pattern can be reliably distinguished, as Satb1 antibody labels nuclei and Kv4.3 is expected at the cytosol and plasma membrane. The following secondary antibodies were used to visualize the immunoreaction: Alexa 488-conjugated goat anti-rabbit (1:500, Thermo Fisher Scientific), Cy5 conjugated goat anti-rabbit (1:500, Jackson ImmunoResearch), Alexa 488-conjugated goat anti-mouse IgG1 (1:500, Jackson ImmunoResearch), and Cy3 conjugated goat anti-mouse IgG1 or IgG2a (1:500, Jackson ImmunoResearch) IgG-subclass-specific secondary antibodies. Biocytin was visualized with Cy5 conjugated Streptavidin (1:1000, Jackson ImmunoResearch).

Fluorescent images were acquired by an Olympus FV1000 confocal microscope (60x objective, 1.35 NA).

### **3.7 Single-cell mRNA (for aim 2.2)**

*The mRNA sequencing was done by Dr Jochen Winterer and data was analysed by Dr David Lukacsovich. I contributed to the procedure with the recording of CCK+INs and the collection of the cytoplasm of the recorded cells. These results are indispensable for the interpretation of my results.*

Single-cell mRNA sequencing was performed using The Clontech's SMARTer v4 Ultra Low Input RNA Kit. The cytoplasm of the recorded cells were aspirated by the recording pipette and were collected into a sample collection buffer. Thereafter, the samples were spun briefly, and were snap frozen on dry ice. Samples were stored at  $-80^{\circ}\text{C}$  until further processing, which was performed according to the manufacturer's protocol. Nextera XT DNA Sample Preparation Kit (Illumina) was used for library preparation, as described in the protocol of the manufacturer. Cells were pooled and sequenced in an Illumina NextSeq500 instrument using  $2 \times 75$  paired end reads on a NextSeq high-output kit (Illumina). After de-multiplexing the raw reads to single-cell datasets, we used Trimmomatic and Flexbar to remove short reads and adapter sequences and to trim poor reads. The remaining reads were aligned to the GRCm38 genome with STAR aligner. Aligned reads were converted to gene count using RSeQC. Python3 was used for all data analyses, which included the removal of poor-quality cells (at least 3000 genes were detected in each cell), normalization of gene expression data using scran, and analysis of differential expression of genes across cell types. Sequences of splicing variants of KChIP4, DPP6, and DPP10 were validated in the NCBI Genebank and UCSC databases.

### **3.8 Computational modelling (for aim 2.2)**

Computer simulations were performed using the NEURON simulation environment (version 7.5 and 7.6, downloaded from <http://neuron.yale.edu>). First, we implemented the

.SWC file of the detailed morphological reconstruction of the recorded cell with the help of the Import3d feature of NEURON. After rigorous inspection of the implemented morphology, the traced skeletons were segregated into distinct functional compartments; soma, dendrite, axon, axon initial segment (AIS), which were segmented according to the d\_lambda rule at 0.1 kHz (Hines et al., 2001). To recapitulate the recorded behavior of the reconstructed cell, first the passive electrical parameters (membrane capacitance –  $C_m$ , membrane resistance –  $R_m$ , axial resistance –  $R_{ax}$ ) need to be defined. Out of the three, two passive parameters are easily constrained, as  $R_m$  (or rather the leak conductance -  $g_L$  that define  $R_m$ ) can be estimated based on the input resistance ( $R_{input}$ ) and the membrane time constant ( $\tau_m$ ) is the product of  $C_m$  and  $R_m$ . These two features can be readily retrieved from passive membrane responses (to small, -20 pA and +20 pA current injection). “Passiveness” of the responses can be tested by the symmetricity of these two traces. The measurement of  $R_{ax}$  is more difficult and can be reliably determined experimentally only with two electrode current-clamp recordings (Rall et al., 1985). Therefore, axial resistance values were set invariably to 120  $\Omega\text{cm}$ , which is in the range of reported values (100-150  $\Omega\text{cm}$  (Bezaire et al., 2016)). The  $g_L$  and  $C_m$  values were fitted with the Multiple Run Fitter (MRF) algorithm of the NEURON simulation environment (ranges:  $C_m$ : 1.05 – 0.82  $\mu\text{F}/\text{cm}^2$ ,  $g_L$ :  $5 \cdot 10^{-5}$  –  $5.8 \cdot 10^{-5}$   $\text{S}/\text{cm}^2$ ) to the recorded passive traces. The reversal potential of the passive conductances ( $g_L$ ) was set to -63 mV, which was sufficient for establishing a resting MP in agreement with our recordings (TOR cells:  $-64.58 \pm 0.46$  mV,  $n = 85$ , regular spiking cells:  $-64.88 \pm 0.73$  mV,  $n = 79$ ).

Next, to replicate the active behavior of the cell, we selected a set of active conductances based on a previous publication (Bezaire). Due to the high dimensionality of the parameter-space, the properties of these conductances (voltage dependence and kinetics) were adjusted by hand rather than fitting. Conductance parameters were adjusted to reproduce several aspects of my measurements, including AP parameters (peak, half-width, AHP amplitude, threshold,  $dV/dt$  peak) and firing behaviors (accommodation of firing frequency and maximum firing frequency). The spiking parameters were measured on firing patterns elicited from -60 mV, as presumably the A-type potassium conductances (which are of key interest in project 3.2) have negligible effect on spiking at this MP.

For the accurate depiction of my experimental results, models are expected to reproduce the voltage-clamp measurements and account for the CC recordings of the firing behavior. Specifically, models were tuned to my measurements concerning two distinct firing phenotypes of CCK+INs (for details, see section 5.2). Briefly, approximately half of the recorded CCK+INs in the CA3 region fired with a substantial AP onset latency when they were stimulated from slightly hyperpolarized MPs, however the AP delay disappeared when the firing was elicited from slightly depolarized MPs (these cells are referred to as TOR cells – Transient Outward Rectification). The other half of the recorded CCK+INs showed no MP-dependence in their firing, therefore they are termed RS cells (Regular Spiking). The ionic current which underlie the TOR phenomenon was determined to be an A-type potassium current ( $I_{SA}$  – Subthreshold A-type potassium current) that is mediated by Kv4.3 channels, which were modelled by two conductance models, to account for the differences in the measurements from TOR and RS cells. To take into consideration the limitations of whole-cell VC recordings in clamping distal cellular compartments (Rall et al., 1985; Spruston et al., 1993), the distribution of  $I_{SA}$  was determined from pooled outside-out patch recordings. Whole cells VC and CC simulations were run with protocols identical to the ones used in our patch clamp recordings, with the appropriate uncompensated  $R_s$  implemented in the VC models ( $2.76 \pm 0.28 \text{ M}\Omega$ ,  $n = 14$ ).

$I_{SA}$ RS conductance model parameters were constrained on whole-cell current recordings (in the presence of sodium current -  $I_{NA}$  and hyperpolarization activated nonselective cation current –  $I_h$  blockers, with offline isolation of the currents blocked by specific Kv4.3 blocker; Heteropodatoxin-2), as we observed similar kinetics and voltage-dependence of the recorded outside-out patch currents and whole-cell currents. The MP dependent steady-state activation (*minf*) and steady-state inactivation (*hinf*) of the  $I_{SA}$ RS model was set by the following Boltzmann equations:

$$minf = (1/(1 + \exp(-(v + 26.5)/13)))^4$$

$$hinf = 1/(1 + \exp((v + 59)/4))$$

The activation time-constant and deactivation time-constants were set by a bell-curve:

$$mtau = 0.1 + 1 * \exp(-0.5 * ((v + 57.5)/10)^2)$$

These two kinetic parameters were defined with the same curve, as in conductance models generally a positive shift in the MP results in the activation of the potassium channel and hyperpolarization causes deactivation at the same rate. The same relationship was set for the decay time constant and recovery from inactivation, which was defined as:

$$h\tau = 4.5 + 50 * \exp(-0.5 * ((v + 76)/25)^2)$$

if  $v < -40.95$  mV:

$$h\tau = 1 + \exp(5.1 + (0.05367 * v) + (0.000167595 * v^2))$$

The use of two bell curves was necessary, as the measured recovery from inactivation and decay time constant could not be fitted with a single one. Instead, I defined two curves, which independently fitted the two measurement accurately and had no abrupt break-point at their crossing at -40.95 mV. The acquired conductance model was then tested in CC mode, which confirmed only a minor effect of  $I_{SARS}$  on the delay of the first AP (Figure 16).

The outside-out patch recordings were however much more variable from TOR cells than in RS cells, with some of them exhibiting similar voltage-dependence to RS cells. To account for these observations, the A-type potassium conductance of TOR cells was modelled as a mixture of two conductances, one of which is the already established  $I_{SARS}$ . The leftward-shifted (see section 5.2)  $I_{SA}$  model ( $I_{SATOR}$ ) parameters and the ratio of  $I_{SATOR}$  and  $I_{SARS}$  were constrained on both VC and CC recordings. MP dependent activation and inactivation was defined as follows:

$$minf = (1/(1 + \exp(-(v + 59)/7)))^4$$

$$hinf = \left( \frac{1}{1 + \exp\left(\frac{v + 70}{4}\right)} + \frac{1}{1 + \exp\left(\frac{v + 78}{4}\right)} \right) / 2$$

with the following kinetic parameters:

$$m\tau = 0.1 + 1 * \exp(-0.5 * ((v + 59.5)/10)^2)$$

$$h\tau = 2 + 90 * \exp(-0.5 * ((v + 54)/35)^2)$$

if  $v > -66.2$  mV:

$$h\tau = 44 + 60 * \exp(-(v + 61)^2/80)$$

To investigate the behavior of these model cells in *in vivo* relevant conditions, physiologically plausible input conditions were constructed with a large number of temporally organized synaptic excitatory and inhibitory events. Accurate representation of the excitatory and inhibitory inputs was based on spontaneous synaptic events from recordings made with less than 2 M $\Omega$  uncompensated R<sub>s</sub>, using intracellular solutions, containing CsCl (133.5 mM CsCl, 1.8 mM NaCl, 1.7 mM MgCl<sub>2</sub>, 0.05 mM EGTA, 10 mM HEPES, 2 mM Mg-ATP, 0.4 mM Na<sub>2</sub>-GTP, 10 mM phosphocreatine, and 8 mM biocytin, pH: 7.2; 270–290 mOsm). GABAergic events were recorded in the presence of 10  $\mu$ M CNQX (6-Cyano-7-nitroquinoxaline-2,3-dione) and 20  $\mu$ M D-AP5 (D-(-)-2-Amino-5-phosphonopentanoic acid), and were confirmed at the end of the recordings by adding 5  $\mu$ M SR 95531 hydrobromide (6-Imino-3-(4-methoxyphenyl)-1(6H)-pyridazinebutanoic acid hydrobromide). Glutamatergic events were isolated by the application of 5  $\mu$ M SR 95531 hydrobromide, and were confirmed at the end of the recordings by 10  $\mu$ M CNQX and 20  $\mu$ M D-AP5. Considering that we observed no significant difference in the amplitude of the excitatory events in the two CCK+IN populations (TOR:  $-43.4 \pm 0.6$  pA, RS:  $-41.6 \pm 0.4$  pA, Mann-Whitney test;  $p = 0.1398$ ,  $U = 3.42002 * 106$ ,  $Z = 1.47654$ ,  $n = 7$  TOR and 6 RS cells), recordings were pooled and averaged. To incorporate the biological variability of synaptic inputs, simulated excitatory events were picked from a normal distribution with a mean of 0.22 nS (which corresponds to the average excitatory event amplitudes in my measurements, divided by the driving force) and the variance of 0.01 nS. The simulated inhibitory conductance was adjusted to represent both tonic and phasic inhibition. Therefore, the mean of the normal distribution was slightly lower than what our measurements predicted (TOR measurement:  $-89.1 \pm 1.4$  pA, RS measurement:  $-78.1 \pm 1.7$  pA, model mean: 2 nS) and the variance of the normal distribution was larger (variance: 0.1 nS). Synaptic conductances were uniformly distributed along the somatas and dendrites of the simulated cells. In the final model, inhibitory conductances followed a uniform random temporal distribution, whereas excitatory events were aggregated into normal distribution packages at various frequencies for simulating *in vivo* relevant MP oscillations in single cells, as follows:

$$onset_{Glut} = \frac{1000}{freq} * 0.633 + \left(69.25112 * (0.67747^{freq})\right) + \frac{1000}{freq}$$

where  $onset_{Glut}$  is the timing of an individual excitatory event, and  $freq$  is the frequency which excitatory packages occur. The onset equation takes into consideration the frequency of the oscillation because if the width of the normal distributions was not adjusted, at low frequency ranges the excitatory event packages would be segregated and at high frequencies these packages would overlap substantially, creating a homogenous, tonic excitation. The simulations included 20 oscillatory cycles, or in case of high frequencies at least 5 seconds of run time, ensuring that steady-state conditions can be isolated by discarding some of the starting cycles. During the initialization of each run, inhibitory and excitatory input conductances and onset timings were randomized in a unique, but reproducible manner (pseudo-randomization with a seed value), therefore each simulation were distinct, but could be repeated for individual TOR and RS cell models. At each input frequencies the input strength was constantly elevated (by increasing the number of inputs), to elicit more spikes from the models. In each case, when the RS model (equipped with  $I_{SA}RS$ ) showed AP discharge, simulations were repeated with the TOR model (equipped with  $I_{SA}TOR$  and  $I_{SA}RS$ ). Simulations were stopped when RS cells produced firing above 50 Hz. Changes in firing rate caused by the replacement of  $I_{SA}RS$  with  $I_{SA}TOR+RS$  was calculated by subtraction of the TOR firing rate from RS firing rate and normalized to the latter. Simulations were parallelized and run on the Neuroscience Gateway (Sivagnanam et al., 2015).

### 3.9 Constraining the model amplifier (for aim 2.3)

*The description of the model amplifier in its entirety is the work of Dr János Brunner. These results provide the framework of my further modelling work, therefore are indispensable for the interpretation of my results.*

We systematically collected data about the behavior of the amplifier using three different test configurations (Figure 28A) to emulate the amplifier features in the NEURON.

In the first test we assessed real VC responses of the isolated head stage in open circuit, that is, without electrode holder, pipette and connection to the ground (test #1). This configuration was sufficient to characterize both the high frequency boost unit and capacitance compensation of the VC circuitry. Similar open circuit measurements are not possible in CC mode therefore we closed the circuit through a resistor (test #2). The third test circuit was a modified 1U model cell circuit (test #3, Molecular Devices) which contained passive electrical circuits representing a cell and a measuring pipette therefore it is suitable to emulate whole-cell recording conditions. To make the model cell more flexible we used conductive metal slots taken from a circuit breadboard to fix and connect electrical component. We characterized the stray capacitance of each elements of the test circuits by measuring the capacitive load associated with the introduction of the given circuit element in VC mode. Parasitic capacitances were then included to the simulations during the development of the amplifier model. Capacitors were considered ideal, that is, without any resistive component.

Biological recordings were made with bypassed filtering mode (where the amplifier output was conditioned only with a 100 kHz low pass filter) because stronger filtering may mask higher order amplifier signals, which can be important to understand and model the amplifier behavior. The 100 kHz cutoff is well above the biologically relevant frequency domain of the recorded signals therefore cellular responses will be unaffected by the filter. We supplied our model with an active linear filter having two cascaded Sallen-Key topologies (Figure 28B). Filter parameters were set to create output with four pole low-pass Bessel filter characteristics with a cutoff frequency at 100 kHz designed using an online available filter design tool (<https://www.analog.com/designtools/en/filterwizard/>).

### **3.10 Pipette parameter measurements (for aim 2.3)**

*The description of the pipette is the work of Dr János Brunner and Gergely Tarcsay.*

We assessed the pipette capacitance as a function of the tip distance by dipping known part of the recording pipettes to the recording solution. Pipette position was defined by the x axis values of the micromanipulator used for positioning the electrodes (SM5 controller with Mini unit, Luigs&Neumann). First, we recorded the total capacitance of the instrumentation



in open circuit VC mode where pipette was out of the solution. Then we moved the pipette to the position where the tip reached the surface of the fluid characterized by the appearance of short conductive periods in the recorded VC signal. We inserted the pipette further (typically less than 5  $\mu\text{m}$ ) to the solution to reach a position where the conductive state became stable. We considered that position as the tip position. Starting from that point, we systematically increased the length of the dipped part and recorded the capacitance of the pipette. We quantified the capacitance of the immersed part in VC measurements by integrating the first 50  $\mu\text{s}$  of the capacitance response to a -20 mV step command. To measure the resistance distribution along the pipettes, we systematically broke off known length of the pipette tip and measured the resistance of the remaining part in VC mode. First, we moved the pipette tip to a defined position under the objective and recorded its resistance. After withdrawal of the pipette, we broke the tip by gently touching it with a piece of lens cleaning tissue. The newly formed electrode tip was then positioned back to the reference position on the image. We determined the length of the removed part as the resulting x-axis difference. Resistance was measured in VC mode using -2 to -20 mV steps.

We examined the inner/outer diameter ratio ( $R_{oi}$ ) of the high impedance electrodes using a grinding system. The borosilicate glass pipettes (the first 8-12 mm from the tip) were embedded into epoxy resin on a microscope slide. Pipettes were longitudinally grinded with a coarse-grained aluminium-oxide abrasive disc (grit size=600) until we reached the surface of the pipettes. We continued the grinding in a stepwise manner (grit size=6000) and we imaged (DM2500, Leica, 5X-100X magnifications) the pipette surface after each grinding step. We switched to fine-grained abrasive discs (grit size=6000) as the plane of the tip was approached. The obtained images were then used to measure the pipette dimensions (in PhotoShop 5.0). During the analysis, we calculated the  $R_{oi}$  at predefined tip distances for each plane. Since we could not resolve the exact median plane, we quantified the relative wall thickness as the lowest measured  $R_{oi}$  value in each position.

### **3.11 Validation of voltage- and current clamp model adequacy (for aim 2.3)**

*Validation of voltage- and current clamp model adequacy is the work of Dr János Brunner, Gergely Tarcsay and myself.*

Precise *in silico* reconstruction of the experiment requires parameter estimation consisting of three consecutive fitting steps. First, we used VC data for tuning the actual pipette parameters (1). After connecting the model instrumentation with the detailed morphology of the recorded structure, we created the passive structure of the cell and adjusted the  $R_{\text{access}}$  according to the CC measurements (2). Next, we equipped the model structure with active sodium and potassium conductances and tuned their properties to reproduce the experimentally recorded AP waveform (3). Finally, having established the appropriate conductance set, we were able to obtain the native behavior of the axon (4).

Our general strategy for outlining the theoretical upper bound for the fitting accuracy of the desired parameters consisted of the generation of model traces with known parameters supplemented with random Gaussian noise and the subsequent fitting of the resulting waveform with randomized initiations. The supplemented noise level was in agreement with our recording conditions ( $SD = 1.73$  mV for CC and  $SD = 20$  pA for VC, unless stated otherwise). The model initiations were set to cover the feasible parameter space.

### **3.12 Data analysis and statistics (for aim 2.1 and 2.2 and 2.3)**

No statistical methods were used to predetermine sample sizes, but our samples are similar to or exceed those reported in previous publications and that are generally employed in the field. The experimenter was aware of the experimental condition in the case of the electrophysiology-imaging experiments. Data was analysed using Molecular Devices pClamp, OriginLab Origin, Microsoft Excel software and Python-based scripts. Normality of the data was analysed with Shapiro-Wilks test. For the comparison of two parametric sample groups the Student t-test was used, and the probability of the two-sample means being equal, the t-statistic and the degrees of freedom are denoted. For non-parametric comparisons the Mann-Whitney test was used, and results are denoted by the probability of the two sample groups having identical distributions, the U and the Z statistic. Data are presented as mean  $\pm$  s.e.m.

## 4. RESULTS

### 4.1 Feedforward inhibition is randomly wired from individual granule cells onto CA3 pyramidal cells

The innervation scheme of a FFI circuit can be organized in several distinct manners (Ferrante et al., 2009; Pouille et al., 2001), which has fundamental consequences on the performance and constraints of the neuronal circuit. To distinguish between the possible wiring arrangements of the FFI circuit of the DG-CA3 interface and to gain insight into the preferred tripartite connectivity between individual MFs, FF-INs, and PCs, we recorded disynaptic inhibitory postsynaptic currents (diIPSCs) in PCs evoked by a single MF, which was activated by either directly recording from a visually identified MF terminal (Figure 8a; (Szabadics et al., 2009)) or a GC in the CA3 (CA3 GC) (Szabadics et al., 2010). These disynaptic events reflect the reliable activation of an intermediate, not recorded FF-IN by a single C input. This locally activated FF-IN, in turn, provides characteristic inhibitory events to the recorded PC within a time window that is consistent only with two synaptic steps (2–7 ms; (Brown et al., 1983; Mori et al., 2004; Szabadics et al., 2010)). Convergence of monosynaptic excitatory and disynaptic inhibitory connections in a single PC indicates that the individually recorded GC innervates both this PC and a FF-IN and the latter also innervates the same PC. To detect both the depressing and the less reliable, facilitating disynaptic activations (Lawrence et al., 2004; Szabadics et al., 2009; Torborg et al., 2010; Toth et al., 2000), the presynaptic stimulation protocol consisted of three low-frequency APs at 20 Hz, followed by a sustained high-frequency train (6 or 15 APs at 150 Hz). Thus, diIPSCs are sufficient tools to directly assess the single GC-initiated FFI. To address the three hypotheses presented above, the recorded PCs were assigned to one of two groups based on the presence ( $n = 42$  tested pairs) or absence ( $n = 321$  tested pairs) of monosynaptic excitatory postsynaptic currents (EPSCs) from the simultaneously recorded MF or CA3 GCs. In these experimental arrangements, the testable assumptions are that (1) if the FFI is ensemble-specific, then the proportion of diIPSC connectivity is higher in the monosynaptically excited PC group; (2) in case of lateral inhibition, a lack of diIPSC connections is expected in the directly innervated Cs; and (3) similar diIPSC proportions and similar properties are expected

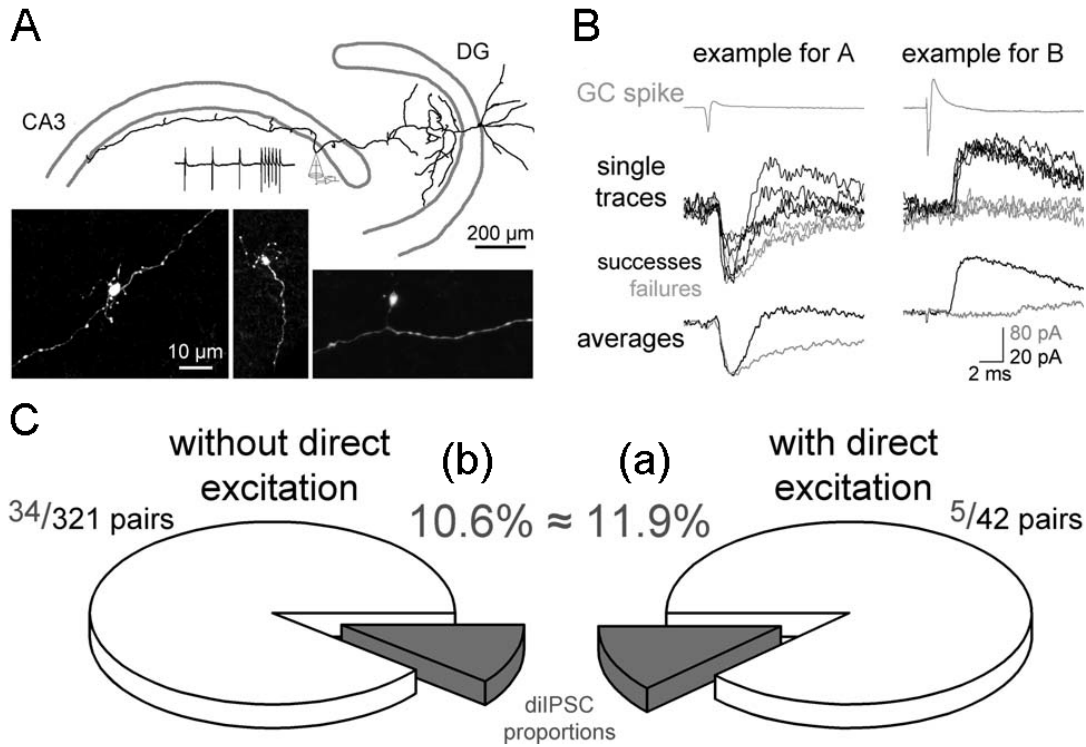


**Figure 8.** Wiring of FFI between individual cells of the DG-CA3 interface.

A. Drawing of the partially recovered presynaptic axons and dendrites of a DG GC. One of its large terminals was recorded in cell-attached configuration and was subsequently in whole-bouton mode to load with biocytin for the anatomical recovery. The presynaptic spikes at two frequencies during cell attached simulation are shown on top. B. Example traces of MF terminal and PC pairs with diIPSC connectivity only (i.e., positive example for PCs in group b) and with both monosynaptic EPSC and diIPSC connectivity (i.e., group a). The upper gray traces show the average presynaptic action currents in the giant bouton in cell-attached mode, the middle traces are individual postsynaptic responses or failures, and the trace pairs at the bottom show the averages of all traces with (black) or without (gray) diIPSCs. The morphology of one of the presynaptic GCs (right example) is shown on panel B. The example traces were recorded with 20 Hz stimulation. C. Pie charts summarizing the numbers and probabilities of detecting diIPSCs between single MFs or GCs and PC pairs. The tested PCs either received monosynaptic EPSCs from the stimulated MF (group a, right pie) or lacked direct excitatory connections (group b, left pie). This arrangement led to similar probabilities of finding diIPSCs in the two groups (p5.791, Fisher's exact test).

if the FFI is randomly distributed from individual GCs. We found that the probabilities of observing single-MF-elicited diIPSCs were similar in the two groups of PCs (5 diIPSC couplings out of 42 tested pairs with monosynaptic EPSCs, 11.9%; 34 diIPSC couplings out of 321 tested pairs without monosynaptic EPSCs, 10.6%; Figure 8c). Statistical comparisons

using the binomial test-based Fisher's exact test did not reject the hypothesis that the proportions of diIPSC connections in the two groups were similar ( $p = 0.791$ , the estimated difference between the sample  $p$  values was  $-0.013$ ; the 95% confidence interval was between 0.0904 and 20.1167). The prevalence of diIPSCs was similar when we considered

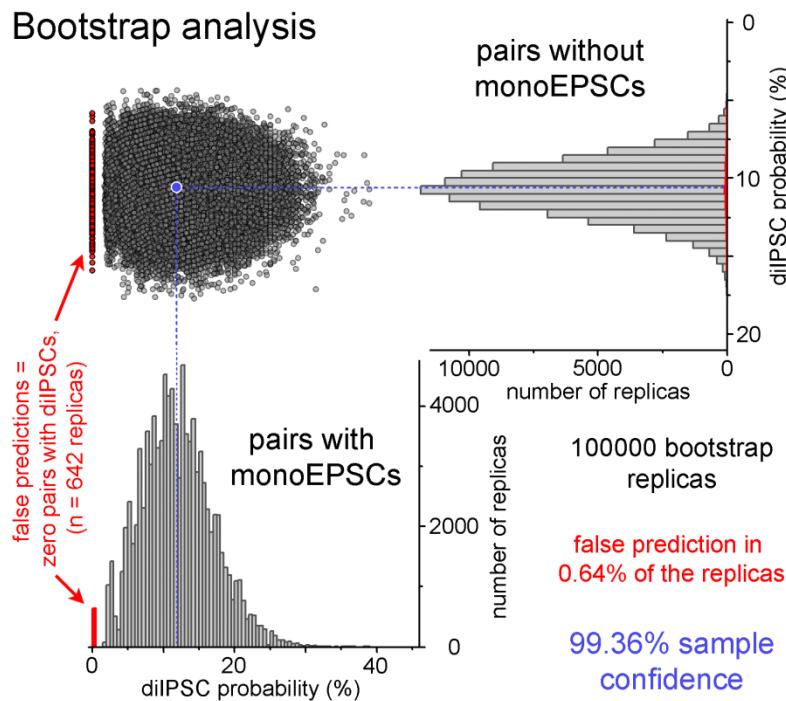


**Figure 9.** Bootstrap resampling of the experimental data set.

In order to test the accuracy of the predictions of the obtained data, we simulated the incidences of diIPSC-connectivity among the directly excited (A group in Figure 8) and not excited PCs (B group) using bootstrapping approach in 100000 replicas. We considered replicas false prediction (red symbols) if the resampled data did not contain any diIPSC-connectivity between monosynaptically connected MF-PC pairs (never occurred) or between not connected MF-PC pairs (642 replicated cases). Transparent gray symbols indicate the replicas in which diIPSCs occurred in both groups of tested PCs (99358 replicated cases). Blue circle indicates the experimentally observed ratios. Notice the different diIPSC probability axis for the two data sets.

only those pairs wherein the presynaptic recording was made on giant MF terminals, which presumably originate from DG GCs (3 pairs with dual, disynaptic IPSC and monosynaptic EPSC connections out of 32 tested pairs with monosynaptic EPSCs, 9.4%; and 10 diIPSC connections out of 112 tested pairs without monosynaptic EPSCs, 8.9%). Thus, the directly innervated PCs are neither spared nor preferred by single MF-evoked FFI. This is

inconsistent with hypotheses #1 and #2 and supports the hypothesis #3, which states that the FFI is randomly distributed between the DG and the CA3.

For additional analysis on the accuracy of the obtained data size, we used bootstrap

**Table 1.** Comparison of the properties of the diIPSCs (n = 30 diIPSC only connections and n = 4 diIPSC in dual connections).

Mean $\pm$ s.e. (Median)	diIPSC only connections	diIPSC in dual connections	MW-test p value
<b>Delay from AP (ms)</b>	3.53 $\pm$ 0.12 (3.53)	4.11 $\pm$ 0.31 (4.33)	0.104
<b>Variance of delay (ms<sup>2</sup>)</b>	1.18 $\pm$ 0.14 (1.18)	1.04 $\pm$ 0.38 (0.8)	0.808
<b>Rise time (ms)</b>	0.93 $\pm$ 0.05 (0.85)	0.76 $\pm$ 0.11 (0.81)	0.398
<b>Decay time constant (ms)</b>	8.40 $\pm$ 0.43 (8.03)	8.88 $\pm$ 0.55 (8.88)	0.450
<b>Potency (pA)</b>	34.8 $\pm$ 2.8 (33.6)	70.5 $\pm$ 37.3 (37.9)	0.375

resampling. Bootstrapping is a statistical test that allows assigning measures of accuracy to sample estimates based on random resampling with sample replacement with the Monte Carlo method (Efron, 1979). The basis of this method is the creation of multiple sets of sample populations with sizes identical to the measurements, by sampling from the entire recorded dataset with sample replacement. By calculating the fraction of cases in which diIPSCs were present for monosynaptically coupled and uncoupled PCs in the synthesized sample populations, we could directly estimate the probability of our recordings representing the random wiring scheme. For this, we used sampling with case replacement from 5 recordings with diIPSCs and monosynaptic EPSCs, 37 recordings with monosynaptic EPSCs, 34 recordings with only diIPSCs and 287 recordings with no connections. This procedure was repeated 100000-times. The confidence of our conclusions can be estimated as the fraction of cases, in which non-specific FFI was found. Interestingly, none of the replicas supported the ensemble-specific wiring, while only 642 replicas showed lateral inhibition, resulting in a 99.36 % sample confidence, thus confirming our assessment of the wiring scheme of FFI despite the seemingly low sample numbers.

It is important to note that the relative numbers of the directly excited PCs in our sample are not representative. This is because we intentionally targeted likely connected MF-PC pairs to increase the number of observations for both PC groups. Nevertheless, this aspect of our approach does not affect the unbiased sampling of FFI and diIPSCs. In triplet, quadruplet and quintuplet-recordings, wherein 2, 3, or 4 PCs were tested with the same presynaptic MF source and at least one of them received a diIPSC, the prevalence of the diIPSCs in the other concurrently tested PCs (considering 12 pairs) were apparently higher (5 out of 12) than in the complete pool of data, as expected from the highly divergent

**Table 2.** Comparison of the properties of the EPSCs in pairs with or without diIPSCs (n = 28 EPSC only connections and n = 4 EPSC in dual connections).

Mean $\pm$ s.e. (Median)	EPSC only connections	EPSC in dual connections	MW-test p value
<b>Delay from AP (ms)</b>	0.61 $\pm$ 0.03 (0.57)	0.71 $\pm$ 0.08 (0.63)	0.224
<b>Rise time (ms)</b>	0.89 $\pm$ 0.04 (0.82)	1.02 $\pm$ 0.11 (0.95)	0.178
<b>Decay time constant (ms)</b>	6.41 $\pm$ 0.37 (5.95)	7.48 $\pm$ 0.89 (6.83)	0.213
<b>Facilitation (3<sup>rd</sup>/1<sup>st</sup> 20Hz-AP)</b>	1.33 $\pm$ 0.10 (1.26)	1.44 $\pm$ 0.31 (1.23)	0.903
<b>Facilitation (150Hz/20Hz charge)</b>	6.92 $\pm$ 1.30 (5.02)	6.79 $\pm$ 0.08 (6.79)	0.405

innervation of PCs by feedforward inhibitory cells (Acsady et al., 1998; Bezaire et al., 2013). Furthermore, the properties of the diIPSC events were similar regardless of the presence of monosynaptic EPSCs from the same single GC source (Table 1).

Thus, not only the wiring probability, but also the strength and kinetics of the inhibition (thus, the source of FFI; see discussion) appear to be similar in excited and not excited PCs. The properties of the monosynaptic EPSCs were also similar between pairs with both inputs and pairs with EPSCs only (Table 2). Thus, the PCs that are readily and strongly inhibited following GC activity seem to be similarly excited to those wherein no diIPSCs were detected.

Our findings reveal that individual MFs recruit CA3 PCs and FFINs regardless of the presence of inhibitory synaptic connections between them. Therefore, FFI between the DG

and the CA3 is not wired to specifically inhibit a restricted population of PCs selected based on direct excitation from the GCs. This is consistent with the idea that the FFI is randomly distributed by individual GCs, which allows for the adjustment of general excitability of the CA3 network based on the activity of the DG. Our results from a sufficiently large sample size confirm the previous observations in slice cultures indicating disynaptic inhibition both in directly connected PCs and in PCs that are not excited by the same GC (Mori et al., 2007).



## 4.2 Functional specification of CCK+ interneurons by alternative isoforms of Kv4.3 auxiliary subunits

A crucial aspect of our findings discussed above is that our observations suggest that the various types of FF-INs follow the random wiring rules in a similar manner, as the kinetic properties of the diIPSCs were found to be similar in both groups of PCs. Uniform contribution of distinct cell types to the FFI circuit allows DG GCs to dynamically select a subpopulation of FFINs for certain tasks. Recruitment of these INs however critically depends on the neuronal excitability, therefore our next aim was to investigate, how FFIN excitability contributes to the diverseness of the DG-CA3 interface. To this end, we focused on one of the most numerous and diverse inhibitory cell class of the CA3 region, the CCK+ INs. Although these cells are heterogeneous in anatomical terms, including their axonal arborization and molecular marker content, their *in vitro* firing characteristics are considered to be homogeneous and distinct from other inhibitory cell types. However, *in vivo* recordings suggested that individual CCK cells may be active during different oscillatory states. Because of these complexities, hippocampal CCK+INs are ideal to address the question of boundaries of cell classes from a broader perspective, including genes, molecular content, morphology, excitability and potential contributions to specific physiological functions.

### 4.2.1 Half of the CA3 CCK+INs show state-dependent firing

To explore potential differences in the excitability of individual CCK+INs in the CA3 region of the rat hippocampus, first we characterized their firing properties in two different conditions. Specifically, we recorded the spiking in response to current steps from two, physiologically plausible MP ranges of *post hoc* identified CCK+INs. We focused mostly on CA3 region because CA3 CCK+INs are the most diverse within the hippocampus. When CCK+INs ( $n = 557$  cells) were stimulated from slightly depolarized MPs (MP, range:  $-60 - -65$  mV) relative to rest ( $-64.7 \pm 0.4$  mV), AP firing always showed spike-frequency accommodation, which is one of the most characteristic features of this cell class (Cea-del Rio et al., 2011; Glickfeld et al., 2006; Szabadics et al., 2009; Szabó et al., 2014).

However, we noticed that numerous CCK+INs ( $n = 290$  cells) showed MP-dependent firing: their initial spiking was strongly inhibited and its onset was delayed when it was

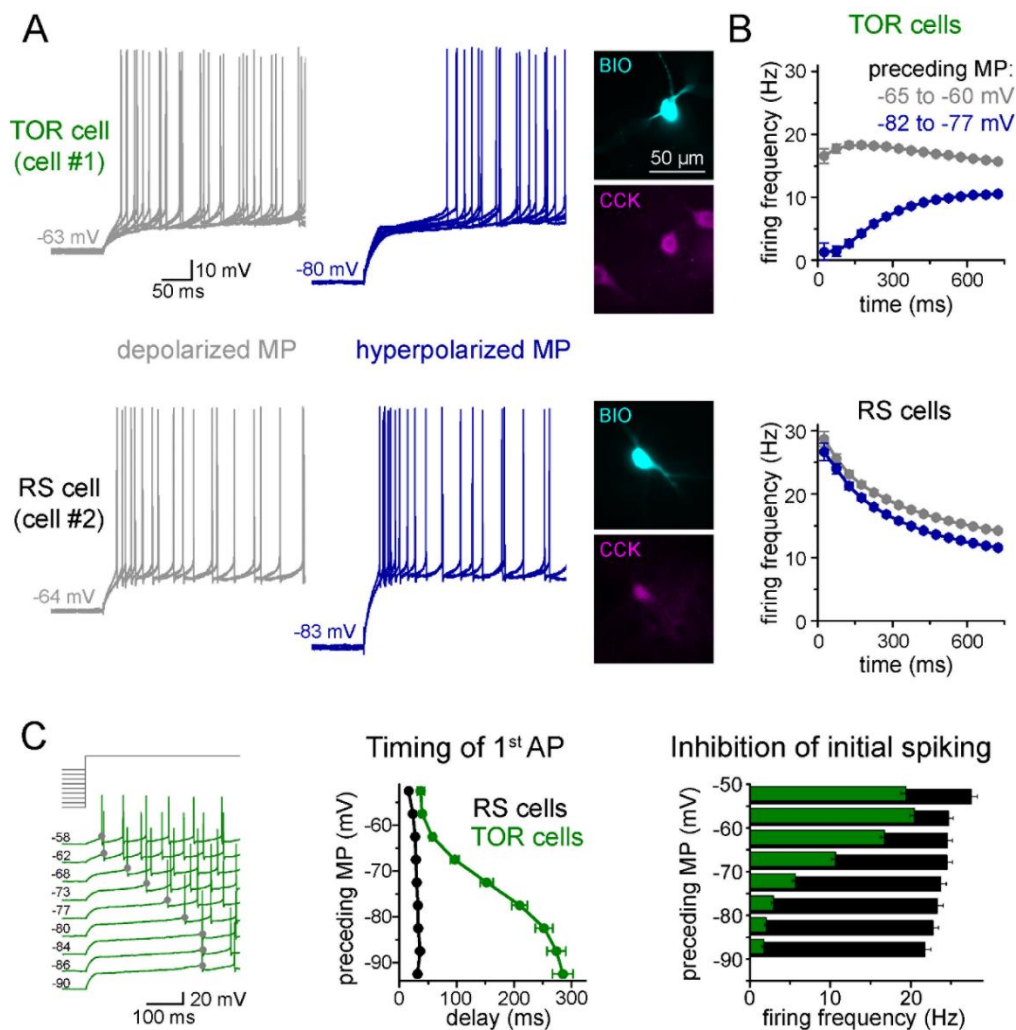


**Figure 10.** Two distinct firing patterns within CA3 CCK+ cells.

A. Firing properties of two representative CCK+INs in the CA3 hippocampal region. Firing was elicited with square pulse current injection of identical amplitude, from depolarized (grey traces), or hyperpolarized MPs (blue traces). Several trials are superimposed to show the stability of the timing of the first AP. Insets show the immunolabelling of the biocytin filled (BIO) recorded cells for CCK. B. Average time course of AP occurrence in TOR and RS cells from two MP ranges ( $n = 120$  and  $113$  representative cells, respectively). C. Timing of the first AP and probability of APs during the first 150 ms of the square stimulus shows steep MP-dependence in TOR cells, whereas the initial spikes are stable in the RS cells. The amplitude of stimulating current steps was standardized for each cell and only the preceding holding current (3 seconds) was varied in individual trials. Traces show a representative recording from a TOR cell. The average data derived from 85 TOR and 81 RS cells.

evoked from hyperpolarized MPs (between  $-75$  to  $-85$  mV, Figure 10A-B). On average, these cells started firing after a  $252 \pm 15$  ms silent period from hyperpolarized MP (measured from

the start of the current injection). We categorized these cells as Transient Outward Rectifying cells or TOR cells (a term that was used to describe cells in other brain regions (Stern et al., 1996)). The rest of CCK+INs ( $n = 267$  cells) were characterized as regular spiking or RS cells as they fired regularly irrespective of their MP and they started firing with a short delay ( $33 \pm 2$  ms) when stimulated from hyperpolarized MP. At depolarized MP ( $-55$  to  $-65$  mV), the first APs of both TOR and RS cells occurred with short delays ( $48 \pm 3$  ms and  $26 \pm 1$  ms, respectively, *Student t-test*,  $p = 0.09$ ,  $t(160) = -1.706$ ).

Next, we applied a protocol allowing the detailed quantification of the MP-dependence of firing in individual cells ( $n = 81$  RS and  $85$  TOR cells). Specifically, firing was evoked by a current step that was calibrated for each cell to elicit similar average firing ( $10$ - $20$  Hz) from slightly depolarized MP. The holding current preceding the standard step was systematically varied to reach a wide range of steady-state MPs (3 seconds, in the range of  $-50$  and  $-90$  mV, Figure 10C). In TOR cells, the number of APs within the first 150 ms and the timing of the first AP showed steep voltage dependence ( $V_{1/2}$  value of the Boltzmann fits were  $-67.4$  mV and  $-73$  mV, respectively,  $R^2 = 0.995$  and  $0.999$ , Figure 10C). In contrast, the delay and number of spikes did not show MP-dependence in RS cells.

Unlike the initial spiking, the general firing and membrane properties of TOR and RS cells were similar, including input resistance ( $143 \pm 7$  M $\Omega$  vs.  $139 \pm 7$  M $\Omega$ ,  $n = 112$  TOR and  $n = 122$  RS cells, respectively), AP threshold ( $-37.4 \pm 0.4$  mV vs.  $-37.6 \pm 0.4$  mV), AP half-width ( $0.49 \pm 0.01$  ms vs.  $0.51 \pm 0.01$  ms),  $dV/dt$  maximum ( $484 \pm 13$  mV/ms vs.  $486 \pm 14$  mV/ms) and AHP amplitude ( $-15.5 \pm 0.3$  mV vs.  $-14.4 \pm 0.3$  mV). Furthermore, the frequency of spontaneous synaptic events (including both IPSCs and EPSCs;  $2.47 \pm 0.57$  Hz and  $3.26 \pm 0.86$  Hz,  $n = 9$  TOR and  $8$  RS cells) and amplitude of these events ( $-51.6 \pm 3.3$  pA and  $-51.5 \pm 2.5$  pA) were also similar. TOR cells were present in the CA1 region as well. However, here their prevalence was lower compared to CA3 (2 TOR out of 13 CA1 CCK+IN). Both TOR ( $n = 15$  cells) and RS ( $n = 12$  cells) CCK+INs were also detected in the CA3 region of adult rats (older than 70 days). In summary, the firing of TOR cells shows a remarkable sensitivity to a physiologically plausible 20 mV shift in the MP, despite having no other distinctive passive electrical or spiking properties compared to RS cells.

#### **4.2.2 TOR and RS firing types do not correlate with previously known subtypes of CCK+ cells**

The CCK+IN class has been previously divided into several subtypes based on various functionally relevant features. Therefore, next we investigated whether the two MP-dependent firing phenotype can be linked to previously known subtypes of CCK+INs. Three subtypes have been previously identified within CA3 CCK+INs based on the target zones of their axons. Basket cells (BCs) innervate the soma and proximal dendrites (Hendry et al., 1985). Mossy fiber-associated (MFA) cells are specific to the CA3 region where their axons colocalize with the axons of DG GCs in stratum lucidum and hilus (Vida et al., 2000). The third morphological type is named after the position of their axons as Schaffer collateral associated cells (SCA) (Cope et al., 2002). Altogether, 172 of the recorded CCK+INs were unequivocally identified either as BCs (n = 31), MFAs (n = 96) or SCAs (n = 45). Both TOR and RS firing types occurred similarly among these morphological subtypes (Figure 11B) indicating that the two firing phenotypes cannot be assigned to these morphology-based subtypes of CCK+INs.

In addition to the variable axonal morphology, CCK+INs are known to heterogeneously express several molecules (J. Somogyi et al., 2004). To compare their molecular content first we performed single cell RNA sequencing (SC-RNAseq) (Földy et al., 2016) of individually recorded TOR cells (n = 8) and RS cells (n = 9). Only those cells were analysed in detail, which had detectable mRNA for both CCK and cannabinoid-receptor type 1 (CB1R or *Cnr1*; Figure 11C). In accordance with previous observations (Földy et al., 2016), the included cells contained the transcripts of at least 3000 different genes. Most subtype-specific marker genes (calbindin/*Calb1*, vesicular glutamate transporter *VGlut3/slc17a8*, vasoactive intestinal protein/*VIP*, serotonin receptor type 3a/*5HT3a*, Reelin, neuropeptide-Y/*Npy*) were present at comparable levels in TOR and RS cells (Figure 11C),

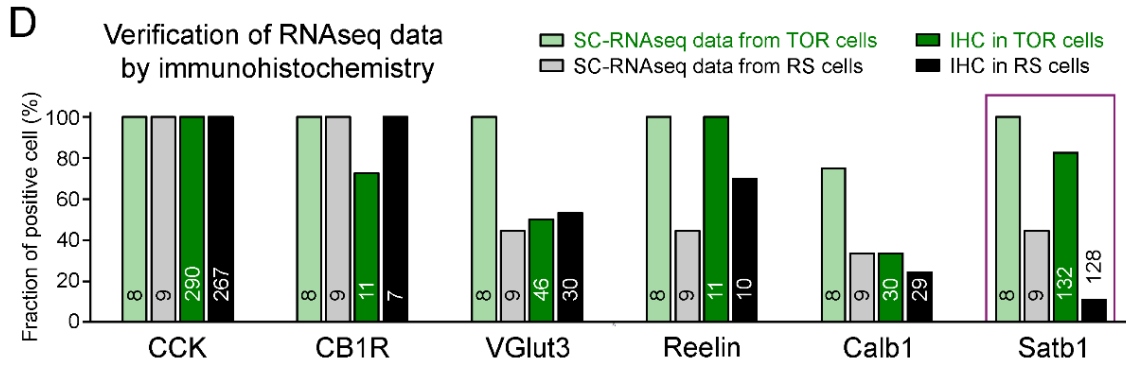
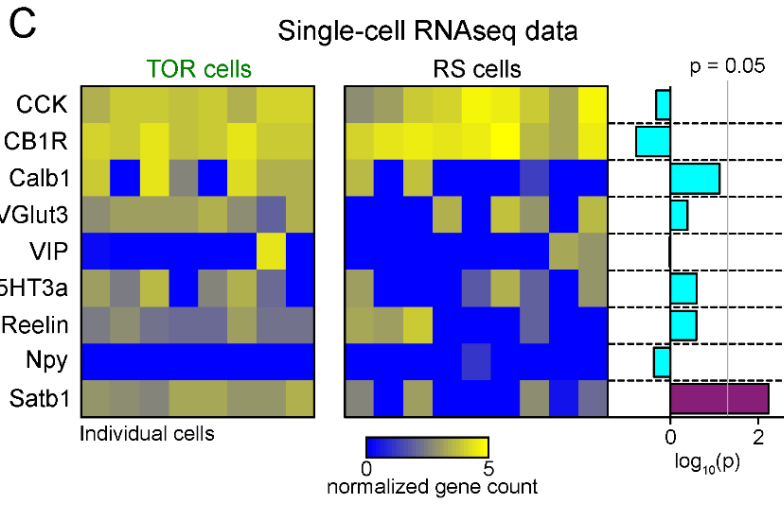
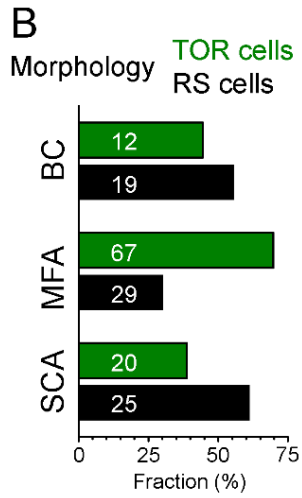
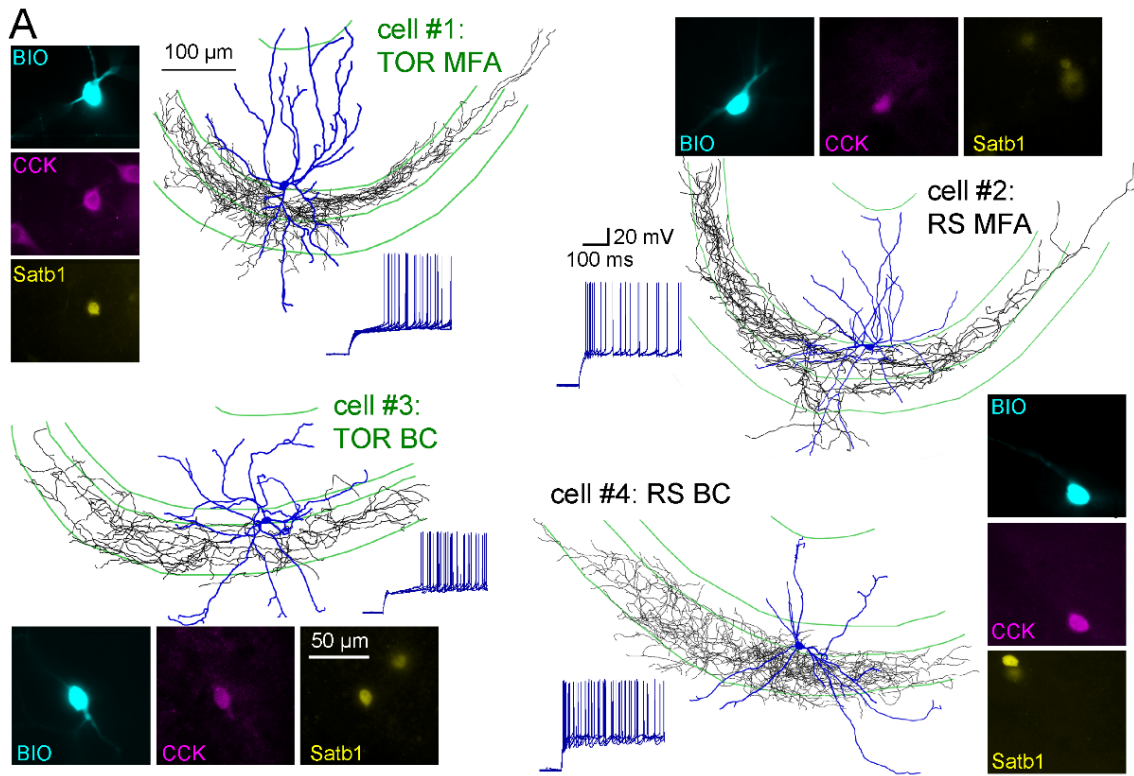


**Figure 11.** *Different excitability does not correlate with previously known diversity of CCK+ cells.*  
 A. Axonal (black) and dendritic (blue) reconstructions of four CCK+INs in the CA3 region representing two major morphological types, the mossy-fiber associated cells and basket cells. The firing of cell#1 and #2 are shown in detail in Figure 10. The firing from hyperpolarized MP is shown for each cell. Immunolabellings for CCK and the nuclear protein Satb1 are shown next to each recorded cell. B. Prevalence of TOR and RS cells within three major morphological types of CA3 CCK+. Numbers of identified cells are indicated on each bar (BC: CCK+ basket cells, MFA: mossy-fiber associated cells, SCA: Schaffer-collateral associated cells). C. Single cell RNAseq characterization of recorded TOR (left, n = 8) and RS (right, n = 9) cells for known GABAergic cell markers. Each column corresponds to single identified CCK+INs. Only Satb1 mRNA content was significantly different between TOR and RS cells ( $p = 0.00346$ , Mann-Whitney Test). D. Comparison of immunohistochemical and single cell RNAseq data. Bar plots show the fraction of the recorded cells with detectable RNA content (threshold: 0.2) for the selected markers and immunopositivity for the same proteins. The number of tested cells are shown on each bar.

except the activity-dependent transcription regulator, Satb1 (Close et al., 2012). All tested TOR cells had high levels of Satb1 mRNA, whereas it was present only in 4 of the 9 tested RS cells (*Mann-Whitney test*,  $p = 0.0058$ ,  $z = 2.76$ ,  $U = 65$ ).

To confirm these findings at the level of protein expression, next we performed immunohistochemistry on identified CCK+ TOR and RS cells in separate experiments (Figure 11D). As expected, CB1R protein was detected in the axon of almost all tested cells (15 out of 18 tested cells). Furthermore, VGluT3 (23 out of 46 TOR cells, 16 out of 30 RS cells), Reelin (all TOR, n = 11 and 7 out 10 RS was positive) and Calb1 (10 out 30 TOR and 7 out of 29 RS) proteins occurred similarly in RS and TOR types. However, the majority of the tested TOR cells were positive for Satb1 protein (109 out of 132, 82.6%) but only few RS cells were positive (14 out of 128 tested, 10.9%). Satb1 protein was also prevalent in non-recorded CCK+ cells within the CA3 region of the acute slices (126 Satb1+/CCK+ out of 425 CCK+), suggesting that the presence of this activity-dependent marker is not due to the recording. The somata of Satb1+/CCK+ cells were found throughout CA3 strata oriens, pyramidale, lucidum and radiatum and their proportion to all CCK+ cells were variable (34.1%, 21.4%, 33.6%, and 27.2%, respectively). In agreement with the lower occurrence of TOR cells in the CA1, non-recorded CCK+ cells in this region were less likely to be Satb1 positive (21.6% of 231 CCK+ cells). In the hilar region of the DG the proportion of Satb1+/CCK+ cells was also low (4.8% of 123 CCK+ cells). We have also detected Satb1

and CCK overlap in tissue samples derived from transcardially perfused animals (20.2%, 97 Satb1+/CCK+ out of 480 CCK+ cells in the CA3 area). Thus, the mRNA and immunohistochemical data suggest that the Satb1 content of hippocampal CCK+INs is predictive for their TOR or RS identity and these firing phenotypes are not related to previously known subtypes of the CCK+IN class.

#### **4.2.3 Differences in low-voltage-activated potassium currents ( $I_{SA}$ ) underlie the heterogeneity of CCK+IN firing**

Next, we investigated the conductances that are responsible for the difference of the two firing types in CCK+INs. We focused on near-threshold potassium currents, which can effectively regulate firing responses in similar experimental conditions in various brain regions (Lammel et al., 2008; Margrie et al., 2001; Neuhoff et al., 2002; Stern et al., 1996). First, we characterized each cell as TOR or RS type under normal recording conditions. Then, we blocked sodium (3  $\mu$ M TTX) and hyperpolarization-activated cation currents (10  $\mu$ M ZD7288) and recorded subthreshold potassium currents by applying 300 ms voltage command steps between -100 and -25 mV from -120 mV conditioning potentials (300 ms). All cells included in the analyses were verified to be CCK+ by *post hoc* immunolabelling. TOR cells had a substantial amount of potassium currents at firing threshold (Figure 12A,  $683 \pm 109$  pA at -40 mV). In contrast, potassium currents in RS cells activated at more positive voltages and were much smaller at threshold ( $148 \pm 28$  pA,  $p = 0.0006$ ,  $t(26)=3.885$ ,  $n = 17$  and  $11$ , *Student's t-test*). Because in these recording conditions the majority of the membrane conductances remained intact, voltage clamping could not be properly performed at more depolarized MPs, which precluded the determination of the exact half-activation voltage values. The robust low-voltage-activated potassium currents ( $I_{SA}$ ), which are activated tens of millivolts below AP threshold, can underlie the strong inhibition of AP generation in TOR cells, whereas  $I_{SA}$  in RS cells is much smaller at near-threshold voltage range.

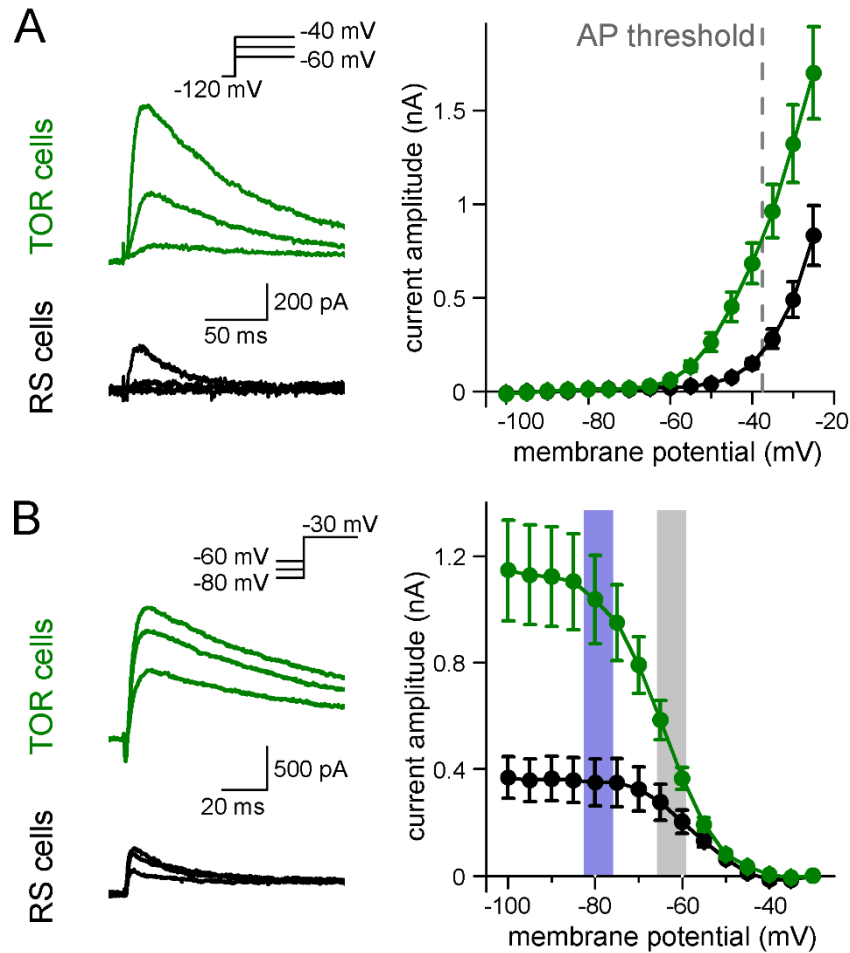


**Figure 12.** Differences in  $I_{SA}$  currents underlie the heterogeneity of CCK+IN firing.

A. Representative traces of low voltage activated potassium currents from TOR and RS cells (in the presence of 3  $\mu\text{M}$  TTX and 10  $\mu\text{M}$  ZD7288). Right, voltage dependence of activation of  $I_{SA}$  in TOR ( $n = 17$ ) and RS ( $n = 11$ ) cells. The grey dotted line indicates AP threshold ( $-37.52 \pm 0.3$  mV) measured before TTX application. Notice the large amount of outward current in TOR cells at subthreshold MPs. B. Representative traces of  $I_{SA}$  activated at -30 mV from different holding potentials. Right, voltage dependence of inactivation of  $I_{SA}$  in the two cell types ( $n = 14$  and 10 for TOR and RS cells respectively). Blue and grey shaded areas indicate the voltage ranges from which state-dependent firing was tested (see Figure 10).

Next, we investigated the availability of  $I_{SA}$  at different MPs. For these measurements, potassium currents were evoked by a voltage step to -30 mV following various pre-pulse potentials between -100 to -35 mV. The  $V_{1/2}$  of the average inactivation curve was  $-64.5 \pm 0.2$  mV (Boltzmann fit,  $R^2 = 0.999$ , mean of  $V_{1/2}$  from individual cells:  $-63.8 \pm 0.9$  mV,  $n = 13$  cells, Figure 12B) in TOR cells. Importantly, the majority of  $I_{SA}$  was



available at hyperpolarized MPs ( $91.3 \pm 1.6\%$  at  $-80$  mV), where the inhibition of firing was clearly observable during the characterization of TOR cells (see Figure 10 data). But at  $-60$  mV, where the inhibition of spiking was not prominent, the majority of outward currents in TOR cells were inactivated; only  $35.7 \pm 3.4\%$  of the current was available. Thus, the MP-dependence of the steady-state inactivation of  $I_{SA}$  can explain the TOR firing phenotype. Similar to the activation, the inactivation of  $I_{SA}$  in RS cells was shifted toward positive voltage ranges ( $V_{1/2}$ :  $-57.4 \pm 0.3$  mV,  $n = 8$  cells, mean of individual data:  $-55.6 \pm 2$  mV, comparison with TOR cells:  $p = 0.0006$ ,  $t(19)=4.12$ , *Student's t-test*) and a larger portion of  $I_{SA}$  remained available at  $-60$  mV in RS cells ( $52.7 \pm 6.3\%$ , Figure 12B). Thus, hyperpolarization of the RS cells cannot add a substantial amount of AP-firing disabling inhibitory conductance.

Interestingly, the inactivation time constant of  $I_{SA}$  was faster in RS cells compared to TOR cells ( $18.8 \pm 1.7$  ms vs.  $71.2 \pm 9.1$  ms, measured at  $-25$  mV,  $p = 0.0007$ ,  $t(19)=4.025$ , *Student's t-test*,  $n = 7$  and  $14$ ). Furthermore, the recovery from inactivation was faster in RS cells, but it showed steep voltage dependence in TOR cells (RS cells:  $11.8 \pm 4.4$  ms,  $8.0 \pm 2.2$  ms,  $7.1 \pm 1.6$  ms and  $3.3 \pm 0.4$  ms at  $-65$ ,  $-75$ ,  $-85$  and  $-120$  mV respectively, whereas in TOR cells: time constants of the recovery were  $58.2 \pm 2.9$  ms,  $46.2 \pm 2.9$  ms,  $29.8 \pm 2.5$  ms and  $4.4 \pm 0.1$  ms, respectively). Due to these properties,  $I_{SA}$  currents in RS cells resulted in only a small inhibitory charge transfer around the AP threshold, whose availability remains similarly limited within the relevant  $-80$  and  $-60$  mV MP range. Thus, the different properties of  $I_{SA}$  currents, particularly the left-shifted inactivation and activation curves and the different inactivation kinetics can explain the differences in TOR and RS firing phenotypes.

#### 4.2.4 Realistic models of TOR and RS firing

In the previous experiments, we injected simple steady-state currents to CCK+INs, which already revealed remarkably different excitability properties. However, excitation of neurons *in vivo* is more dynamic due to the fast rise and decay of PSPs that are clustered into packages according to the ongoing oscillatory state of the network, resulting in a constantly fluctuating MP. The different temporal properties of  $I_{SA}$  in TOR and RS suggest that these

cells can follow MP fluctuations differently. Therefore, to predict the frequency ranges of oscillations that are optimal for the distinct CCK+IN types with distinct excitability, we performed computer simulations of realistic dynamic behavior of RS and TOR phenotypes.

First, we equipped five reconstructed CCK+INs (3 TOR and 2 RS types) with known voltage-dependent conductances and passive properties of hippocampal CCK+INs (Bezaire et al., 2016) and reproduced the general firing properties (Figure 13). To add the  $I_{SA}$  currents

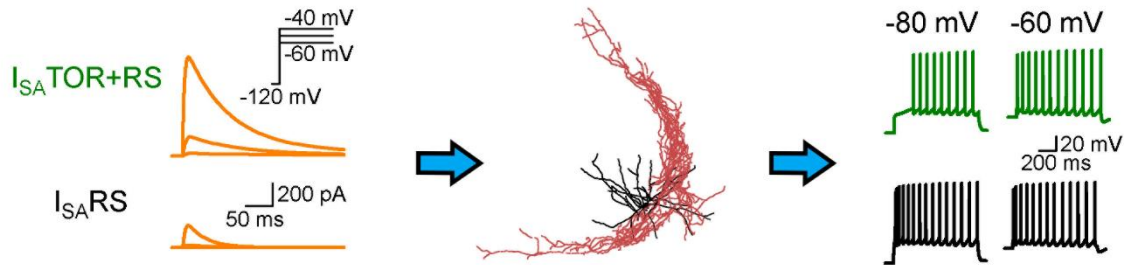


**Figure 13.** Construction of realistic single cell models.

$I_{SA}$ TOR+RS and  $I_{SA}$ RS were added to five reconstructed CCK+INs, which possess every known voltage-dependent conductance (Bezaire et al., 2016). Changing  $I_{SA}$ RS to  $I_{SA}$ TOR+RS in the same cells transformed the firing from RS to TOR phenotype. These simulated cells were equipped with synaptic conductance to simulate input drives in various network states.

to the models, we recorded the properties of local  $I_{SA}$  current by pulling outside-out patches from the soma and dendrites of RS and TOR cells (Figure 14). This additional experiment was necessary because the subcellular distribution of many ion channels are inhomogeneous (Nusser, 2009), which also influences the somatically measured ensemble currents.  $I_{SA}$  was isolated by subtraction of currents measured at 0 mV with -80 and -50 mV pre-pulses. We did not observe a significant gradient along the dendritic axis of the two cell types, albeit there was a tendency for larger somatic current densities compared to dendrites. The average kinetics of patch currents matched those of whole-cell currents: slower inactivation in TOR cells/patches. However, we detected a large variability of  $I_{SA}$  between individual patches from TOR cell (Figure 14D), even when multiple patches were pulled from the same cell. Patches from RS cells were more homogeneous (variance of current decays, TOR: 2888 ms<sup>2</sup>, RS: 373 ms<sup>2</sup>). Surprisingly, in many TOR cell patches the current kinetics resembled the patch- and whole-cell currents of the RS cells. While in other TOR cell patches much slower

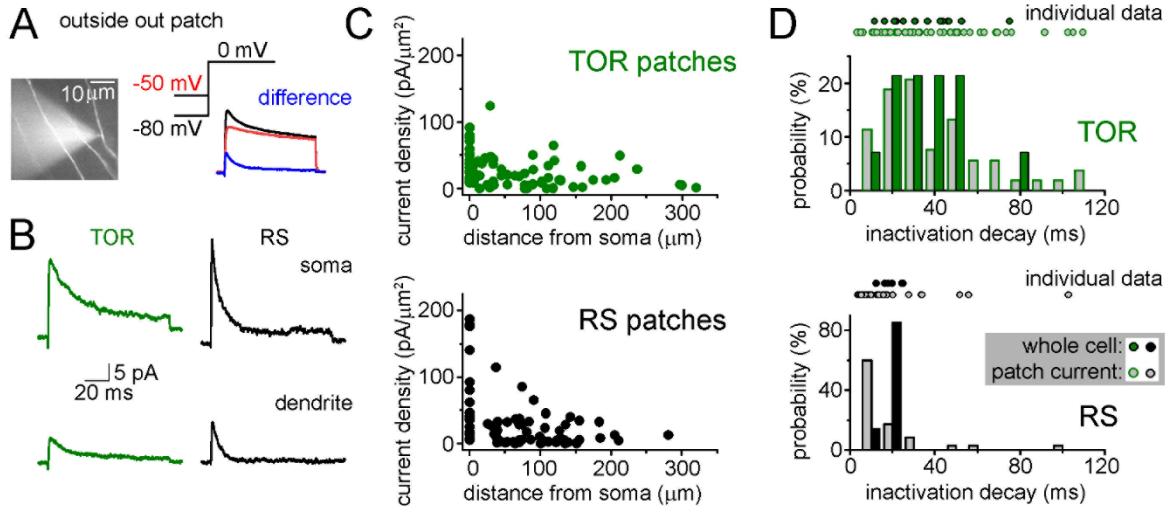


**Figure 14.** Mapping the somato-dendritic distribution of  $I_{SA}$ .

A. Representative outside-out patch recording of dendritic  $I_{SA}$  current from a RS cell, which was somatically loaded with Alexa594 dye to visualize dendrites in epifluorescent illumination and to record firing pattern.  $I_{SA}$  current (blue) was evoked at 0 mV and isolated by subtracting currents evoked with -80 mV prepulse voltage from -50 mV prepulse. B. Average  $I_{SA}$  currents from somata and dendrites of RS and TOR cells ( $n = 22$  somatic TOR-,  $n = 17$  somatic RS-,  $n = 56$  dendritic TOR and  $n = 53$  dendritic RS patches). C. Current densities are plotted against dendritic distance. Current densities were calculated by dividing the peak of  $I_{SA}$  current with the membrane surface of the patch, which was calculated from the capacitance difference measured with the patch membrane and after pushing the pipette in an insulator gel (Sylgard). D. Comparison of inactivation decay time constants of  $I_{SA}$  measured in individual whole-cell and outside-out recordings. Symbols above the graphs show individual measurements and their distributions are represented by bar graphs. Notice the wider distribution of patch data compared to whole-cell data from TOR cells.

currents were also detected. This variability might be due to the clustered occurrence of voltage-gated potassium channels in GABAergic cells (Kollo et al., 2006). We implemented this variability by equipping TOR models with two types of  $I_{SA}$  currents (for details see below).

These outside-out patch recordings also allowed us to directly compare the density of  $I_{SA}$  in TOR and RS cells because the majority of channels are expected to be open at larger voltage steps (to 0 mV) and the current amplitude is determined by the driving force and the conductance. Interestingly, the density of somatic  $I_{SA}$  in RS cells were significantly larger

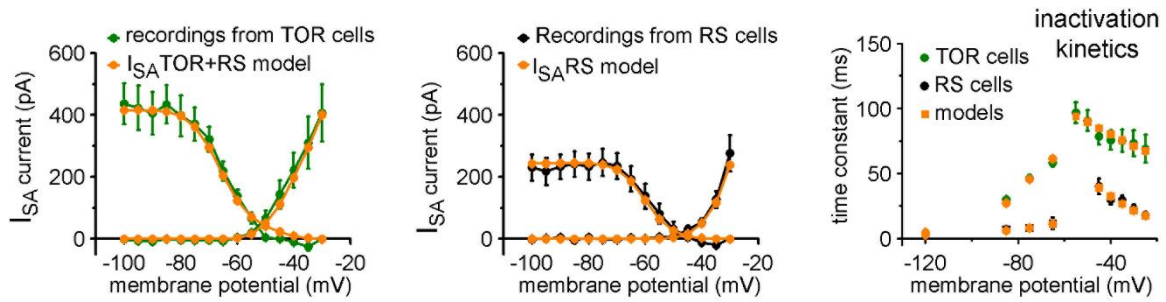


**Figure 15.** Model  $I_{SA}$  conductances accurately represent recorded  $I_{SA}$  kinetics and MP-dependence. VC simulations with complete morphology and realistic conductances reproduced whole-cell  $I_{SA}$  currents of TOR and RS cells, including voltage-dependence, the total current measured at the soma (left and middle graphs), and inactivation and the kinetics of inactivation and recovery from inactivation (right graph, where recovery was measured at -120, -85, -75 and -65 mV). Note that the total amount of  $I_{SA}$  in RS cells was larger than in TOR cells (4) and the larger current at low voltages are the consequence of the left-shifted activation curve.

compared to that of the TOR cells ( $70.5 \pm 15.2 \text{ pA}/\mu\text{m}^2$  vs.  $42.2 \pm 5.2 \text{ pA}/\mu\text{m}^2$ ,  $n = 26$  and  $17$ ,  $p = 0.047$ ,  $t(41) = -2.048$ ). This result does not contradict with the above data that the total  $I_{SA}$  current is larger in TOR cells near the AP threshold because in TOR cells the activation of  $I_{SA}$  is left-shifted, therefore, a larger fraction of channels is open at lower voltages. In dendritic patches (25-320  $\mu\text{m}$ ) the density of  $I_{SA}$  was similar in TOR and RS cells ( $19.6 \pm 3.3 \text{ pA}/\mu\text{m}^2$  vs.  $19.5 \pm 3.0 \text{ pA}/\mu\text{m}^2$ ,  $n = 53$  and  $47$ ).

Based on the results of the above recordings, we used two sets of  $I_{SA}$  conductances and tuned their densities to recreate RS and TOR firing properties in simulations. In the model, the recorded whole-cell  $I_{SA}$  potassium currents and firing properties were best represented if RS cells were equipped with a single type of  $I_{SA}$  potassium conductance ( $I_{SA}RS$ ). Whereas,  $I_{SA}$  currents of TOR cells were reproduced by a mixture of two  $I_{SA}$  potassium conductances, including  $I_{SA}RS$  and a left-shifted, slowly inactivating current ( $I_{SA}TOR$ ) in a 3:1 ratio. This mixed  $I_{SA}$  ( $I_{SA}TOR+RS$ ) is not only consistent with the variability of the patch current kinetics but also reproduces the properties of whole-cell currents (Figure 15). After adding  $I_{SA}RS$  or  $I_{SA}TOR+RS$  to the core CCK+IN properties (Bezaire et al., 2016) in current-clamp simulations, the models reproduced the common firing properties of CCK+INs (including AP width, peak and frequency and AHP shape), but in the presence of  $I_{SA}TOR+RS$  all five cells showed MP-dependent firing with similar temporal

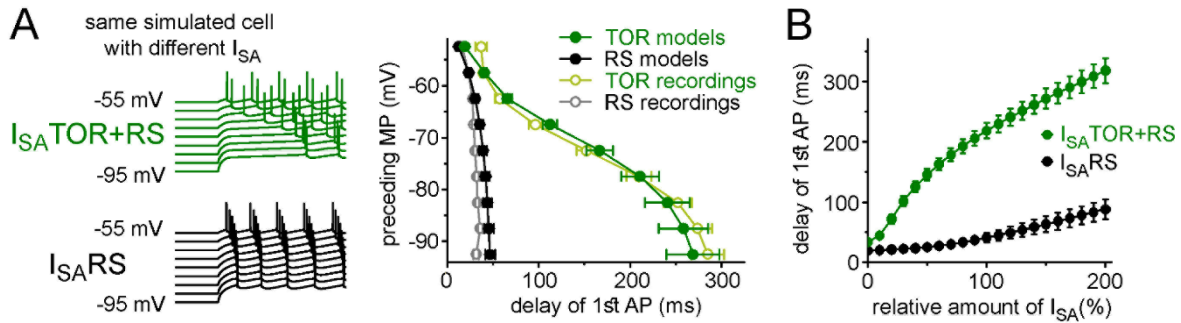


**Figure 16.**  $I_{SA}$  conductances constrained on VC recordings are able to recreate CC behavior of TOR and RS cells

A. Left, representative current-clamp simulations from a single model cell with either  $I_{SA}^{TOR+RS}$  or  $I_{SA}^{RS}$  currents. Notice the characteristic MP-dependence of spike onset with  $I_{SA}^{TOR+RS}$ . The graph on the right summarizes the MP-dependence of timing of the first APs from five model cells with either  $I_{SA}^{TOR+RS}$  or  $I_{SA}^{RS}$ . The results from recordings using the same protocols are shown for comparison (from 10, open symbols). B. Conductance density has little effect on the presence or absence and the extent of the TOR phenomenon suggesting that the kinetic and voltage-dependent properties of the two sets of  $I_{SA}$  currents play a more important role in this phenomenon than the amounts of inhibitory conductance (measured from -80 mV preceding MP).

dynamics and voltage dependence as recorded experimentally. When the same cells were equipped with  $I_{SA}^{RS}$  only, they turned to RS firing type (Figure 16). Thus, exchange of  $I_{SA}^{RS}$  to  $I_{SA}^{TOR+RS}$  alone is sufficient to generate TOR properties, even if the reconstructed cell originally belonged to the RS type and vice versa.

Surprisingly, these results also suggest that TOR firing required much less (57.5%)  $I_{SA}$  potassium conductance in total, than RS firing in the same reconstructed cells. This could be an additional consequence of the left-shifted activation of  $I_{SA}$  in TOR cells (further supports for this argument will follow below).

#### 4.2.5 TOR cells are selectively silenced by $I_{SA}TOR$ in a narrow range of oscillatory states

Next, we simulated the activity of RS and TOR firing cells during *in vivo*-like oscillating network conditions using excitatory and inhibitory inputs arriving onto the somato-dendritic axis of the five models of CCK+INs. The occurrence of excitatory events was clustered and tuned to frequencies ranging from 1 to 100 Hz and their kinetics were

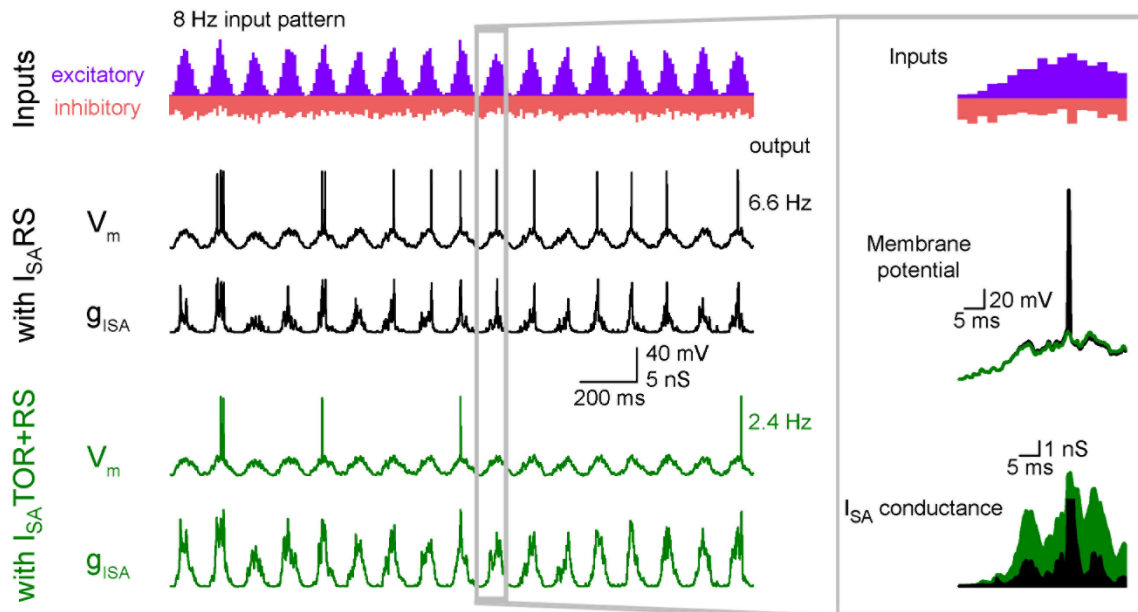


**Figure 17.** Measuring the behavior of TOR and RS models in physiologically relevant conditions.

A.  $I_{SA}TOR+RS$  and  $I_{SA}RS$  were added to five reconstructed CCK+INs, which possess every known voltage-dependent conductance (Bezaire et al., 2016). Changing  $I_{SA}RS$  to  $I_{SA}TOR+RS$  in the same cells transformed the firing from RS to TOR phenotype. These simulated cells were equipped with synaptic conductance to simulate input drives in various network states.

deducted from recordings from CCK+INs (see Methods). All five cells received the same input patterns and the strengths of excitation was varied (by changing the number of EPSCs, Figure 17), which resulted in a wide range of spiking frequencies in CCK+INs representing the frequency ranges that have been recorded *in vivo* (Klausberger et al., 2005; Lasztóczy et al., 2011).

Next, we compared the average spiking of  $I_{SA}TOR+RS$  potassium conductance-equipped CCK+INs ( $n = 5$  cells) with the spiking of the same cells during the same conditions except that they were equipped only with  $I_{SA}RS$ . As Figure 18 shows, in most conditions, the presence of  $I_{SA}TOR+RS$  instead of  $I_{SA}RS$  did not markedly reduce the firing rates. However, CCK+INs were efficiently silenced by  $I_{SA}TOR+RS$  in 8-15 Hz input frequency regimes. On average,  $39.1 \pm 0.6\%$  fewer APs were evoked (see red areas in the middle of the Figure 18 graph and example traces). In contrast, during lower and higher input regimes the presence

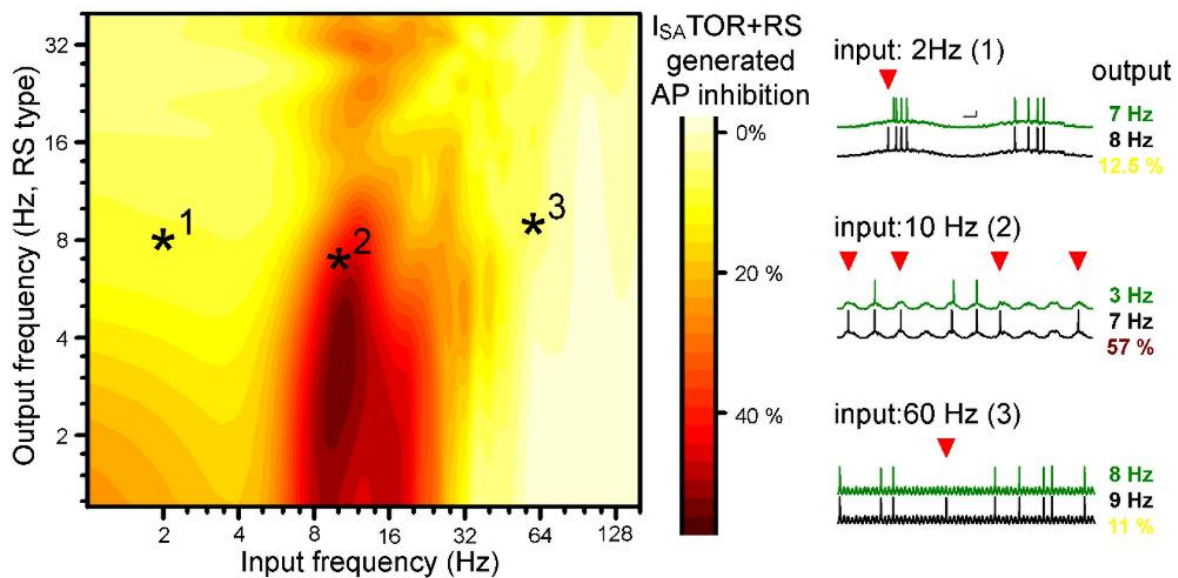


**Figure 18.** *Different  $I_{SA}$  currents in TOR and RS cells tune them for different network states.* Average effects of exchanging  $I_{SA}RS$  to  $I_{SA}TOR+RS$  on the output of five CCK+INs during various input frequency ranges (x-axis) and baseline output activity (i.e. with  $I_{SA}RS$  conductance, y-axis). Yellow color shows no change in firing when  $I_{SA}TOR+RS$  replaced  $I_{SA}RS$ , whereas red color indicates robust reduction in AP output. Representative traces on the right depict three examples with different input frequencies. Red triangles highlight inhibited spikes.

of  $I_{SA}TOR+RS$  reduced firing only slightly (spiking was decreased by  $8 \pm 0.3\%$  and  $7.5 \pm 0.2\%$ , between 1-6 Hz and 25-100 Hz).

Thus, the results of these simulations suggest that  $I_{SA}TOR+RS$  conductance alone enables CCK+INs to be selectively silenced during 8-15 Hz input regime, which adds a novel level of complexity to the diverse functions of GABAergic cells and can contribute to their observed heterogeneous firing during different network states (Klausberger et al., 2008;



Lasztóczy et al., 2011; P. Somogyi et al., 2005). The input frequency dependence of the inhibition of firing can be explained by the specific temporal properties of  $I_{SA}$ TOR+RS. Specifically, in addition to the voltage dependence of activation and inactivation (Figure 12), the time constant of inactivation (Figure 14D) and the recovery from inactivation determines the different availability of these currents during various oscillatory states. Thus, minor modifications in the properties of  $I_{SA}$  enabled distinct functions in individual cells that otherwise belong to the same neuronal class.

#### 4.2.6 Kv4 channels are responsible for both types of $I_{SA}$ currents in CCK+INs

Next, we investigated the identity of potassium channel subunits responsible for the differences of  $I_{SA}$  in RS and TOR cells and for the MP-dependent firing in TOR cells. Neither TEA (0.5 and 10 mM, blocking Kv3 channels) nor low concentration of 4-AP (100  $\mu$ M, blocking Kv1 and Kv3 channels) eliminated the initial firing gap in TOR cells (Figure 19). Only a high concentration of 4-AP (5 mM) was able to diminish the TOR phenomenon in CCK+INs. These results, together with the low voltage activation properties, suggest a key role for Kv4 channels (Lien et al., 2002). Kv4.3 has been shown in hippocampal CCK+INs (M. L. Bourdeau et al., 2007; Kollo et al., 2006). To specifically test the contribution of Kv4 channels to the TOR phenomenon, we applied Heteropodatoxin-1 (HpTX, 1  $\mu$ M), which selectively, but only partially, blocks Kv4.2 and Kv4.3 subunit-containing channels (DeSimone et al., 2011; Sanguinetti et al., 1997). In the presence of HpTX, significantly more APs were evoked in TOR cells during the first 125 ms of the stimulus compared to control conditions in the same cells before HpTX application (Figure 20A, from -80 mV preceding MP,  $9.7 \pm 2.9\%$  vs  $5.1 \pm 2.2\%$ , HpTX and control respectively,  $p=0.0037$ ,  $t(5)=-5.12$ , paired *t-test*). Furthermore, the delay of the first APs was reversibly shortened from  $239 \pm 61$  ms to  $116 \pm 38$  ms (Figure 20B,  $p = 0.01$ ,  $t(7)=3.493$ , paired *t-test*,  $n = 8$  TOR cells). However, HpTX did not change the number and temporal distribution of APs in TOR cells from -60 mV (data not shown), nor the firing of RS cells neither at -80 nor -60 mV. HpTX did not influence the half-width of the APs (TOR cells: control:  $0.48 \pm 0.02$  ms, HpTX:  $0.52 \pm 0.03$  ms,  $p = 0.15385$ ,  $t(7) = -1.59901$ ,  $n = 8$ ; RS cells: control:  $0.55 \pm 0.04$  ms HpTX:  $0.59 \pm 0.06$



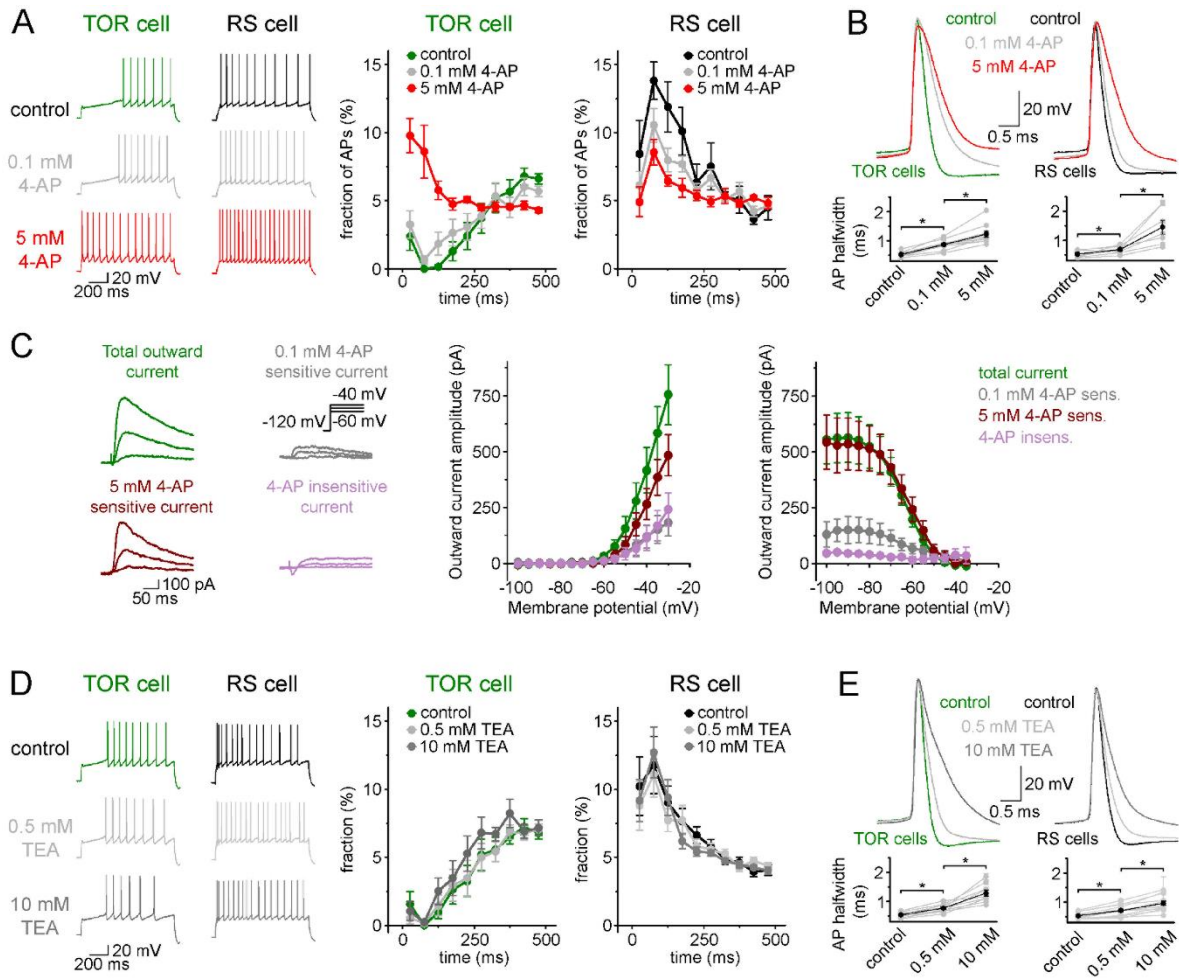


**Figure 19.** TOR phenomenon is not affected when *Kv1* and *Kv3* channels are inhibited.

A. Inhibition of spiking in TOR cells was eliminated by only a high concentration of 4-aminopyridine (4-AP, 5 mM, red traces), but not by low concentration (0.1 mM, grey traces). B. As expected, both low and high concentrations of 4-AP affect AP width and threshold due to blockade of various potassium channels (grey symbols represent individual experiments, black symbols show average results). C. Representative traces on the left show control and 4-AP-sensitive and insensitive currents from a TOR cell and the graphs show the average voltage dependence of these components ( $n = 5$  TOR cells). Majority (64.2% at -30 mV) of outward currents in TOR cells are sensitive to high, but not to low concentration 4-AP. D. Firing patterns of TOR and RS cells are not affected by low (0.5 mM, light grey) and high concentrations (10 mM, dark grey) of tetraethylammonium (TEA,  $n = 9$  TOR and  $n = 13$  RS cells). E. The effect of TEA on AP shape of TOR and RS cells (\*:  $p < 0.05$ , paired sample t-test).

ms,  $p = 0.11016$ ,  $t(7) = -1.82865$ ,  $n = 8$ ). Thus, HpTX-sensitive, *Kv4*-mediated currents are crucial for the TOR phenomenon.

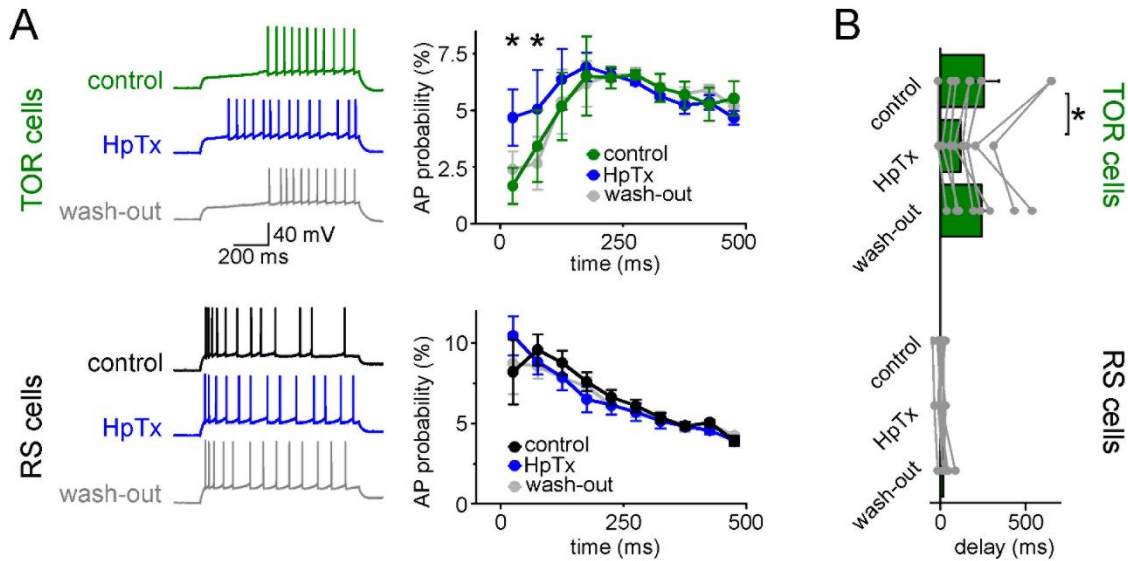


**Figure 20.** Blockade of *Kv4* channels selectively inhibits TOR phenomenon.

A. Representative CCK+INs firing patterns recorded before, during and after HpTx application (in response to identical current steps) and the average AP probabilities in TOR ( $n = 6$ ) and RS cells ( $n = 9$ ) from hyperpolarized MP ranges ( $-82$  to  $-77$  mV). B. Average delay of the first AP and reversible effect of HpTx. Connected symbols represent individual measurements (paired t-test:  $p = 0.01008$ ).

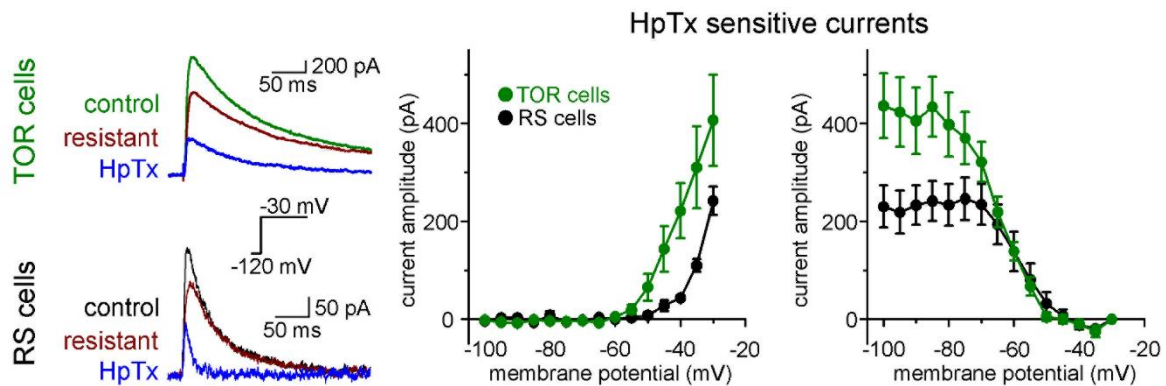


**Figure 21.** Both TOR and RS cells possess *Kv4* mediated currents.

HpTx-sensitive  $I_{SA}$  in representative TOR and RS cells (left) and the average voltage dependence ( $n = 7$  for both TOR and RS cells).

Next, we analysed the contribution of HpTx-sensitive currents to  $I_{SA}$  in TOR and RS cells. Both types had substantial amounts of HpTx-sensitive currents. However, their properties were different in TOR and RS cells similarly as seen for their total  $I_{SA}$ . In TOR cells, the HpTx-sensitive current activated at more negative voltage than in RS cells (Figure

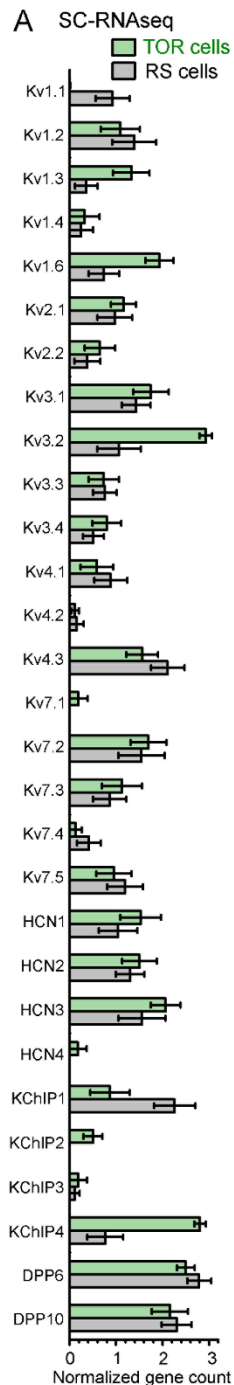


**Figure 22.** Core- and auxiliary potassium channel subunit transcriptome of TOR and RS cells.

Normalized gene count of primary and auxiliary subunits of voltage-gated potassium channels from single cell RNAseq data of TOR (n = 8) and RS (n = 9) cells.

21). The time constant of inactivation of the HpTX-sensitive currents was slower in TOR cells than in RS cells ( $49.1 \pm 12.6$  ms, and  $11.8 \pm 1.6$  ms, respectively, at  $-25$  mV). The voltage dependence of inactivation of the HpTX-sensitive current was also left-shifted in TOR relative to RS cells ( $V_{1/2}$  TOR:  $-64.0 \pm 0.6$  mV, RS:  $-56.8 \pm 1.3$  mV). Considering the similar kinetics and voltage dependence of total and HpTX-sensitive  $I_{SA}$  currents and the partial Kv4-blocking ability of HpTX (DeSimone et al., 2011; Sanguinetti et al., 1997), these results suggest that the majority of inactivating  $I_{SA}$  potassium currents in both types of CCK+INs are mediated by Kv4 channels.

Next, we tested the presence of Kv4 channels in RS and TOR cells using the above SC-RNAseq data (Figure 22 and 23). Kv4.2 was absent in most of the tested 17 CCK+INs confirming previous findings (M. L. Bourdeau et al., 2007; Rhodes et al., 2004). The mRNA of Kv4.3 subunits was detected in most CCK+INs (16 out of 17 cells), including both RS and TOR types, in agreement with the findings that both RS and TOR cells have HpTX-sensitive currents. Interestingly, in line with the predictions of the simulation, the average RNA copy number of Kv4.3 was slightly higher in the tested RS cells compared to TOR cells. Note that the SC-RNAseq data revealed differences in additional Kv channels between RS and TOR cells such as Kv3.2, Kv1.3 and Kv1.6 subunits (Figure 22). Because these subunits do not generate low-voltage-activated, inactivating currents, we did not perform experiments to investigate the currents generated by these subunits (Lien et al., 2002) (Figure 19). We next performed immunohistochemistry to localize Kv4.3 subunits in biocytin-filled TOR and RS

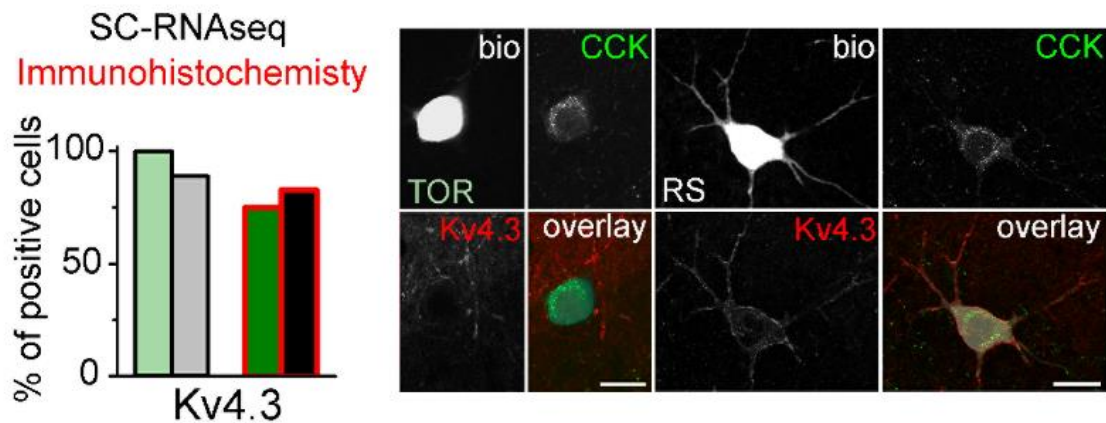


**Figure 23.** Similar *Kv4.3*-expression in *CCK+INs*.

**A.** Normalized gene count of primary and auxiliary subunits of voltage-gated potassium channels from single cell RNAseq data of TOR (n = 8) and RS (n = 9) cells.

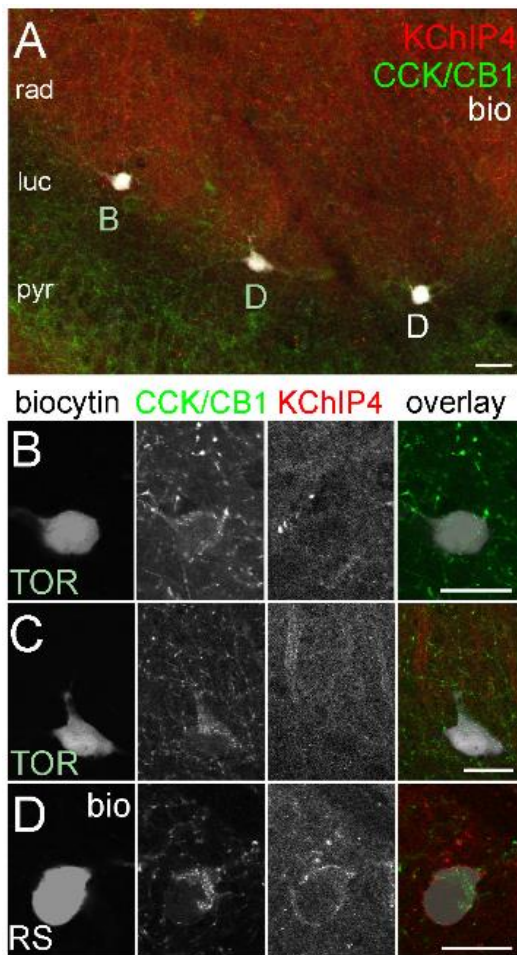


**Figure 24.** *Kv4.3* and *KChIP* immunohistochemistry in perfusion or immersion fixed CA3 slices.

**A.** Low magnification image showing simultaneous immunolabelling of *KChIP4* (red) and *CCK/CB1* (green) in an acute CA3 slice, in which a RS cell and two TOR cells were filled with biocytin (left) at the border of strata radiatum/lucidum in CA3a. Intense *KChIP4* immunolabelling is present in the neuropil of stratum radiatum mainly associated with dendrites of PCs (Rhodes et al., 2004). B-D. High magnification images showing an enlarged view of the biocytin filled cells shown in (A). *KChIP4* is not detectable in the two TOR cells (B, C), but its weak presence was detected in the neighbouring the RS cell (D), but. Scale bars: 20  $\mu$ m.

cells. In general, we observed an intense neuropil labelling for *Kv4.3* in DG, CA3 strata radiatum and oriens, but not in the CA1 area. A subset of INs were also labelled throughout the hippocampus (M. L. Bourdeau et al., 2007; Rhodes et al., 2004). *Kv4.3* proteins appeared to be enriched in the somatic and



dendritic plasma membranes, but the subcellular distribution was often uneven and clustered (Figure 23 and 24) in line with the known distribution pattern of the Kv4.3 subunits (Kollo et al., 2006). In agreement with the pharmacological and SC-RNAseq data we detected Kv4.3 proteins (Figure 23) in both TOR (15 out of 20 tested cells) and RS CCK+INs (19 out of 23 cells). However, the immunosignal for Kv4.3 was usually stronger in RS than in TOR cells even within the same sections. This tendency was also seen in the CA3 area obtained from perfusion-fixed brain (Figure 24 where Kv4.3 signal was detectable at strong or moderate level in most CCK/Satb1- cells (putative RS cells, 99%, 338 out of 342 tested cells), whereas the labelling was weak or hardly detectable in most CCK/Satb1+ cells (putative TOR cells, 97%, 78 out of 80 tested cells). TOR and RS cells not only possess Kv4.3-mediated  $I_{SA}$  with different activation and inactivation kinetics, but TOR cells seem to achieve larger charge transfer via lower density of Kv4.3 channels. What could mediate such differences?

#### 4.2.7 Auxiliary subunits of Kv channels in TOR and RS cells

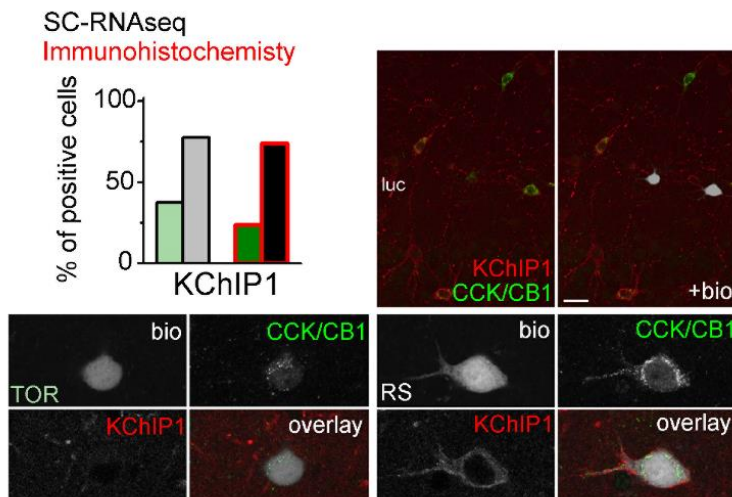


**Figure 25.** Different *KChIP1* content in CCK+INs.

Percentage of recorded cells with detectable levels of *KChIP1* mRNA (n = 8 and 9 cells) and proteins (n = 20 and 27 cells). At the right and in the bottom, immunofluorescent co-localization of CCK with CB1 (green) and *KChIP1* in a TOR

Core Kv4 channel proteins form ternary complexes with dipeptidyl aminopeptidase-like proteins (DPLPs, including DPP6 or DPP10) and K<sup>+</sup> channel interacting proteins (KChIP1-4 from Kcni1-4 genes), which fundamentally change the current properties. The modulatory effects are highly variable and depend on the type and splice isoforms of the available auxiliary subunit. For example, most KChIP isoforms enhance surface expression and accelerate inactivation and recovery from inactivation (Henry Hungtao Jerng et al., 2014; Pongs et al., 2010). However, the so-called transmembrane KChIPs (tmKChIPs) have opposite effects as they can retain Kv4 from the plasmamembrane and decelerate inactivation (Holmqvist et al., 2002; Henry H Jerng et al., 2008; Henry Hungtao Jerng et al., 2014; Pruunsild et al., 2012). KChIP1, as one of the classical KChIPs, accelerates inactivation and increases surface expression of Kv4.3 channels (Beck et al., 2002; M. Bourdeau et al., 2011; Henry Hungtao Jerng et al., 2014; Pongs et al., 2010). We detected KChIP1 mRNA in most RS cells (7 of 9 tested), but it was absent in 5 out of 8 TOR. The average mRNA level was

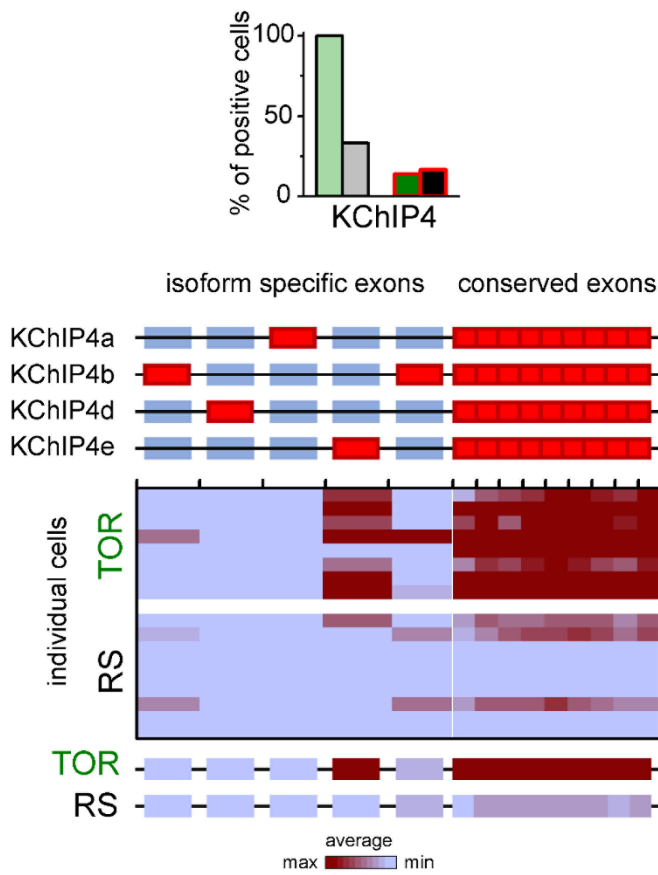


**Figure 26.** *Different KChIP4 isoform content in CCK+INs.*

Major KChIP4 splicing isoforms consist of different exons in the N-terminal region (represented as red boxes). Each row represents a single cell in the color-mapped data and columns correspond to individual exons aligned to the schematic illustration of isoforms above. Red and blue colors code high and low mRNA levels, respectively. The average exon counts from the two types of CCK+INs (n = 8 and 9) are shown at the bottom using the same color code scheme.

significantly higher in RS than in TOR cells ( $2.26 \pm 0.44$ , TOR:  $0.87 \pm 0.42$ , Mann-Whitney,  $p = 0.013$ ,  $z = -2.475$ ). Detection of the KChIP1 protein by immunohistochemistry revealed an even clearer distinction between RS and TOR cells (Figure 25). The KChIP1 protein was detected in the majority of tested RS cells (20 out of 27), whereas only few TOR cells showed positive immunoreaction (5 out of 21) and the signal in these cells was weaker than in RS cells (Figure 25). KChIP1 signal was present not only in the plasma membrane but also in the cytosol, in agreement with their trafficking role (Pongs et al., 2010). This data from recorded cells were confirmed by the analysis of CCK+INs in perfusion fixed brains. We detected strong KChIP1 signal in the majority of CCK+/Satb1- cells (corresponding to RS cells, 122 out of 132 tested cells, 92.4%). In contrast, only 4.9% of CCK+/Satb1+ cells (corresponding to TOR cells, 2 out of 41 tested cells) showed strong KChIP1 immunosignal. We did not detect significant amounts of KChIP2 and KChIP3 mRNAs in CCK+INs.

The universal mRNA sequence of KChIP4s was detected in all TOR cells (8 out of 8), whereas it occurred in 3 out of 9 RS cells. The available antibody detected KChIP4 protein only in a very few CCK+INs regardless of their firing type (4 out of 29 TOR, 5 out of 30 RS cells, Figure 26 and 24), thus, our observation with immunohistochemistry apparently contradicts the mRNA data. In general, the relatively weak KChIP4 immunosignal in CCK+INs were surrounded by strong neuropil labelling in the stratum radiatum (Figure 24). While KChIP1 is expressed only in INs, KChIP4 is known to be associated with Kv4.2 channels in PCs as well (Rhodes et al., 2004). This is in accordance with our observation of KChIP4 immunosignal at high magnification (Figure 24), where it appears associated with tube-like structures, likely representing the plasma membranes of putative PC dendrites. However, our KChIP4-specific antibody was raised against a long amino acid segment, which includes the highly variable N-terminal region, which endow the various KChIP4-isoforms with different effects on Kv4 channel function (Holmqvist et al., 2002; Henry H Jerng et al., 2008; Henry Hungtao Jerng et al., 2014; Pruunsild et al., 2012). Therefore, we further analysed the mRNA data at the level of individual KChIP4 exons (Figure 26). We detected the KChIP4e isoform-specific exon in 7 TOR cells (out of 8 tested). KChIP4e belongs to the so-called transmembrane KChIPs (tmKChIPs) (Henry H Jerng et al., 2008), which, in contrast to most KChIP types and isoforms, do not promote the plasma membrane

expression of Kv4 and have opposite effects on the inactivation kinetics (Henry H Jerng et al., 2008; Pruunsild et al., 2012). KChIP4b, which acts as classical KChIPs, was detected in only one TOR cell (from 8 tested). KChIP4e specific exons were detected only in one RS cell. The two other RS cells that also had a small amount of KChIP4, expressed the KChIP4b isoform. Altogether, these data indicate that RS cells express KChIP1, whereas TOR cells primarily express KChIP4e. We suggest that the differential influences of these auxiliary subunits underlie some of the distinct properties of  $I_{SA}$  in RS and TOR cells because KChIP1 is known to accelerate inactivation and increase surface expression, whereas tmKChIPs, such as KChIP4e, do not facilitate Kv4 plasma membrane trafficking and confer slow channel inactivation.

KChIPs alone cannot account for all differences between  $I_{SA}$  currents in TOR and RS cells, including differences in voltage-dependence. DPP10 and DPP6 proteins effectively shift the voltage dependence of Kv channel activation and inactivation (Henry H Jerng et al., 2007; Henry H Jerng et al., 2012; Henry Hungtao Jerng et al., 2014; Nadal et al., 2003; Pongs

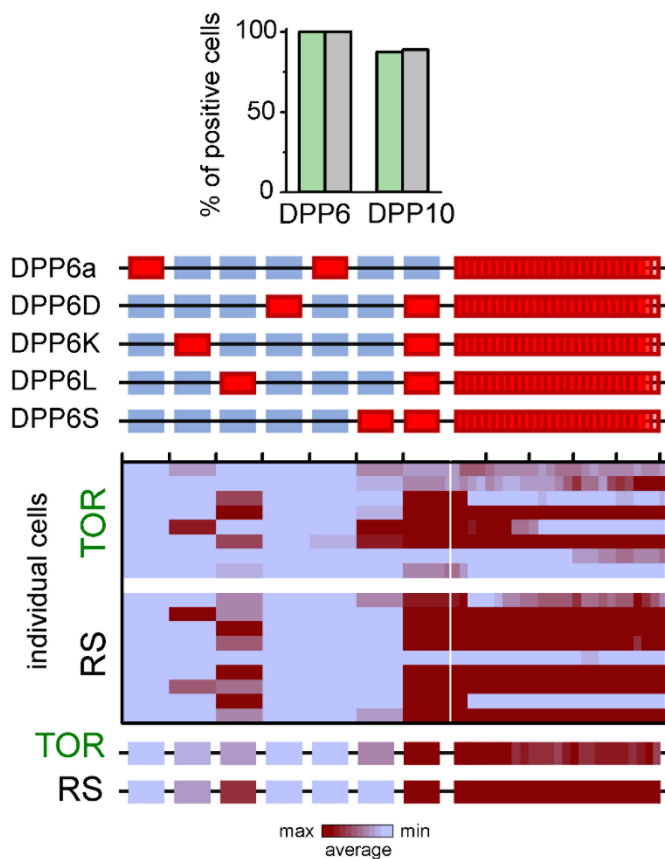


**Figure 27.** Different DPP isoform content in CCK+INs. Percentage of recorded cells with detectable levels of DPP6 and DPP10 mRNA. At the bottom, assembly of major DPP6 isoforms and exon levels in individual CCK+INs are shown in figure 26.



et al., 2010). Therefore, next we analyzed the expression of these molecules at the mRNA level (Figure 27). DPP10 (conserved segments) was present in both TOR and RS cells (7 out of 8, and 8 out of 9 cells, respectively). The DPP10c isoform was detected in significant amounts in all cells regardless of their firing type. DPP6 was also detected in most CCK+INs from both types. The primary isoform in RS cells was the DPP6L. In contrast, DPP6S isoform occurred in most TOR cells (7 out of 8 cells) and DPP6L-specific exons were also detected in several cells (4 out of 8 TOR cells). Thus, in addition to KChIPs, expression of DPLP-isoforms correlates with the firing types of CCK+INs and their combined modulatory effects may underlie the different properties of Kv4.3-mediated  $I_{SA}$  currents, which is responsible for their different excitability.

## **4.3 Small size of recorded neuronal structures constrain the accuracy of voltage measurements**

### **4.3.1 Model implementation of extracted amplifier features**

Accurate representation of the experimental conditions requires the knowledge of numerous cellular and instrumental parameters. Although these parameters can be gained from different VC and CC measurements, commands always induce instrumental artefacts that can substantially alter the recorded signal.

To realistically reproduce model amplifier responses, we collected data about the behavior of the amplifier using three different test configurations, which allow the estimation of isolated circuit elements (Figure 28A, see Methods section for details). The obtained parameters of the amplifier were implemented into a realistic model using the NEURON simulation environment (Hines et al., 1997). Model amplifier construction started from idealized circuit representations, namely from a resistive feedback circuit typical for the VC and an ideal voltage follower circuit for the CC. Then, we supplied the circuits with additional elements and tuned its parameters to reproduce specific behaviors of the real amplifier (in our case, the MultiClamp 700B, see Methods section for the details).

One critical aspect in the VC model construction was the temporal resolution. In an ideal feedback circuit, the rise of the command determines the speed of the VC responses. However, the presence of the experimentally determined stray capacitance associated with the feedback resistor substantially slows down the operation of the model current-to-voltage converter compared to real VC responses. (Figure 29A, time constant of the capacitive relaxation of the ideal amplifier: 10  $\mu$ s, with stray capacitance: 191.92  $\mu$ s). To overcome this, amplifiers usually have a dedicated high frequency boost circuit, which increases the frequency bandwidth of the responses. Therefore, we extended our VC circuit model with a simplified boosting unit (Sigworth, 1995) which was tuned to accelerate model responses to the experimentally observed amplifier speed (Figure 29A, 3.85  $\mu$ s vs 3.19  $\mu$ s real vs boosted

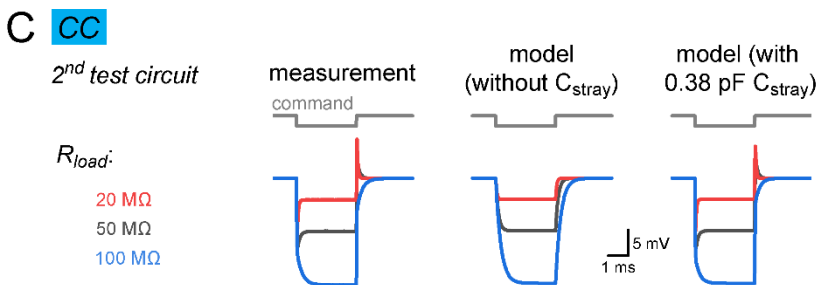
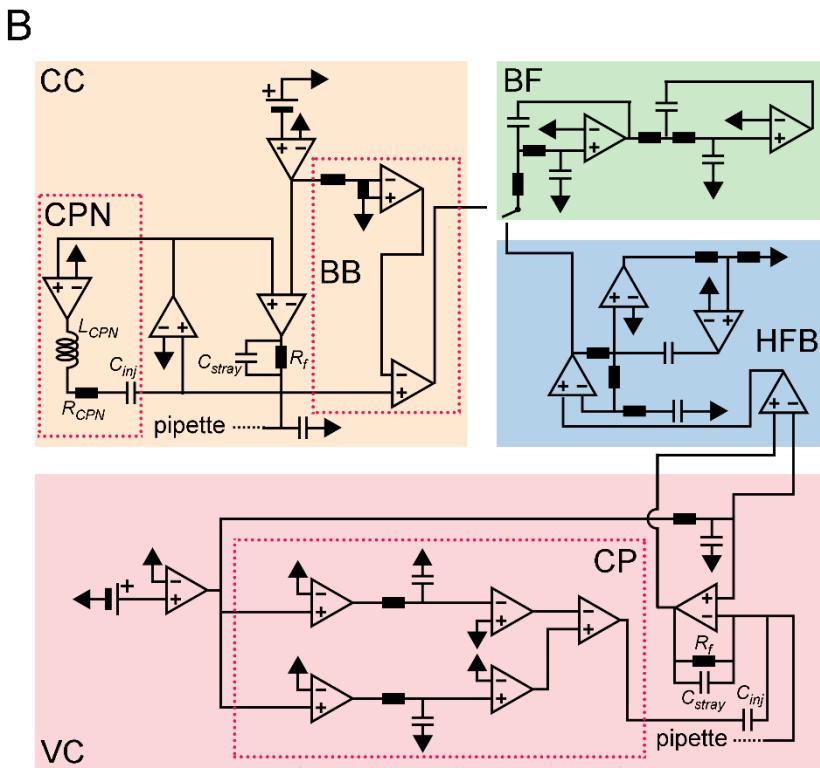
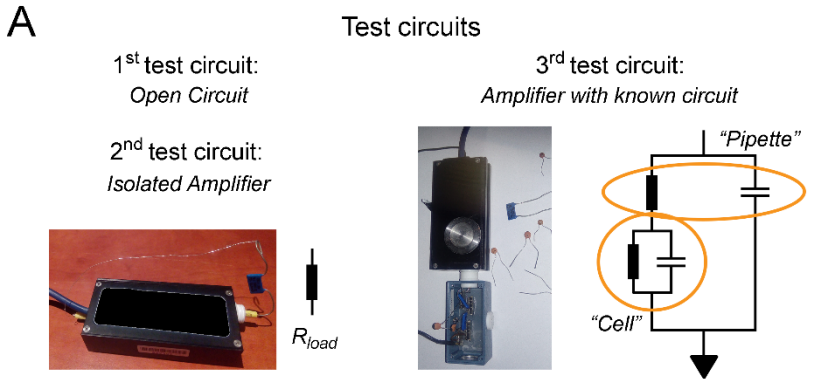


**Figure 28.** Construction of the measurement-based phenomenological model amplifier

A. Test circuits used for the characterization of the circuit components. B. Circuit diagram of the model amplifier consisting of simple linear circuit elements. CC: current clamp block, VC: voltage clamp block, HFB: high frequency boost circuit, BF: Bessel filter, CPN: capacitance neutralization circuit, BB: bridge-balance circuit, CP: capacitance compensation block. See the Methods section for more details. C. Measurements with the 2<sup>nd</sup> test circuit indicate the presence of a stray capacitance on the feedback resistor ( $R_f$ ), which was reproduced by the model implementation of  $0.38 \text{ pF}$  stray capacitance ( $C_{stray}$ ). Left panel shows measurements with different load resistances at the amplifier input, the middle panel shows modelled voltage responses without  $C_{stray}$ , model responses on the right were generated with implemented  $C_{stray}$ .

model). Additionally, as VC recordings

employ pipette capacitance compensation to avoid amplifier saturation, we implemented two

compensatory circuit units working on different timescales, similarly as in the real amplifier (Figure 29B, fast cancellation, CPf: 0.5 - 1.5  $\mu$ s and slow cancellation, CPs: 10 - 4000  $\mu$ s).

The CC model consists of a voltage follower operational amplifier and a current source with capacitance neutralization (CPN) and bridge balance (BB) compensation circuits (Figure 28B). Ideally, CC recordings should be carried out with maximally neutralized instrumental capacitance, however, by definition, voltage oscillates as the CPN reach complete compensated level due to the positive feedback loop. The level of neutralization where the recording is still stable, the dampening of the oscillatory behavior and the frequency profile of the full-scale oscillation are features specific of the amplifier. To implement these CPN characteristics, we simulated whole cell recording conditions and evoked voltage responses by brief current injections in a modified and customizable model cell (Figure 29C, Figure 28). First, we determined the maximal level of neutralization ( $CPN_{max}$ ) that can be attained without generating voltage oscillations. We observed that neutralizing capability of the amplifier crucially depends on the cellular capacitance ( $C_{cell}$ ) because  $CPN_{max}$  became larger as the  $C_{cell}$  decreased resulting in  $\sim 1.5$  pF difference in the  $CPN_{max}$  for the same instrumental capacitance (Figure 29D,  $CPN_{max}$  at 47 pF  $C_{cell}$ : 5.638 pF,  $CPN_{max}$  at 0.75 pF  $C_{cell}$ : 7.166 pF). We also found a correlation between the cellular input resistance ( $R_{in}$ ) and the  $CPN_{max}$  because at a given cellular capacitance the value of  $CPN_{max}$  was larger as the  $R_{input}$  increased ( $CPN_{max}$  at 100 M $\Omega$   $R_{input}$ : 6.75 pF vs.  $CPN_{max}$  at 10 G $\Omega$   $R_{input}$ : 7.44 pF, measured at 0.75 pF  $C_{cell}$ , not shown). Next, we investigated the potential relationship between the pipette resistance and the CPN performance (Figure 29E). In case of the small structure,  $CPN_{max}$  was independent of the  $R_{pip}$ , however, for larger  $C_{cell}$  the  $CPN_{max}$  increased together with the  $R_{pip}$ . As a result, structure-size-dependent differences in the  $CPN_{max}$  disappeared at higher  $R_{pip}$  range ( $>100$  M $\Omega$ ). Altogether, we found that CPN performance of the amplifier is not a fixed characteristic, but varies according to the electrical properties of both the recorded cell and the recording electrode. Having established the key features of the CPN in the amplifier, we implemented the CPN circuit to the CC model (Figures 29C and D, Figure 28B). Amplifiers are typically supplied with additional BB compensatory mechanism to compensate for the voltage offset caused by the access

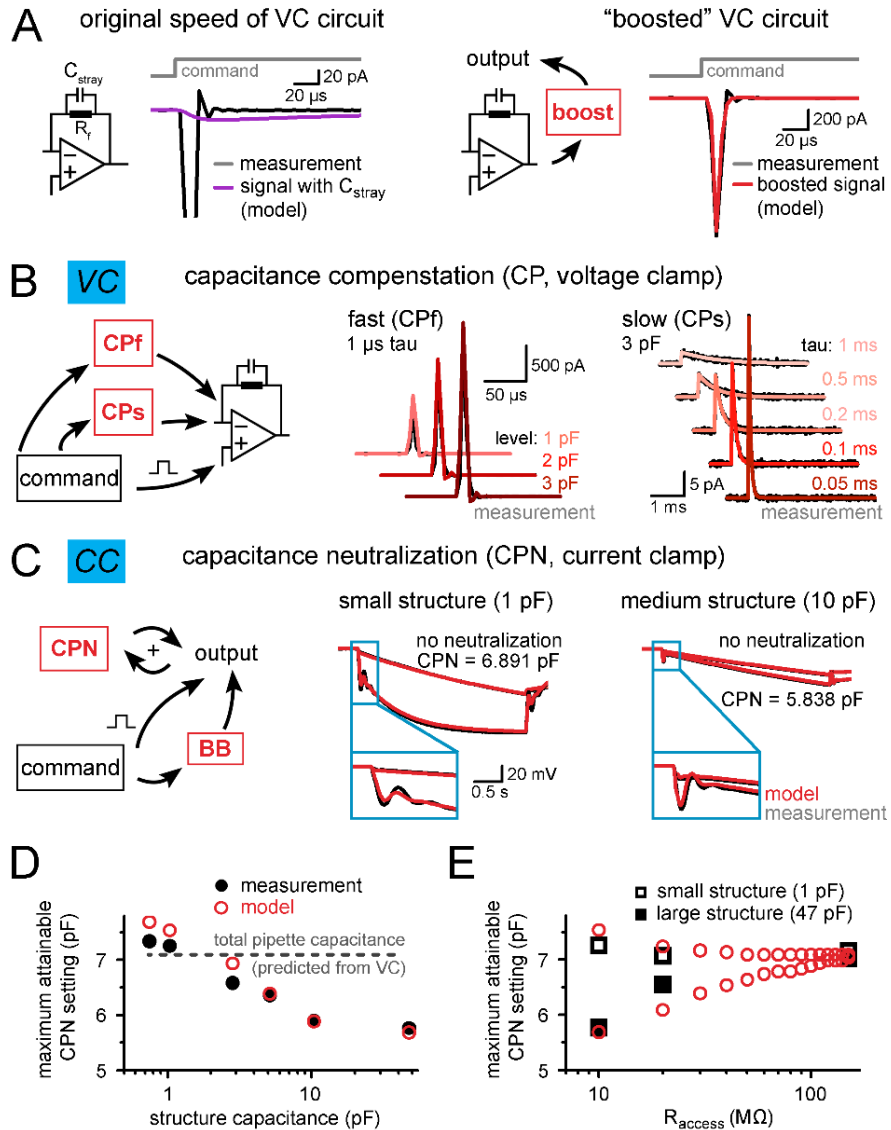


**Figure 29.** Model implementation of extracted amplifier features

A. Slower temporal profile of current responses in VC model (purple trace, left panel) by the stray capacitance ( $C_{\text{stray}}$ ) of the feedback resistor ( $R_f$ ) compared to measurements (black traces). Restoration of real amplifier speed by the implemented high frequency boost circuit (red trace, right panel). B. Capacitance compensation in the VC model (red) faithfully replicates the magnitude and the time course of amplifier-generated real signals (black) for both the fast (CPf) and slow (CPs) compensatory controls. C. Model replicates the amplifier's neutralizing capabilities and associated signal artefacts in CC mode. Comparison of simulated voltage responses (red) with the recorded signals (black) in response to brief (-100 pA, 2 ms) current injection measured by simulating either a small structure (middle panel) or a larger structure (left panel) during the test. D. Relationship between  $\text{CPN}_{\text{max}}$

and the size of the recorded structure in the test. The dashed line marks the instrumental capacitance determined in VC mode. Experimental observations are labeled with black circles; the red circles denote the model behavior under identical conditions. E. Experimentally determined  $CPN_{\max}$  (black squares) and  $CPN_{\max}$  in the model (red circles) as a function of  $R_{\text{access}}$  determined for small structure recordings (open squares) and for measurements where the structure is larger (closed squares).

resistance. Therefore, we next extended the CC model with a BB unit that subtracts the scaled version of the command from the measured voltage (Figure 28B).

### **4.3.2 Pipette implementation considers the observed nonuniform $C_{\text{pip}}$ and $R_{\text{pip}}$ distributions**

Implementation of a realistic patch pipette in the model requires information about the exact distribution of  $C_{\text{pip}}$  and  $R_{\text{pip}}$  along the pipette. To characterize the actual resistance distribution along the high impedance recording electrodes we subsequently broke pieces from the tip of the pipettes and measured the resistance of the remaining part (Figure 30A,  $n = 55$  resistance measurement from  $n = 46$  pipettes, only data points with more than  $20 \mu\text{m}$  tip distance are included). In line with the theoretical considerations (Benndorf, 1995), we found that pipette resistance drops sharply after the tip, falling below one  $M\Omega$  within the first millimeter ( $14.55 \pm 5.14 M\Omega$  pipette resistance below  $100 \mu\text{m}$  tip distances and  $0.33 \pm 0.18 M\Omega$  pipette resistance above 1 mm).

Pipette capacitance is primarily determined by the ratio of outer and inner diameters ( $R_{\text{OI}}$ ) of the pipette and it is less dependent on the absolute pipette dimensions (Benndorf, 1995). To determine the distribution of pipette capacitance for our electrodes, we systematically varied the immersed length of the pipette to the recording solution and measured the capacitance of the dipped part. The pipette capacitance increased sharply within the first 3 mm from the tip whereas the remaining part of the electrode had only moderate contribution to the total capacitance suggesting inhomogeneity in the capacitance distribution ( $0.03 \pm 0.07 \text{ pF}$ ,  $2.52 \pm 0.3 \text{ pF}$  and  $3.1 \pm 0.25 \text{ pF}$  at  $100 \mu\text{m}$ , 3 mm and 7 mm tip distances respectively, Figure 30A,  $n = 656$  capacitance measurement from  $n = 40$  pipettes). A potential explanation of the inhomogeneity is that  $R_{\text{OI}}$  ratio is not constant along the pipette and it

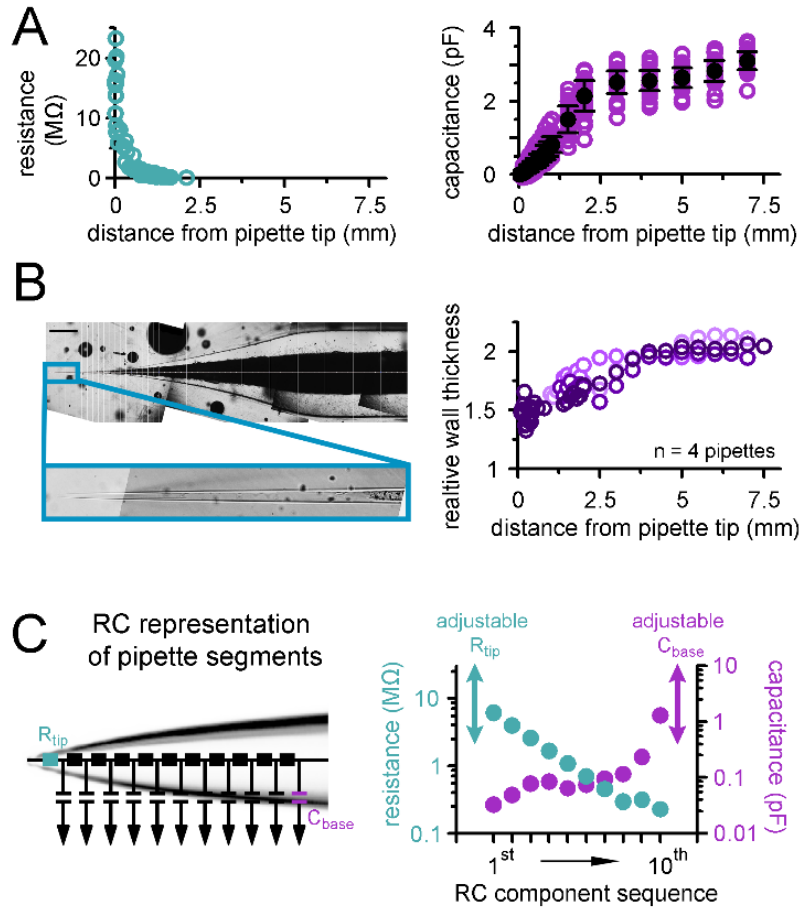


**Figure 30.** Pipette implementation considers the observed nonuniform  $C_{pip}$  and  $R_{pip}$  distributions

A. Pooled data of the pipette resistance (left graph, measured from 46 pipettes) and capacitance (right graph, data from 40 pipettes) as a function of tip distance. B. Representative images that were used for determine the ratio of the inner and the outer diameter of the high impedance pipettes. Scale bar=0.5 mm. Graph on the right shows the  $R_{oi}$  as a function of tip distance (measured from 4 pipettes, individual pipettes were indicated by different shades of purple). C. Schematic representation of the pipette model. Electrode was implemented as 10 RC units where each unit represents a particular part of the pipette. Graph on the right indicates the actual capacitance (purple) and resistance (green) values of the corresponding RC motifs. The double-headed arrows indicate the positions of the additional resistor ( $R_{tip}$ , on the left) and the capacitor ( $C_{base}$ , on the right) that serve to set the actual  $R_{pip}$  and  $C_{pip}$ , respectively.

decreases toward the tip. To test this possibility, we developed an independent measure where we directly measured the  $R_{OI}$  along the pipettes (Figure 30B, see Methods section for details). In line with our hypothesis,  $R_{OI}$  decreased at the tapered part of the pipette ( $R_{oi}<2\text{mm} = 1.6 \pm 0.02$  vs.  $R_{oi}>5\text{mm} = 2.04 \pm 0.02$ ,  $n = 4$  pipettes) predicting larger contribution of the tip

region to the total electrode capacitance. Based on these distributions, we generated the skeleton of an ideal high impedance pipette model, which included 10 RC units in series (Figure 30C). Model pipette parameters can be adjusted to account for the variability across individual pipettes using an additional resistor placed to the tip (to set the actual  $R_{\text{pip}}$ ) and a capacitor placed to the back end of the chain (to set actual  $C_{\text{pip}}$ ).

### 4.3.3 Reconstitution of the undisturbed membrane dynamics of a recorded axon

To demonstrate the capability of the model for predicting the undisturbed fast neuronal membrane responses, we choose an experiment in which APs were recorded directly from a small bouton of an identified hippocampal MF axon. The gMFBs of these axons are readily accessible for direct electrophysiological recordings (Geiger et al., 2000; Szabadics et al., 2009; Vyleta et al., 2014), however, MFs also have several regular sized axon terminals. Synaptic contacts formed by these small terminals on local INs represent a substantial part of the MF output (Acsady et al., 1998), therefore understanding of the MF function cannot be complete without the exploration of the electrical behavior of those structures. However, direct patch-clamp recordings made from the tiny axonal MF structures suffer from the technical limitations discussed in previous sections. Therefore, our computational approach can be particularly useful for the investigation of their artefact-free excitability.

We first characterized the actual pipette used in the experiment. The open tip resistance was directly measured in the bath (58.47 M $\Omega$ ). The  $C_{\text{pip}}$  can be estimated from the capacitive transients in cell attached (on-cell) VC measurements, i.e., when the electrode is already attached to the structure but the cell membrane has not been broken yet (Figure 31B). The target trace for this estimation was recorded using both fast and slow pipette capacitance compensation of the amplifier and we set the model accordingly (CP magnitude = 6.638 pF, tau = 1.17  $\mu$ s / CPs magnitude = 3 pF, tau = 88.2  $\mu$ s). The fitting procedure yielded a total fast capacitance of 7.097 pF for the recording electrode.



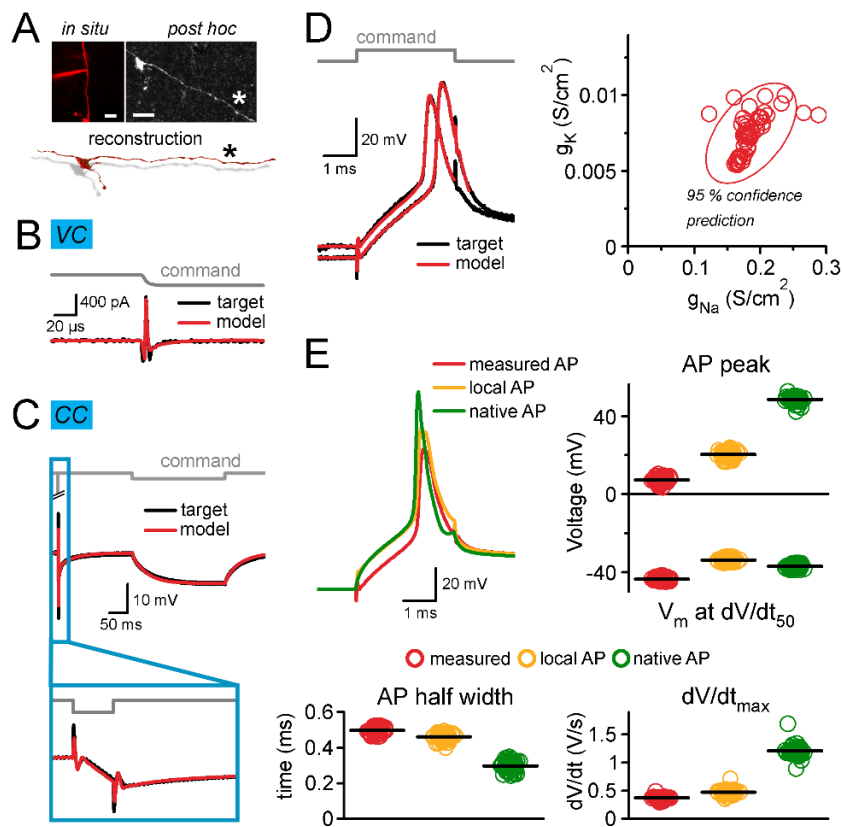


**Figure 31.** *Reconstitution of the undisturbed membrane dynamics of a recorded axon*

A. Confocal z-stack images on the top show the recorded axonal part taken at the end of the experiment (left) and after the anatomical recovery (right). Part of the reconstructed morphology is shown on the bottom. Asterisks mark the recording position. Scale bars = 10  $\mu\text{m}$ . B. On-cell recorded current response (black) upon  $-20\text{ mV}$  voltage step used for the  $C_{\text{pip}}$  adjustment in the model

(red). C. Recorded axonal voltage response (black) to short (3 ms,  $-50\text{ pA}$ ) and long (250 ms,  $-2.5\text{ pA}$ ) current stimuli. Passive parameters ( $R_m$ ,  $C_m$  and  $R_i$ ) and the  $R_{\text{access}}$  were fitted to the registered voltage response in the model for identical current step injections (red).

(D) Two simulated model APs (red) superimposed with their targets (black) evoked by brief (3 ms,  $75\text{ pA}$ ) current stimuli (left panel). The distribution of the best-fit maximal  $\text{Na}^+$  and  $\text{K}^+$  conductance densities used for AP reconstitution is on the right, red ellipse marks the 95 % confidence interval of the results.

(E) Representative simulated AP recorded through the pipette (red) together with the corresponding local axonal spike in the axon (orange) and with the undisturbed AP (i.e. simulated in the absence of the measuring system, green). Summary graphs show the observed differences in the AP parameters. Top, right: AP peak voltage and threshold (defined as the membrane voltage where the speed of the AP exceeds  $50\text{ mV/ms}$ ,  $V_m$  at  $dV/dt_{50}$ ); bottom, left: AP half width; bottom, right: maximal rate of the rising phase. Horizontal black lines on the plots indicate the mean values.

Morphological characteristics of the axon can substantially affect the signal generation and AP propagation (Goldstein et al., 1974; Manor et al., 1991). MFs form a single unmyelinated axon without ramifications in the stratum lucidum of the CA3 area, however, due to the highly variable size of the different bouton types ( $0.5\text{-}1\text{-}5\text{ }\mu\text{m}$  for small varicosities and  $2\text{-}8\text{ }\mu\text{m}$  for large terminals for gMFs) accurate modelling requires detailed

morphological information about the recorded axon (Acsady et al., 1998; Rollenhagen et al., 2007). Therefore, we recovered the axon after the measurements and created a detailed structural reconstruction (Figure 31A). Then, we fitted the model responses to the measured CC data to estimate the cable properties, namely the  $C_m$ , the  $R_m$  and the  $R_{ax}$  of the axon (Figure 31C). The well-established way to collect experimental data for this purpose is the combined application of short and long current steps in CC mode (Nörenberg et al., 2010; Roth et al., 2001; Schmidt-Hieber et al., 2007; Szoboszlay et al., 2016). A major disadvantage of this protocol is that evoked responses are strongly affected by the instrumentation, which can be only partly compensated even by careful BB and CPN setting. However, incorporation of the complete experimental instrumentation to the model allowed us to obtain relevant information about the cellular parameters even if the measuring artefacts severely affect the recorded signal. Our model could accurately replicate the recorded signal (together with the artefacts associated with the current injection) with passive parameters in the theoretically expected ranges:  $R_m = 55.3 \text{ k}\Omega \cdot \text{cm}^2$ , a  $C_m = 0.67 \text{ }\mu\text{F} \cdot \text{cm}^{-2}$  and  $R_{ax} = 150.2 \text{ }\Omega \cdot \text{cm}$ . In addition, the best approximation of the experimental data was (fit error: 2.86-times baseline signal variance) obtained when  $R_{access}$  closely matched the  $R_{pip}$  (the additional fine-tuning pipette resistance was  $2.84 \cdot 10^{-5} \text{ M}\Omega$ ) indicating that the electrode impedance was the sole determinant of  $R_{access}$  in that particular measurement.

After the incorporation of the basic membrane parameters into the model, we concentrated on the AP-shaping sodium and potassium conductances. We equipped the passive structural skeleton with active sodium and potassium conductance models to capture the spiking behavior of the axon. For this, we selected standard Hodgkin-Huxley type models (HH, the built-in mechanism in the NEURON) in which we could freely adjust the density, kinetics and the voltage dependence during the AP reconstitution process (Figure 31D and Figure 32). We elicited several APs during the experiment using brief current stimuli (3 ms, 75 pA) and we used them to define the parameter ensemble, which adequately (fit errors =  $6.86 \pm 1.13$  baseline variance,  $n = 49$ ) reproduces the firing of the axon within the model (using sodium and potassium conductance densities of  $0.186 \pm 0.004 \text{ S/cm}^2$  and  $0.0075 \pm 0.005 \text{ S/cm}^2$  respectively; Figure 31D).

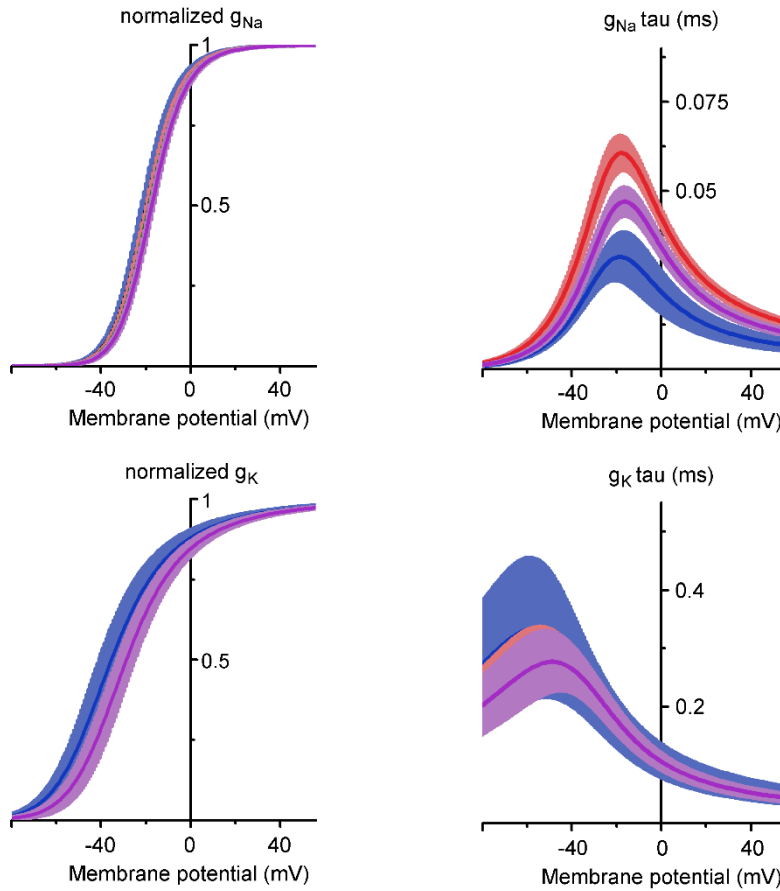


**Figure 32.** Kinetics and voltage-dependence of the model conductance sets used for the reconstruction of the APs measured with different recording conditions.

On the top, averaged voltage dependence and kinetic profile of the  $\text{Na}^+$  conductance models used for the reconstruction of the APs recorded with different CPN settings (CPN = 6.5 pF in purple, CPN = 7 pF in red and CPN = 7.386 pF in blue). On the bottom, same as in panel A but for the  $\text{K}^+$  conductance model.

By comparing the local and recorded axonal AP waveforms, we could directly quantify the filtering effect caused by the pipette. As expected, local spikes had larger peak amplitudes than the recorded APs ( $20.25 \pm 0.23$  mV vs  $7.26 \pm 0.24$  mV, respectively,  $p = 1.42 \cdot 10^{-84}$ ,  $t(48) = -369.61$  paired sample  $t$ -test,  $n = 49$  APs), but the difference in their half width was less pronounced (half width:  $0.46 \pm 0.003$  ms vs  $0.5 \pm 0.002$  ms,  $p = 2.78 \cdot 10^{-28}$ ,  $t(48) = 23.87$ , paired sample  $t$ -test,  $n = 49$  APs). These observations are in agreement with the expected filtering, which affects faster signals, such as axonal APs more prominently.

The BB compensation was set to 185 M $\Omega$  during the actual recording. However, the model predicted that the actual  $R_{\text{access}}$  was only 58.47 M $\Omega$ . Such overcompensation could heavily contaminate both the measured peak and the threshold voltages. Indeed, compared to the absolute peak potential, the filtering effect was much smaller on the spike amplitude (difference between the peak and threshold voltages,  $54.16 \pm 0.35$  vs  $50.76 \pm 0.34$  mV for local vs recorded AP amplitude respectively,  $p = 2.88 * 10^{-55}$ ,  $t(48) = -90.39$ , *paired sample t-test*,  $n = 49$  APs). We also analyzed the maximal rate of rise ( $dV/dt_{\text{max}}$ ) during the upstroke of the spikes, which should be particularly sensitive to the low-pass filtering introduced by the pipette. Our analysis revealed a significant difference between the rate of local and measured APs ( $476.7 \pm 6.4$  V/s vs  $373.24 \pm 3.5$  V/s, respectively,  $p = 6.99 * 10^{-35}$ ,  $t(48) = -33.39$ , *paired sample t-test*,  $n = 49$  APs). Altogether, the comparison of the recorded and local spikes revealed only moderate pipette filtering.

Our model predicts that the peak of the presynaptic AP in the small MF bouton had lower peak and slower kinetics than the APs measured directly from the gMFBs (Alle et al., 2009; Geiger et al., 2000). This observed difference could be either due to the biological variability among the subcellular compartments or due to the larger instrumental impact on the local membrane of the small axon. To discriminate between these possibilities, we investigated the native AP parameters predicted by the model. By comparing the local native spikes (i.e. elicited by an ideal current source without passive elements, by which filtering and passive pipette contribution is eliminated) to the local APs evoked through the pipette, we could examine the isolated instrumental distortion caused by the presence of the measuring system. We found that native APs had more depolarized peak potential ( $48.5 \pm 0.24$  mV,  $p = 2.99 * 10^{-81}$ ,  $t(48) = -315.13$ , *paired sample t-test*,  $n = 49$  APs) and had significantly faster kinetics (half width:  $0.297 \pm 0.004$  ms,  $p = 1.61 * 10^{-52}$ ,  $t(48) = 79.14$ , *paired sample t-test*;  $dV/dt_{\text{max}}$ :  $1207.5 \pm 13.8$  V/s,  $p = 3.58 * 10^{-56}$ ,  $t(48) = -94.4$ , *paired sample t-test*,  $n = 49$  APs) compared to the local spikes modelled with the experimental rig. The obtained native AP parameters were close to the AP kinetics observed in the direct gMFB measurements, which supports the hypothesis that the different AP shape observed in the small MF recording is primarily attributable to the presence of the measuring system.

#### 4.3.4 Distinct APs recorded from the same axon under different conditions predict similar native spike shapes

Simulation of the complete experimental situation has another potential advantage compared to more simplified instrumental representations. Namely, the predictions regarding the cellular parameters should be largely independent from the experimental conditions. To test the robustness of the model, we recorded the spike waveforms from the same axon with different CPN settings. We either reduced the applied neutralization by 0.5 pF (from 7 pF to 6.5 pF) or increased it close to  $CPN_{max}$  (to 7.386 pF). As a result of the manipulation, we recorded strikingly different APs from the same structure (Figure 33A, absolute AP peak:  $-2.46 \pm 0.16$  mV and AP half width:  $0.647 \pm 0.004$  ms,  $n = 25$  APs with CPN = 6.5 pF; AP peak:  $23.58 \pm 0.1$  mV and AP half width:  $0.41 \pm 0.004$  ms,  $n = 48$  APs with CPN = 7.386 pF). We independently repeated the previous optimizations with the experimentally used CPN settings in the model, and found that the model predicted highly overlapping parameter distributions for the different spike waveforms (Figure 33B). Specifically, the predicted amount of  $g_{Na}$  and  $g_K$  was similar (sodium conductance density:  $0.19 \pm 0.008$  S/cm<sup>2</sup>,  $0.18 \pm 0.003$  S/cm<sup>2</sup>,  $0.17 \pm 0.003$  S/cm<sup>2</sup>, potassium conductance density:  $0.007 \pm 0.0002$  S/cm<sup>2</sup>,  $0.007 \pm 0.0002$  S/cm<sup>2</sup>,  $0.007 \pm 0.0003$  S/cm<sup>2</sup>;  $n = 25$ ,  $n = 49$  and  $n = 48$  for CPN = 6.5 pF, CPN = 7 pF and CPN = 7.386 pF respectively, for kinetics and voltage-dependence see Figure 32) in spite of the original recorded AP traces were substantially different due to different CPN. We also repeated our simulations regarding the shape of the local APs with the obtained parameter sets (Figures 33A and C). In accordance with the moderate extent of low-pass filtering by the pipette, local AP shapes in the presence of the instrumentation were close to the recorded ones. In contrast, the distortion caused by the measuring instrumentation became progressively larger with the decreased CPN compensation (Figure 33C). Most importantly, the predicted native AP shape was similar irrespective of the experimentally used compensation, indicating that representation of the measuring system in the model is adequate to predict the correct native APs independent from the exact instrumentation settings (half-width of the native APs were  $0.29 \pm 0.006$  ms,  $0.297 \pm 0.004$  ms and  $0.33 \pm 0.005$  ms for CPN = 6.5 pF, CPN = 7 pF and CPN = 7.386 pF respectively).

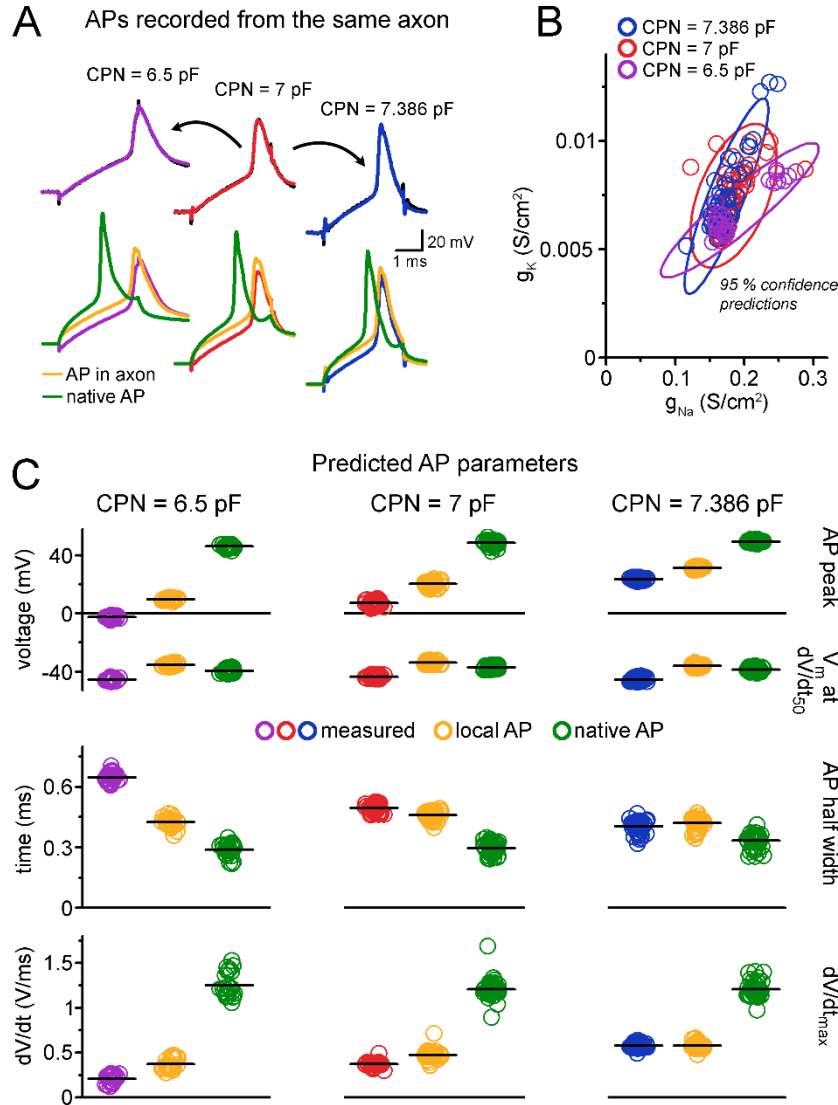


**Figure 33.** APs recorded from the same axon under different conditions predict similar native spike shapes

A. Representative target APs (black) and their best-fit model representations simulated with standard CPN settings (red, CPN = 7pF), with reduced neutralization (purple, CPN = 6.5 pF) or with the highest attainable CPN level (blue, CPN = 7.386 pF). The corresponding local spikes (orange) and native APs (green) are shown below. B. The best-fit maximal Na<sup>+</sup> and K<sup>+</sup> conductance densities for the reconstitution of the distinct AP waveforms. Color coding is as for A. C. Summary graphs show the differences in the AP parameters. Horizontal black lines on the plots indicate the mean values. Top: AP peak voltage and threshold; middle: AP half width; bottom: maximal rate of the rising phase.

#### 4.3.5 Instrumental and structural parameters cooperatively define signal distortion in recordings from small neuronal structures

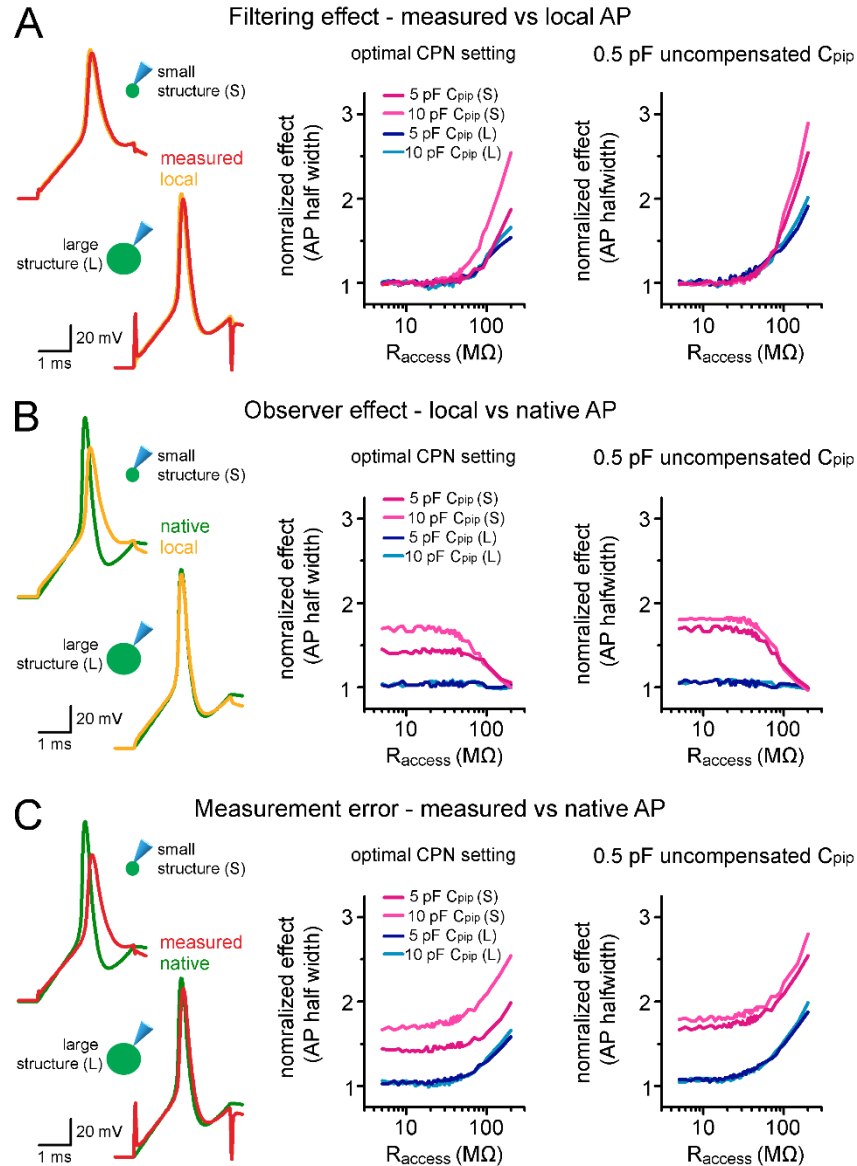


**Figure 34.** Instrumental and structural parameters jointly define signal distortion in recordings from small neuronal structures

A. On the left, representative traces show the filtering effect of 50 M $\Omega$   $R_{access}$  (ie. the difference between the measured and the local APs). Graph in the middle summarizes the filtering over a wide range of  $R_{access}$ . The effect size was quantified as the difference in AP half width. The right graph summarizes the effect in other simulations where suboptimal CPN was modelled. Purple lines show filtering effect in small structures (1 pF), blue lines show the same for large structures (10 pF). B. Same as in A but for the observer effect, quantified as the difference between the local AP and the native AP waveform. C. Same as in (A) but for the measurement error, quantified as the difference between the local AP and the native AP waveform.

Our modelling results described above highlighted that complete elimination of the

instrumental disturbance during the actual recording was not possible under the conditions used in that particular experiment (difference in measured vs native AP in Figure 33C). Importantly, the alterations in the AP shape predominantly arose from the inadequate local signal generation rather than from the pipette filtering. Thus, the reduced membrane responsiveness caused by the presence of the pipette (hereafter referred as observer effect based on the analogy with the concept introduced in the field of physics for the situations where the measurement inevitably changes the measured parameter) seems to be a critical factor which defines the accuracy of the measured voltage responses.

To evaluate the relative contribution of the pipette filtering and the observer effect to the instrumental distortions under different experimental conditions, we varied the pipette parameters and the cellular capacitance in the model (Figure 34). Consistent with the previous findings, the pipette filtering allows the faithful measurement of the fast voltage transients in wide ranges of  $R_{\text{access}}$  (Figure 34A) with optimal CPN neutralization. However, the filtering effect increases sharply at higher  $R_{\text{access}}$  as the cutoff frequency of the RC filter formed by the pipette becomes progressively lower and reaches the temporal domain of the APs. When the target structure is large ( $C_{\text{cell}} = 10 \text{ pF}$ ), the filtering becomes the sole error source that defines the measurement error because the capacitance added by the pipette becomes insignificant compared to the  $C_{\text{cell}}$ . In contrast, when the recorded structure is small ( $C_{\text{cell}} = 1 \text{ pF}$ ), the observer effect causes significant inaccuracy in the measurement especially when the  $R_{\text{access}}$  is low (Figure 34B). Increasing the  $R_{\text{access}}$ , however, effectively isolates the residual instrumental capacitance from the cell and weakens the observer effect. As a result of the complementary changes in the two effects, quality of the small axonal recordings - which are heavily distorted by the observer effect - is less sensitive to the  $R_{\text{access}}$  compared to the recordings from larger neuronal structures (Figure 34C). Furthermore, the measurement error was independent of the pipette capacitance when larger target structure was modelled. In contrast, smaller  $C_{\text{pip}}$  effectively reduced both error types, thus it improved the quality of the recorded signal in simulations where the target structure was small. We also tested how the level of the applied CPN affects the quality of the measurement. For this, we repeated the simulations with reduced CPN level ( $-0.5 \text{ pF}$ ), which scaled the extent of both errors without affecting their  $R_{\text{access}}$  dependence (Figure 34).



Altogether, our results revealed target-size-dependent instrumental contribution to the measured voltage signals. In case of small neuronal structures, the quality of the measurement critically depends on the observer effect, which partially decouples the measurement error from the access resistance but increases the sensitivity to the pipette capacitance.

## 5. Discussion

The main findings of my PhD thesis are as follows: (1) The wiring of feed-forward inhibition between individual GCs and PCs is independent of the direct excitation. (2) Different expression of the auxiliary subunits of Kv4.3 potassium channel underlies a novel functional heterogeneity of CCK+INs in the rat hippocampus due to frequency-dependent modulation of the excitability of individual cells. (3) Distortion and filtering of voltage signals from small neuronal structures can be estimated and corrected for by the precise modelling of the recording instruments.

### 5.1 Global thresholding of CA3 activity through FFI

Feedforward inhibition (FFI) between the dentate gyrus (DG) and CA3 sparsifies and shapes memory- and spatial navigation-related activities. To better understand FFI wiring schemes, we compared the prevalence of diIPSCs between pairs of individually recorded GC axons or somas and PCs, some of which were connected by monosynaptic excitation, while others were not. We found single GC-elicited diIPSCs with similar probabilities irrespective of the presence of monosynaptic excitation. This observation suggests that the wiring of FFI between individual GCs and PCs is independent of the direct excitation.

Our findings reveal that individual MFs recruit CA3 PCs and FFINs regardless of the presence of inhibitory synaptic connections between them. Therefore, FFI between the DG and the CA3 is not wired to specifically inhibit a restricted population of PCs selected based on direct excitation from the GCs. This is consistent with the idea that the FFI is randomly distributed by individual GCs, which allows for the adjustment of general excitability of the CA3 network based on the activity of the DG.

Importantly, FFI is effective in preventing spike transmission during sparse GC firing, while high-frequency GC bursts remain effective (Acsady et al., 2007; Henze et al., 2002; Zucca et al., 2017). This is because the large number of synaptic release sites (Rollenhagen et al., 2007) and activity-dependent facilitation of release (Salin et al., 1996; Toth et al., 2000) provide an almost unlimited source of excitation from each giant MF bouton onto the PCs. However, this is restricted to only a few PCs because each GC typically

innervates 10–20 PCs (Acsady et al., 1998). Thus, the sparse excitation of the PCs is accompanied by highly divergent and random FFI from the same GC input source. Specifically, the targets of the FFI originating from single GCs are multiplied via two divergent steps. First, GCs innervate 4–5 times more INs than PCs (Acsady et al., 1998). These FF-INs then usually innervate hundreds of PCs (Bezaire et al., 2013). The dynamically adjusted global threshold for PC recruitment by the local, MF-driven GABAergic inhibition, thus, potentially contributes to the disambiguation of small differences in the physiological DG activity, such as single AP- or burst-firing. Nevertheless, certain small ensembles consisting of PCs inhibited to a smaller degree may become relatively more sensitive to forthcoming presynaptic GC activity than the majority of the population. The randomness of the FFI wiring implies not only that the FFI sets the activation threshold for the majority of the PCs, but also that it contributes, to some extent, to the precise tuning of spike timing in dually innervated PCs (Pouille et al., 2001).

Some of our observations suggest that the various types of FF-INs follow the random wiring rules in a similar manner. Most importantly, the kinetic properties of the diIPSCs are similar in PCs that received direct monosynaptic excitation from the recorded MF and in PCs that were devoid of direct excitation. Given the anatomical and synaptic diversities of the FF-INs, which result in cell type-specific kinetics for their IPSCs, if some FF-IN types were preferentially recruited for specific FFI or for lateral inhibition (i.e., if they are more or less likely to be recruited onto the directly MF innervated PCs), the properties of the diIPSC responses were expected to differ in PCs with and without direct MF input. In contrast to these assumptions, we found no difference in the diIPSCs between the two groups of PCs. Further support for the homogeneous FF-IN type contribution is provided by the observation that the occurrences of the diIPSC events were similar during the low- and high-frequency stimulus trains in the two PC groups. This observation supports the similar recruitment of the various FF-IN types onto both PC groups because different IPSC occurrences were expected to reflect the cell type-specific short-term plasticity of the excitation of the FF-INs (Mori et al., 2004; Szabadics et al., 2009; Torborg et al., 2010; Toth et al., 2000).

The detected diIPSCs represent only a fraction of the available actual FFI. The observed diIPSCs are those that involve the most strongly excited and single MF-activated FF-INs under the less excitable slice conditions (Jiang et al., 2015). Thus, the obtained

diIPSC connectivity underestimates the total number of inhibited PCs by the single GC-driven FFI under *in vivo* conditions. Thus, most likely, only a small population of PCs is devoid of FFI from single GCs, as there are relatively large numbers of GABAergic cells that are innervated by single MFs and large numbers of PCs that are innervated by all types of FF-INs (Acsady et al., 1998). Importantly, in spite of the underestimation of the overall FFI in our experimental arrangement, observation of diIPSCs in PCs both with and without direct excitation is consistent with random FFI innervation rules. First, merely the presence of the diIPSCs shows that none of the two PC groups is completely avoided by FFI. Second, because the recorded GC/MF-PC pairs were randomly chosen, the preservation of the connection onto and from the intermediate INs and the reliable activation of some of them cannot be preferentially influenced by the preparation conditions. Thus, it is reasonable to conclude that the FFI of PCs was independent of their direct excitation from the individually tested GC source within the intact circuit. The random local wiring of FFI is crucial to understand the functional contexts of the plasticity mechanisms that regulate the DG/ CA3 interface, including the experience-dependent structural plasticity (De Paola et al., 2003; Ruediger et al., 2011; Tashiro et al., 2003), short-term dynamics (Szabadics et al., 2009; Torborg et al., 2010; Toth et al., 2000) and activity-dependent balance (Mori et al., 2004) of the recruitment of inhibition (Acsady et al., 2007). Notably, the numbers of innervated FF-INs, particularly PV-expressing cells, are markedly altered in response to environmental enrichment and experience (Ruediger et al., 2011). Thus, considering our findings that FFI does not have to be maintained in a selected population of PCs, the learning-induced structural plasticity of the FFI circuit might not require energy-costly mechanisms to maintain its proper functions (this would have been necessary if each PV-positive cell selected certain structurally or functionally defined groups of PCs). However, the randomness excludes the possibility that the FFI and its structural plasticity are required for the suppression or enhancement of specific information channels. Rather, the FFI sets the overall excitability of the network depending on the state, demands, and previous activity of the DG and CA3 networks. Future studies should also address whether the random wiring rule is preserved or compromised during disease states, such as epilepsy. If this rule persists in spite of insults, therapies that enhance FFI between the DG and CA3 circuits may not be useful tools for combating abnormal GC activity. These strong activities are unlikely to be

restrained by the FFI. Similarly strong, but normal GC activities, such as bursts, constitute physiological DG functions (Diamantaki et al., 2016; Pernía-Andrade et al., 2014), and they are able to overcome the randomly distributed FFI, as evidenced by the ability of single GCs to drive postsynaptic PC firing (Henze et al., 2002). Thus, abnormal strong activities can also overcome the FFI if the capacity for facilitating excitation is maintained.

The functional consequence of random FFI wiring is that FF-INs provide a “blanket of inhibition” (Karnani et al., 2014) for the CA3 by dynamically adjusting the activity level for a large population of PCs (Ferrante et al., 2009; Pouille et al., 2001), from which the “detonating” (Vyleta et al., 2016) direct excitation can select the required ensemble of cells. This arrangement therefore provides optimal signal-to-noise communication between the DG and the CA3 at the lowest wiring and developmental cost while maintaining diverse plasticity opportunities (Buzsáki et al., 2004; Lawrence et al., 2004). Our results also suggest that individual GCs have access to various types of FF-INs follow the random wiring rules in a similar manner, as the kinetic properties of the diIPSCs are similar in both groups of PCs. FF-INs in the CA3 consist of biophysically and morphologically complementary inhibitory cell types that are specifically tuned for regulating the activity of the much more populous PCs in broad temporal (Lasztóczy et al., 2011; Viney et al., 2013) and spatial domains (Tamas F Freund et al., 1996). However, due to the computational demand of physiological behavior on the hippocampus, the currently known degree of functional diversity of GABAergic cells is most likely insufficient. The basis of this theorised limitation is the severe computational constraint of a system, which consist of various “rigid building blocks”. PCs have been recently shown to overcome this challenge by exhibiting anatomical and functional diversity within the classically defined cell type (Hunt et al., 2018; Kesner, 2007), which raises the question, whether functional heterogeneity exists within specific GABAergic cell types to the same extent. Therefore, our next aim was to investigate whether GABAergic diversity exists beyond the established cell classes, which can multiply the available regulating possibilities.

## 5.2 Molecular mechanisms of GABAergic diversity with CA3 CCK+INs

We found that CCK+INs in the rat hippocampal CA3 region exhibit a previously undetected functional heterogeneity, which enables members of this IN population to modulate their output in a MP-dependent manner. This phenomenon is a consequence of different transient potassium currents, mediated by Kv4.3 potassium channels coupled to distinct auxiliary subunits. Although our recordings confirmed the crucial role of this potassium channel in TOR firing, RS cells also express Kv4.3 channels, and in fact, their density is higher in RS cells compared to TOR cells. Thus, paradoxically, in spite of Kv4.3 mediated currents are responsible for the unique and distinctive firing properties of TOR cells, Kv4.3 currents are present in both cell firing types. We found the potential explanation that solves this paradox in differences of the auxiliary subunits that can modify the function of Kv4.3 channels. Namely, the K<sup>+</sup> channel-interacting proteins (KChIPs) and dipeptidyl peptidase-like proteins (DPLPs), which form ternary complexes with the pore-forming Kv4 subunits (Henry Hungtao Jerng et al., 2014; Pongs et al., 2010; Zhou et al., 2015). It has been shown that when expressed alone in heterologous cells, Kv4 subunits are poorly transported to the cell surface (Hasdemir et al., 2005). However co-expression with KChIP or DPPL promotes the trafficking and surface expression of Kv4 (Foeger et al., 2012; Shibata et al., 2003) without affecting the voltage dependence of the potassium conductances (Henry H Jerng et al., 2004; Nadal et al., 2003; Shibata et al., 2003). Importantly, our results show that TOR firing is dependent on the left-ward shifted voltage dependence of the Kv4.3 mediated currents, which can be a consequence of co-expression of Kv4, KChIP, and DPPL, which complex can fully constitute the characteristic properties of subthreshold A-type potassium currents (Henry H Jerng et al., 2005; Henry H Jerng et al., 2012; Nadal et al., 2003). In contrast to the function of these “classical” auxiliary subunits, several KChIP variants and isoforms have been described with opposing effects on Kv4 channels (see below), which results in diverse modulatory possibilities.

KChIP1 is strongly expressed by RS cells, whereas most TOR cells lacked this cytosolic auxiliary subunit. The known effects of the KChIP1 (Beck et al., 2002; M. Bourdeau et al., 2011; Henry Hungtao Jerng et al., 2014; Pongs et al., 2010) correlate well with the properties of the I<sub>SA</sub> in RS cells. As a classical KChIP, KChIP1 increases surface

expression of Kv4 channel complex. Indeed, we measured larger density of  $I_{SA}$  current in outside out patch from RS cells than in TOR cells. We also observed that Kv4.3 immunosignal was usually stronger in RS cells than in TOR cells. Furthermore, we were able to reproduce TOR and RS firing phenotypes in the realistically simulated conditions only if the total amount of  $I_{SA}$  conductance was larger in RS cells than in TOR cells. The apparent paradox between larger current density and the smaller measured current amplitude near the AP threshold in RS cells derives from the differences in the voltage dependence of activation of  $I_{SA}$  in RS and TOR cells.  $I_{SA}$  channels are submaximally activated at physiological subthreshold voltage. However, because of the left-shifted activation curve, a much larger fraction of  $I_{SA}$  channels are activated in TOR cells at lower voltage ranges. Therefore, larger currents can be generated even by a smaller number of channels. Another substantial influence of KChIP1 on Kv4.3 is the acceleration of steady-state inactivation kinetics and the recovery time from inactivation (Beck et al., 2002; M. Bourdeau et al., 2011; Henry Hungtao Jerng et al., 2014; Pongs et al., 2010). These are also correlated well with the differences of  $I_{SA}$  in RS and TOR cells, as both parameters were much faster in the former type of cells.

KChIP4 was the dominant KChIP in TOR cells and it was not detected in most RS cells. Our data also showed that TOR cells expressed a special splicing isoform, KChIP4e, which belongs to the so-called tmKChIPs (Holmqvist et al., 2002; Henry H Jerng et al., 2008; Henry Hungtao Jerng et al., 2014; Pongs et al., 2010). In contrast to classical KChIPs, all tmKChIPs including KChIP4e do not facilitate surface expression of Kv4 channels (Holmqvist et al., 2002; Henry H Jerng et al., 2008; Pruunsild et al., 2012). As explained above, several lines of evidence suggest lower Kv4.3 channel density in the KChIP4e-expressing TOR compared to KChIP1-expressing RS cells. The presence of tmKChIPs results in slow inactivation kinetics, often slower than that of the solitary Kv4 channels (Holmqvist et al., 2002; Henry H Jerng et al., 2007; Henry H Jerng et al., 2008; Tang et al., 2014). As a consequence of enhanced closed-state inactivation of Kv4.3 channels, KChIP4e causes a leftward shift in the voltage dependence of inactivation (Tang et al., 2013; Tang et al., 2014). Albeit it is a likely possibility due to the similarity of their N-terminal domains, it remains to be answered whether the effects of KChIP4e on Kv4.3 kinetics are similar to the other studied tmKChIPs. The slower inactivation and recovery of  $I_{SA}$  in KChIP4e-expressing

TOR cells were critical for their unique functionality during 8-15 Hz network states because they define the availability of the  $I_{SA}$  conductance. KChIP4 was present only in three RS cells and two of them expressed the KChIP4b isoform, which is a classical KChIP that, similarly to KChIP1s results in much faster inactivation and recovery (Henry H Jerng et al., 2008). We should also note that the apparent discrepancy in KChIP4 detection between the mRNA and protein levels may also be explained by the presence of different isoforms, as our antibody may have targeted the highly variable N-terminal region.

Both DPLPs were present in TOR and RS cells. DPP10c isoform, which is known to affect voltage dependence of Kv4 channels, but does not accelerate inactivation (Henry H Jerng et al., 2007), was ubiquitous in both types of CCK+INs. Albeit all tested CCK+INs had a significant amount of DPP6 mRNA, TOR and RS cells expressed different isoforms. RS cells expressed only DPP6L and in TOR cells the primary isoform was DPP6S (but DPP6L was also present in several cells). DPP6S can contribute to the left-shifted voltage dependence of activation of  $I_{SA}$  in TOR cells. The left-shifted voltage dependence is important for the sufficient prevention of spiking. The dual set of DPP6 proteins fits well with our observations that many properties of TOR cells can be described only if two populations of Kv4.3-mediated currents are present. Altogether, these observations suggest that apparently small modifications in the available components of ion channel complexes underlie the different functions of TOR and RS cells.

The net effects of KChIPs and DPLPS are not simply the sum of the effects of individual subunits. Some subunits either dominate others or the interaction can result in unique combinations of effects (Henry H Jerng et al., 2005; Nadal et al., 2006; Zhou et al., 2015). For example, when DPP6K is present, KChIP4e causes a leftward shift of the voltage dependence of inactivation and deceleration of the recovery from inactivation compared to other KChIPs (Henry H Jerng et al., 2012). In this regard, it is an important observation for our results that DPP6S, unlike some other DPLPs, cannot overcome the tmKChIP4-mediated deceleration of inactivation (Henry H Jerng et al., 2007; Henry H Jerng et al., 2008; Seikel et al., 2009). Thus, the expression of DPP6S in TOR cells may preserve the unique modulatory effects of KChIP4e. Because of the composition of these ternary channel complexes by multiple proteins and splicing variants, whose interactions are not yet



characterized, the exact contribution of individual components of DPP6S/L/DPP10c-KChIP4e-Kv4.3- and DPP6L/DPP10c-KChIP1-Kv4.3-complexes cannot be predicted yet. Nevertheless, the higher channel density, faster inactivation kinetics and faster recovery from inactivation of  $I_{SA}$  in RS compared to TOR cells are consistent with the differential expression of KChIP1 and KChIP4e, and the cell type-specific expression and contributions of DPP10c, DPP6L and DPP6S are expected to explain unique voltage-dependency in the two types of CCK+INs without the involvement of additional differences between RS and TOR cells.

Our modeling results demonstrated that the functional consequence of the altered excitability of individual CCK+INs causes different contributions of individual cells to certain network oscillations, specifically in the theta frequency (6-12 Hz) range. Hippocampal theta rhythm is thought to link different cells together in functional ensembles that support memory operations by providing integrated representations of complex concepts and experiences (Colgin, 2016; Feng et al., 2015; Gupta et al., 2012; Wikenheiser et al., 2015). Furthermore, each theta cycle may represent a fundamental unit of information within an episodic memory, as experimental results have shown that distinct representations of different environment (Jezek et al., 2011), or of the same environment but with changed reward position (Dupret et al., 2013), were mainly segregated across separate theta cycles. Although inhibitory transmitter release from CCK+INs allows efficient inhibition of CA3 PCs (Szabó et al., 2014) and thereby the precise control of theta-linked functional ensembles, the significant amount of transmitter released asynchronously from CCK+INs suggests that these cells are capable of prolonged inhibition over several theta cycles. Furthermore, CCK+INs fire at specific phases of the theta cycle, closely following the discharge of CA3 PCs, indicating their main role in feedback regulation (Lasztóczy et al., 2011). These results predict that the CCK+INs have an important role in the dampening of excitability for a large population of PCs. This idea gains support from a recent publication, which showed that disruption of normal CCK+IN connectivity causes reduction of hippocampal oscillations specifically at the theta-band (del Pino et al., 2017), which is consistent with the *in vivo* firing preference of CCK+INs during theta range oscillations (Klausberger et al., 2005) and the fact that a specialized population of highly rhythmic septal IN population (the so-called “Teevra-cells”, (Joshi et al., 2017)) selectively innervate CCK+INs in the hippocampus. Reduction of

hippocampal theta is generally thought to cause network dysfunctions, which was confirmed by in vivo imaging showing impaired spatial representations, delayed acquisition of spatial reference and deficits in hippocampal spatial organization (del Pino et al., 2017). Therefore, the question arises; what could be the role of a cellular phenomenon which selectively silences a population of CCK+INs during theta? Although several fundamental studies showed that the magnitude of theta in the rodent hippocampus is predictive for the learning and recall capability of the animal (Berry et al., 1978; Landfield et al., 1973; Winson, 1978), leading to the early recognition of the fundamental role of theta oscillation in learning and memory, these studies have only looked at the behavior of the animal in familiar environments and recall of learned patterns. Unexpected environmental novelty however has a different effect on hippocampal theta. The hippocampal formation has long been linked with novelty detection, especially where experience differs from expectation given the experimental context or other stimuli (a.k.a., “contextual” or “relational” novelty, “associative mismatch” or “comparator” processing, see e.g., (Hasselmo et al., 1996; Honey et al., 1998; Köhler et al., 2005; Kumaran et al., 2006; Lisman et al., 2001; Sokolov, 1963; Strange et al., 1999; Vinogradova, 2001; Wan et al., 1999)), consistent with its role in context-dependent episodic/declarative memory (Cohen et al., 1993; O'keefe et al., 1978; Zola-Morgan et al., 1991). It has been shown that environmental novelty produces a sharp reduction in the prevalence of theta frequency in foraging rats and this reduction is greater for an unexpected environment than for a completely novel one (Jeewajee et al., 2008). Importantly, this theta-reduction slowly disappears with increasing familiarity. Taken together, reduced prevalence of theta frequency can have important physiological functions in memory formation, which suggests an important function for a subset of CCK+INs (TOR cells), which can selectively lower their firing in this oscillatory regime.

### **5.3 Overcoming the limitations of voltage recordings from small neuronal structures**

In a measurement-based computational work, we developed a realistic model representation of the measuring instrument that replicates an actual patch clamp recording when combined with the detailed morphological reconstruction of the recorded structure. Our results provide evidence that simulating the complete experimental condition is suitable to

correct for the instrumental distortion present in the direct electrophysiological recordings from fine neuronal processes. The model also enabled us to evaluate the extent and the source of the voltage perturbations in direct measurements from these submicron cellular structures. The signal deterioration in small axonal recordings primarily arise from the altered local signal generation instead of pipette filtering, therefore we conclude that the relationship between the measuring instrument and the physical parameters of the recorded structure defines the error in small axonal recordings.

We used the model to correct for the instrumental distortion on the AP shape recorded from a regular sized ( $<1 \mu\text{m}$ ) bouton of the MF. We constructed a population of models that adequately represent the spiking behavior of the axon (Figure 31D). Despite the considerable difference among the individual estimated conductance parameters, the predicted local and native APs were always similar emphasizing the robustness of our model predictions. The estimated high active conductance densities suggest robust local AP phenotype. Indeed, the unperturbed axonal APs were brief events with large amplitude (Figure 31D) whose shape closely resembled to the spike waveform reported for the gMFBs of the same axon (Alle et al., 2009; Geiger et al., 2000). Taken together, the model was able to predict the basic spiking properties of a small axonal structure, however, it has to be noted that for the investigation of specific firing behaviors, such as frequency dependent changes in the shape of APs, a much more complete model is needed that takes into account additional parameters and ionic mechanisms.

Here we claim that the accuracy of CC experiments is the product of the instrumental and cellular parameters. First, our data indicate that compensatory capabilities of the amplifier vary substantially depending on the size of the recorded structure and on the  $R_{\text{access}}$  (Figure 29). Interestingly, those factors were found to be also critical for the signal alterations measured in feedback amplifiers despite their operation follows different principles (Magistretti et al., 1998). Second, the main source of the voltage distortion in small axonal recordings is the observer effect, where the residual instrumental capacitance interferes with the local spike generation (Figure 34). Third, the leak formed by the seal interferes with the local conductance leading to significant depolarization and  $R_{\text{input}}$  reduction in small neuronal processes (Perkins, 2006). Importantly, the target-size-dependent effects are not specific to

the axonal recordings; all measurements targeting small cellular compartments whose electrical parameters are comparable to the capacitance and leak introduced by the measuring instrument are potentially subject to the above-mentioned distortions.

We used the model specifically to assess the native axonal voltage signals and to explore the voltage distortions in axonal measurements. However, it is easy to adopt the model for other experimental situations where the instrumental contribution to the recorded signal is significant (e.g. in vivo recordings or dendritic measurements (Davie et al., 2006; Margrie et al., 2002)). The approach introduced here provides in-depth insights how the instrumental parameters interact with the measured electrical signals, which can guide the design and optimization of future experiments.

## 6. CONCLUSIONS

The main conclusions of my doctoral dissertation are the following:

- Feed-forward inhibition is randomly wired from individual dentate gyrus granule cells onto CA3 PCs
- Half of the CCK+INs in the CA3 region show state-dependent firing (TOR cells) and this novel type of heterogeneity do not correlate with previously known anatomical subpopulations of CCK+INs.
- Differences in low-voltage-activated potassium currents ( $I_{SA}$ ) underlie state-dependent firing of TOR cells
- Realistic models of reconstructed CCK+INs with different  $I_{SA}$  suggest that TOR cells are selectively silenced by their low-voltage-activated potassium currents in a narrow range of oscillatory states
- Kv4 channels are responsible for both types of  $I_{SA}$  in CCK+INs
- Kv4 channels are differentially modulated in the two subpopulation of CCK+INs by specific isoforms of their auxiliary subunits.
- Reconstitution of undisturbed axonal membrane dynamics from voltage recordings can be achieved using *in silico* implementation of the patch-clamp amplifier and the detailed reconstruction of the target structure.

## 7. SUMMARY

Information processing capabilities of a neuronal circuit are largely determined by the diversity of available circuit components and the wiring rules governing their connections. Therefore, accurate description of the local connectivity and examination of the functional heterogeneity of distinct cell types is crucial for understanding the role of the circuit itself. The first two studies presented in my thesis aimed to examine the diversity of the dentate gyrus – CA3 interface at cellular and connectivity levels. In the third project, we investigated the constraints of the recording technique used in these studies, the patch-clamp method.

In the first part of my dissertation, we examined the connectivity of the feed-forward inhibitory circuit in the dentate gyrus – CA3 interface. We found that feed-forward inhibition is random from individual granule cells, as single granule cell-elicited disynaptic inhibitory events were found in CA3 PCs with the same probabilities, irrespective of the presence of monosynaptic excitation. The results suggest that this circuit arrangement is ideal for signal sparsification by setting the general excitability of the CA3 depending on the overall activity of granule cells.

Next, we investigated the functional heterogeneity of inhibitory cells in the CA3 region, and found that half of the CCK-expressing cells (CCK+IN) show MP dependent firing properties, which is caused by surprisingly few differences in the expression of specific splicing isoforms of the auxiliary subunits of Kv4.3 potassium channels. Furthermore, these differences lead to different contributions of individual CCK+INs to specific network oscillations.

At the final part of my thesis, we explored the reliability of patch clamp recordings in current clamp mode when recordings are made from small subcellular compartments. We found that the recording pipette not only filters the recorded signal, but directly perturbs the local electrical environment as well. Furthermore, our model system was able to retrieve the native behavior of the recorded structure by precisely incorporating the detailed morphology, the recording pipette and the amplifier circuits as well.

## 8. ÖSSZEFOGLALÁS

Az idegi hálózatok képességét nagyban befolyásolja az azt felépítő komponensek száma és azok összeköttetési sémája. Ahhoz tehát, hogy feltérképezhessük egy hálózat funkcióját, fontos megismernünk hogy a résztvevő sejtípusok milyen funkcionális sokszínűséggel bírnak, továbbá hogy a hálózat “kapcsolási rajza” milyen szabályok szerint szerveződik. A tézisem első két részében ezeket a kérdéseket vizsgáltuk meg a gírusz dentátusz – CA3 kapcsolati hálózatában. Végezetül a tézisem harmadik részében a patch clamp mérési technika limitációit vizsgáltuk.

Az elsőként bemutatott munkában megvizsgáltuk a gírusz dentátuszból a CA3 régióba érkező előrecsatoló gátlás kapcsolati sémáját. Az eredményeink azt mutatták, a két régió közötti információ átadást limitáló gátlás huzalozása random. Az egyedi szemcsesejtek vagy szemcsesejt axonok stimulálásának hatására ugyanolyan arányban találtunk kiváltott gátló eseményeket az adott szemcsesejthez közvetlenül serkentett és nem kapcsolt CA3 piramissejtekben is. Ezek az eredmények azt sugallják, hogy ennek a régiónak a kapcsolati sémája kiválóan alkalmas a továbbított jelek szűrésére a CA3 régió általános serkenthetőségének modulálása által, a gírusz dentátusz aktivitásának függvényében.

Az értekezésem következő részében a CA3 régió gátló sejtjeinek funkcionális heterogenitását vizsgáltam. Az eredményeink azt mutatták, hogy a CCK expresszáló sejtek közel fele membránpotenciál-függő tüzelési mintázattal rendelkeznek. Megmutattuk továbbá, hogy ezt az aktivitási mintázatot a Kv4.3-as kálium ioncsatorna járulékos alegységeinek alternatív hasítási izoformái okozzák. Ezek az izoforma külsőségek azonban fontos funkcionális jelentőséggel bírnak, mivel az eltérő aktivitás mintázat különböző hálózatbeli szerepet eredményez különböző oszcillációk alatt.

Az értekezésem utolsó részében azt vizsgáltuk, hogy mennyire megbízhatóak a current clamp elvezetések kis struktúrák mérése során. Az eredményeink azt mutatták, hogy a méréshez használt pipetta nem csupán szűri a mért jelet, hanem közvetlenül befolyásolja a mért struktúra passzív elektromos környezetét is. Azonban a munkánk során sikerült egy olyan modellt létrehozunk, amely képes az eredeti jel visszanyerésére a pipetta és elvezetett struktúra figyelembevételével.

## 9. REFERENCES

- Acsady L, & Kali S. (2007) Models, structure, function: the transformation of cortical signals in the dentate gyrus. *Prog. Brain Res.*, 163: 577-599.
- Acsady L, Kamondi A, Sik A, Freund T, & Buzsáki G. (1998) GABAergic cells are the major postsynaptic targets of mossy fibers in the rat hippocampus. *J. Neurosci.*, 18: 3386-3403.
- Albus JS. (1971) A theory of cerebellar function. *Math. Biosci.*, 10: 25-61.
- Alle H, & Geiger JR. (2006) Combined analog and action potential coding in hippocampal mossy fibers. *Science*, 311: 1290-1293.
- Alle H, Roth A, & Geiger JR. (2009) Energy-efficient action potentials in hippocampal mossy fibers. *Science*, 325: 1405-1408.
- Amaral DG, & Witter MP. (1989) The three-dimensional organization of the hippocampal formation: a review of anatomical data. *Neuroscience*, 31: 571-591.
- Amoroso EC, Baxter MI, Chiquoine A, & Nisbet R. (1964) The fine structure of neurons and other elements in the nervous system of the giant African land snail *Archachatina marginata*. *Proceedings of the Royal Society of London. Series B. Biological Sciences*, 160: 167-180.
- Ascoli GA, Alonso-Nanclares L, Anderson SA, Barrionuevo G, Benavides-Piccione R, Burkhalter A, Buzsáki G, Cauli B, DeFelipe J, & Fairén A. (2008) Petilla terminology: nomenclature of features of GABAergic interneurons of the cerebral cortex. *Nature Reviews Neuroscience*, 9: 557.
- Ball M. (1977) Neuronal loss, neurofibrillary tangles and granulovacuolar degeneration in the hippocampus with ageing and dementia. *Acta Neuropathol.*, 37: 111-118.
- Bartos M, Vida I, Frotscher M, Meyer A, Monyer H, Geiger JR, & Jonas P. (2002) Fast synaptic inhibition promotes synchronized gamma oscillations in hippocampal



- interneuron networks. *Proceedings of the National Academy of Sciences*, 99: 13222-13227.
- Bartos M, Vida I, & Jonas P. (2007) Synaptic mechanisms of synchronized gamma oscillations in inhibitory interneuron networks. *Nature reviews neuroscience*, 8: 45.
- Beck EJ, Bowlby M, An WF, Rhodes KJ, & Covarrubias M. (2002) Remodelling inactivation gating of Kv4 channels by KChIP1, a small-molecular-weight calcium-binding protein. *The Journal of physiology*, 538: 691-706.
- Benndorf K. (1995). Low-noise recording. In *Single-Channel Recording* (pp. 129-145): Springer.
- Berry SD, & Thompson RF. (1978) Prediction of learning rate from the hippocampal electroencephalogram. *Science*, 200: 1298-1300.
- Bezair MJ, Raikov I, Burk K, Vyas D, & Soltesz I. (2016) Interneuronal mechanisms of hippocampal theta oscillations in a full-scale model of the rodent CA1 circuit. *Elife*, 5: e18566.
- Bezair MJ, & Soltesz I. (2013) Quantitative assessment of CA1 local circuits: knowledge base for interneuron-pyramidal cell connectivity. *Hippocampus*, 23: 751-785.
- Bilkey D, & Goddard G. (1987) Septohippocampal and commissural pathways antagonistically control inhibitory interneurons in the dentate gyrus. *Brain Res.*, 405: 320-325.
- Bourdeau M, Laplante I, Laurent C, & Lacaille J-C. (2011) KChIP1 modulation of Kv4. 3-mediated A-type K<sup>+</sup> currents and repetitive firing in hippocampal interneurons. *Neuroscience*, 176: 173-187.
- Bourdeau ML, Morin F, Laurent CE, Azzi M, & Lacaille J-C. (2007) Kv4. 3-mediated A-type K<sup>+</sup> currents underlie rhythmic activity in hippocampal interneurons. *J. Neurosci.*, 27: 1942-1953.
- Branco T, & Häusser M. (2010) The single dendritic branch as a fundamental functional unit in the nervous system. *Curr. Opin. Neurobiol.*, 20: 494-502.

- Brette R, Piwkowska Z, Monier C, Rudolph-Lilith M, Fournier J, Levy M, Frégnac Y, Bal T, & Destexhe A. (2008) High-resolution intracellular recordings using a real-time computational model of the electrode. *Neuron*, 59: 379-391.
- Brown TH, & Johnston D. (1983) Voltage-clamp analysis of mossy fiber synaptic input to hippocampal neurons. *J. Neurophysiol.*, 50: 487-507.
- Bucurenciu I, Kulik A, Schwaller B, Frotscher M, & Jonas P. (2008) Nanodomain coupling between Ca<sup>2+</sup> channels and Ca<sup>2+</sup> sensors promotes fast and efficient transmitter release at a cortical GABAergic synapse. *Neuron*, 57: 536-545.
- Buhl EH, Halasy K, & Somogyi P. (1994) Diverse sources of hippocampal unitary inhibitory postsynaptic potentials and the number of synaptic release sites. *Nature*, 368: 823.
- Buzsáki G, & Czeh G. (1981) Commissural and perforant path interactions in the rat hippocampus. *Exp. Brain Res.*, 43: 429-438.
- Buzsáki G, Geisler C, Henze DA, & Wang X-J. (2004) Interneuron diversity series: circuit complexity and axon wiring economy of cortical interneurons. *Trends Neurosci.*, 27: 186-193.
- Cajal RY. (1893) *Nuevo concepto de la histología de los centros nerviosos.*
- Cea-del Rio CA, Lawrence JJ, Erdelyi F, Szabo G, & McBain CJ. (2011) Cholinergic modulation amplifies the intrinsic oscillatory properties of CA1 hippocampal cholecystokinin-positive interneurons. *The Journal of physiology*, 589: 609-627.
- Cembrowski MS, & Spruston N. (2019) Heterogeneity within classical cell types is the rule: lessons from hippocampal pyramidal neurons. *Nature Reviews Neuroscience*, 20: 193-204.
- Clelland C, Choi M, Romberg C, Clemenson GD, Fagniere A, Tyers P, Jessberger S, Saksida L, Barker R, & Gage F. (2009) A functional role for adult hippocampal neurogenesis in spatial pattern separation. *Science*, 325: 210-213.
- Close J, Xu H, García NDM, Batista-Brito R, Rossignol E, Rudy B, & Fishell G. (2012) *Satb1* is an activity-modulated transcription factor required for the terminal

- differentiation and connectivity of medial ganglionic eminence-derived cortical interneurons. *J. Neurosci.*, 32: 17690-17705.
- Cobb S, Buhl E, Halasy K, Paulsen O, & Somogyi P. (1995) Synchronization of neuronal activity in hippocampus by individual GABAergic interneurons. *Nature*, 378: 75.
- Cohen N, & Eichenbaum H. (1993) *Memory, amnesia, and hippocampal function*. Cambridge: MIT Press.
- Colombo, PJ, Davis, HP, & Volpe, BT (1989). Allocentric spatial and tactile memory impairments in rats with dorsal caudate lesions are affected by preoperative behavioral training. *Behavioral Neuroscience*, 103: 1242-1250.
- Cole KS, & Curtis HJ. (1939) Electric impedance of the squid giant axon during activity. *The Journal of general physiology*, 22: 649-670.
- Cole KS, & Moore JW. (1960) Potassium ion current in the squid giant axon: dynamic characteristic. *Biophys. J.*, 1: 1-14.
- Colgin LL. (2016) Rhythms of the hippocampal network. *Nature Reviews Neuroscience*, 17: 239.
- Cope D, Maccaferri G, Marton L, Roberts J, Cobden P, & Somogyi P. (2002) Cholecystokinin-immunopositive basket and Schaffer collateral-associated interneurons target different domains of pyramidal cells in the CA1 area of the rat hippocampus. *Neuroscience*, 109: 63-80.
- Danielson NB, Turi GF, Ladow M, Chavlis S, Petrantonakis PC, Poirazi P, & Losonczy A. (2017) In vivo imaging of dentate gyrus mossy cells in behaving mice. *Neuron*, 93: 552-559. e554.
- Danielson NB, Zaremba JD, Kaifosh P, Bowler J, Ladow M, & Losonczy A. (2016) Sublayer-specific coding dynamics during spatial navigation and learning in hippocampal area CA1. *Neuron*, 91: 652-665.
- Davie JT, Kole MH, Letzkus JJ, Rancz EA, Spruston N, Stuart GJ, & Häusser M. (2006) Dendritic patch-clamp recording. *Nat. Protoc.*, 1: 1235.

- De Paola V, Arber S, & Caroni P. (2003) AMPA receptors regulate dynamic equilibrium of presynaptic terminals in mature hippocampal networks. *Nat. Neurosci.*, 6: 491.
- DeFelipe J, Hendry S, & Jones E. (1986) A correlative electron microscopic study of basket cells and large GABAergic neurons in the monkey sensory-motor cortex. *Neuroscience*, 17: 991-1009.
- del Pino I, Brotons-Mas JR, Marques-Smith A, Marighetto A, Frick A, Marín O, & Rico B. (2017) Abnormal wiring of CCK+ basket cells disrupts spatial information coding. *Nat. Neurosci.*, 20: 784.
- DeSimone CV, Zarayskiy VV, Bondarenko VE, & Morales MJ. (2011) Heteropoda toxin 2 interaction with Kv4. 3 and Kv4. 1 reveals differences in gating modification. *Mol. Pharmacol.*, 80: 345-355.
- Diamantaki M, Frey M, Berens P, Preston-Ferrer P, & Burgalossi A. (2016) Sparse activity of identified dentate granule cells during spatial exploration. *Elife*, 5: e20252.
- Dobrunz LE, & Stevens CF. (1997) Heterogeneity of release probability, facilitation, and depletion at central synapses. *Neuron*, 18: 995-1008.
- Dupret D, O'Neill J, & Csicsvari J. (2013) Dynamic reconfiguration of hippocampal interneuron circuits during spatial learning. *Neuron*, 78: 166-180.
- Efron B. (1979) Bootstrap methods: another look at the jackknife *Annals of statistics* 7: 1–26. [View Article PubMed/NCBI Google Scholar.](#)
- Eggermann E, & Jonas P. (2012) How the 'slow' Ca<sup>2+</sup> buffer parvalbumin affects transmitter release in nanodomain-coupling regimes. *Nat. Neurosci.*, 15: 20.
- Espinoza C, Guzman SJ, Zhang X, & Jonas P. (2018) Parvalbumin+ interneurons obey unique connectivity rules and establish a powerful lateral-inhibition microcircuit in dentate gyrus. *Nature communications*, 9: 4605.
- Evstratova A, Chamberland S, & Topolnik L. (2011) Cell type-specific and activity-dependent dynamics of action potential-evoked Ca<sup>2+</sup> signals in dendrites of hippocampal inhibitory interneurons. *The Journal of physiology*, 589: 1957-1977.

- Fabre LF, McLendon DM, & Stephens AG. (1981) Comparison of the therapeutic effect, tolerance and safety of ketazolam and diazepam administered for six months to outpatients with chronic anxiety neurosis. *J. Int. Med. Res.*, 9: 191-198.
- Farrant M, & Nusser Z. (2005) Variations on an inhibitory theme: phasic and tonic activation of GABA A receptors. *Nature Reviews Neuroscience*, 6: 215.
- Feng T, Silva D, & Foster DJ. (2015) Dissociation between the experience-dependent development of hippocampal theta sequences and single-trial phase precession. *J. Neurosci.*, 35: 4890-4902.
- Férezou I, Cauli B, Hill EL, Rossier J, Hamel E, & Lambolez B. (2002) 5-HT<sub>3</sub> receptors mediate serotonergic fast synaptic excitation of neocortical vasoactive intestinal peptide/cholecystokinin interneurons. *J. Neurosci.*, 22: 7389-7397.
- Ferrante M, Migliore M, & Ascoli GA. (2009) Feed-forward inhibition as a buffer of the neuronal input-output relation. *Proceedings of the National Academy of Sciences*, 106: 18004-18009.
- File SE, Kenny PJ, & Cheeta S. (2000) The role of the dorsal hippocampal serotonergic and cholinergic systems in the modulation of anxiety. *Pharmacol. Biochem. Behav.*, 66: 65-72.
- Foeger NC, Norris AJ, Wren LM, & Nerbonne JM. (2012) Augmentation of Kv4.2-encoded currents by accessory dipeptidyl peptidase 6 and 10 subunits reflects selective cell surface Kv4.2 protein stabilization. *J. Biol. Chem.*, 287: 9640-9650.
- Földy C, Darmanis S, Aoto J, Malenka RC, Quake SR, & Südhof TC. (2016) Single-cell RNAseq reveals cell adhesion molecule profiles in electrophysiologically defined neurons. *Proceedings of the National Academy of Sciences*, 113: E5222-E5231.
- Freund TF. (2003) Interneuron diversity series: rhythm and mood in perisomatic inhibition. *Trends Neurosci.*, 26: 489-495.
- Freund TF, & Buzsáki G. (1996) Interneurons of the hippocampus. *Hippocampus*, 6: 347-470.

- Freund TF, & Katona I. (2007) Perisomatic inhibition. *Neuron*, 56: 33-42.
- Geiger JR, & Jonas P. (2000) Dynamic control of presynaptic Ca<sup>2+</sup> inflow by fast-inactivating K<sup>+</sup> channels in hippocampal mossy fiber boutons. *Neuron*, 28: 927-939.
- Gentet LJ, Stuart GJ, & Clements JD. (2000) Direct measurement of specific membrane capacitance in neurons. *Biophys. J.*, 79: 314-320.
- Gigg J. (2006) Constraints on hippocampal processing imposed by the connectivity between CA1, subiculum and subicular targets. *Behav. Brain Res.*, 174: 265-271.
- Glickfeld LL, & Scanziani M. (2006) Distinct timing in the activity of cannabinoid-sensitive and cannabinoid-insensitive basket cells. *Nat. Neurosci.*, 9: 807.
- Goldstein SS, & Rall W. (1974) Changes of action potential shape and velocity for changing core conductor geometry. *Biophys. J.*, 14: 731-757.
- GoodSmith D, Chen X, Wang C, Kim SH, Song H, Burgalossi A, Christian KM, & Knierim JJ. (2017) Spatial representations of granule cells and mossy cells of the dentate gyrus. *Neuron*, 93: 677-690. e675.
- Goussakov IV, Fink K, Elger CE, & Beck H. (2000) Metaplasticity of mossy fiber synaptic transmission involves altered release probability. *J. Neurosci.*, 20: 3434-3441.
- Graves AR, Moore SJ, Bloss EB, Mensh BD, Kath WL, & Spruston N. (2012) Hippocampal pyramidal neurons comprise two distinct cell types that are countermodulated by metabotropic receptors. *Neuron*, 76: 776-789.
- Gulyás AI, Megias M, Emri Z, & Freund TF. (1999) Total number and ratio of excitatory and inhibitory synapses converging onto single interneurons of different types in the CA1 area of the rat hippocampus. *J. Neurosci.*, 19: 10082-10097.
- Gulyás AI, Milles R, Hájos N, & Freund TF. (1993) Precision and variability in postsynaptic target selection of inhibitory cells in the hippocampal CA3 region. *Eur. J. Neurosci.*, 5: 1729-1751.
- Gupta AS, Van Der Meer MA, Touretzky DS, & Redish AD. (2012) Segmentation of spatial experience by hippocampal theta sequences. *Nat. Neurosci.*, 15: 1032.

- Guzman SJ, Schlögl A, Espinoza C, Zhang X, Suter B, & Jonas P. (2019) Fast signaling and focal connectivity of PV+ interneurons ensure efficient pattern separation by lateral inhibition in a full-scale dentate gyrus network model. *bioRxiv*: 647800.
- Guzman SJ, Schlögl A, Frotscher M, & Jonas P. (2016) Synaptic mechanisms of pattern completion in the hippocampal CA3 network. *Science*, 353: 1117-1123.
- Hasdemir B, Fitzgerald DJ, Prior IA, Tepikin AV, & Burgoyne RD. (2005) Traffic of Kv4 K+ channels mediated by KCHIP1 is via a novel post-ER vesicular pathway. *The Journal of cell biology*, 171: 459-469.
- Hasselmo ME, Wyble BP, & Wallenstein GV. (1996) Encoding and retrieval of episodic memories: role of cholinergic and GABAergic modulation in the hippocampus. *Hippocampus*, 6: 693-708.
- Hefft S, & Jonas P. (2005) Asynchronous GABA release generates long-lasting inhibition at a hippocampal interneuron–principal neuron synapse. *Nat. Neurosci.*, 8: 1319.
- Hendry S, & Jones E. (1985) Morphology of synapses formed by cholecystokinin-immunoreactive axon terminals in regio superior of rat hippocampus. *Neuroscience*, 16: 57-68.
- Henze DA, Wittner L, & Buzsáki G. (2002) Single granule cells reliably discharge targets in the hippocampal CA3 network in vivo. *Nat. Neurosci.*, 5: 790.
- Hines ML, & Carnevale NT. (1997) The NEURON simulation environment. *Neural Comput.*, 9: 1179-1209.
- Hines ML, & Carnevale NT. (2001) NEURON: a tool for neuroscientists. *Neuroscientist*, 7: 123-135.
- Holmqvist MH, Cao J, Hernandez-Pineda R, Jacobson MD, Carroll KI, Sung MA, Betty M, Ge P, Gilbride KJ, & Brown ME. (2002) Elimination of fast inactivation in Kv4 A-type potassium channels by an auxiliary subunit domain. *Proceedings of the National Academy of Sciences*, 99: 1035-1040.

- Honey RC, Watt A, & Good M. (1998) Hippocampal lesions disrupt an associative mismatch process. *J. Neurosci.*, 18: 2226-2230.
- Hosp JA, Strüber M, Yanagawa Y, Obata K, Vida I, Jonas P, & Bartos M. (2014) Morphophysiological criteria divide dentate gyrus interneurons into classes. *Hippocampus*, 24: 189-203.
- Hunt DL, Linaro D, Si B, Romani S, & Spruston N. (2018) A novel pyramidal cell type promotes sharp-wave synchronization in the hippocampus. *Nat. Neurosci.*, 21: 985.
- Jayant K, Hirtz JJ, Jen-La Plante I, Tsai DM, De Boer WD, Semonche A, Peterka DS, Owen JS, Sahin O, & Shepard KL. (2017) Targeted intracellular voltage recordings from dendritic spines using quantum-dot-coated nanopipettes. *Nature nanotechnology*, 12: 335.
- Jeewajee A, Lever C, Burton S, O'Keefe J, & Burgess N. (2008) Environmental novelty is signaled by reduction of the hippocampal theta frequency. *Hippocampus*, 18: 340-348.
- Jerng HH, Kunjilwar K, & Pfaffinger PJ. (2005) Multiprotein assembly of Kv4. 2, KChIP3 and DPP10 produces ternary channel complexes with ISA-like properties. *The Journal of physiology*, 568: 767-788.
- Jerng HH, Lauver AD, & Pfaffinger PJ. (2007) DPP10 splice variants are localized in distinct neuronal populations and act to differentially regulate the inactivation properties of Kv4-based ion channels. *Mol. Cell. Neurosci.*, 35: 604-624.
- Jerng HH, & Pfaffinger PJ. (2008) Multiple Kv channel-interacting proteins contain an N-terminal transmembrane domain that regulates Kv4 channel trafficking and gating. *J. Biol. Chem.*, 283: 36046-36059.
- Jerng HH, & Pfaffinger PJ. (2012) Incorporation of DPP6a and DPP6K variants in ternary Kv4 channel complex reconstitutes properties of A-type K current in rat cerebellar granule cells. *PLoS One*, 7: e38205.



- Jerng HH, & Pfaffinger PJ. (2014) Modulatory mechanisms and multiple functions of somatodendritic A-type K<sup>+</sup> channel auxiliary subunits. *Front. Cell. Neurosci.*, 8: 82.
- Jerng HH, Qian Y, & Pfaffinger PJ. (2004) Modulation of Kv4.2 channel expression and gating by dipeptidyl peptidase 10 (DPP10). *Biophys. J.*, 87: 2380-2396.
- Jezek K, Henriksen EJ, Treves A, Moser EI, & Moser M-B. (2011) Theta-paced flickering between place-cell maps in the hippocampus. *Nature*, 478: 246.
- Jiang X, Shen S, Cadwell CR, Berens P, Sinz F, Ecker AS, Patel S, & Tolias AS. (2015) Principles of connectivity among morphologically defined cell types in adult neocortex. *Science*, 350: aac9462.
- Joshi A, Salib M, Viney TJ, Dupret D, & Somogyi P. (2017) Behavior-dependent activity and synaptic organization of septo-hippocampal GABAergic neurons selectively targeting the hippocampal CA3 area. *Neuron*, 96: 1342-1357. e1345.
- Jung M, & McNaughton B. (1993) Spatial selectivity of unit activity in the hippocampal granular layer. *Hippocampus*, 3: 165-182.
- Karnani MM, Agetsuma M, & Yuste R. (2014) A blanket of inhibition: functional inferences from dense inhibitory connectivity. *Curr. Opin. Neurobiol.*, 26: 96-102.
- Katona I, Sperl agh B, S ik A, K afalvi A, Vizi ES, Mackie K, & Freund TF. (1999) Presynaptically located CB1 cannabinoid receptors regulate GABA release from axon terminals of specific hippocampal interneurons. *J. Neurosci.*, 19: 4544-4558.
- Kepecs A, & Fishell G. (2014) Interneuron cell types are fit to function. *Nature*, 505: 318-326.
- Kesner RP. (2007) Behavioral functions of the CA3 subregion of the hippocampus. *Learn. Memory*, 14: 771-781.
- Klausberger T. (2009) GABAergic interneurons targeting dendrites of pyramidal cells in the CA1 area of the hippocampus. *Eur. J. Neurosci.*, 30: 947-957.

- Klausberger T, Magill PJ, Márton LF, Roberts JDB, Cobden PM, Buzsáki G, & Somogyi P. (2003) Brain-state-and cell-type-specific firing of hippocampal interneurons in vivo. *Nature*, 421: 844.
- Klausberger T, Marton LF, O'Neill J, Huck JH, Dalezios Y, Fuentealba P, Suen WY, Papp E, Kaneko T, & Watanabe M. (2005) Complementary roles of cholecystokinin-and parvalbumin-expressing GABAergic neurons in hippocampal network oscillations. *J. Neurosci.*, 25: 9782-9793.
- Klausberger T, & Somogyi P. (2008) Neuronal diversity and temporal dynamics: the unity of hippocampal circuit operations. *Science*, 321: 53-57.
- Knierim JJ, Neunuebel JP, & Deshmukh SS. (2014) Functional correlates of the lateral and medial entorhinal cortex: objects, path integration and local–global reference frames. *Philosophical Transactions of the Royal Society B: Biological Sciences*, 369: 20130369.
- Kohara K, Pignatelli M, Rivest AJ, Jung H-Y, Kitamura T, Suh J, Frank D, Kajikawa K, Mise N, & Obata Y. (2014) Cell type–specific genetic and optogenetic tools reveal hippocampal CA2 circuits. *Nat. Neurosci.*, 17: 269.
- Köhler S, Danckert S, Gati JS, & Menon RS. (2005) Novelty responses to relational and non-relational information in the hippocampus and the parahippocampal region: A comparison based on event-related fMRI. *Hippocampus*, 15: 763-774.
- Kollo M, Holderith NB, & Nusser Z. (2006) Novel subcellular distribution pattern of A-type K<sup>+</sup> channels on neuronal surface. *J. Neurosci.*, 26: 2684-2691.
- Kowalski J, Gan J, Jonas P, & Pernía-Andrade AJ. (2016) Intrinsic membrane properties determine hippocampal differential firing pattern in vivo in anesthetized rats. *Hippocampus*, 26: 668-682.
- Kumaran D, & Maguire EA. (2006) An unexpected sequence of events: mismatch detection in the human hippocampus. *PLoS Biol.*, 4: e424.

- Lammel S, Hetzel A, Häckel O, Jones I, Liss B, & Roeper J. (2008) Unique properties of mesoprefrontal neurons within a dual mesocorticolimbic dopamine system. *Neuron*, 57: 760-773.
- Landfield PW, Tusa RJ, & McGAUGH JL. (1973) Effects of posttrial hippocampal stimulation on memory storage and EEG activity. *Behav. Biol.*, 8: 485-505.
- Larkum ME, Nevian T, Sandler M, Polsky A, & Schiller J. (2009) Synaptic integration in tuft dendrites of layer 5 pyramidal neurons: a new unifying principle. *Science*, 325: 756-760.
- Lasztóczy B, Tukker JJ, Somogyi P, & Klausberger T. (2011) Terminal field and firing selectivity of cholecystinin-expressing interneurons in the hippocampal CA3 area. *J. Neurosci.*, 31: 18073-18093.
- Lawrence JJ, Grinspan ZM, & McBain CJ. (2004) Quantal transmission at mossy fibre targets in the CA3 region of the rat hippocampus. *The Journal of physiology*, 554: 175-193.
- Lawrence JJ, & McBain CJ. (2003) Interneuron diversity series: containing the detonation–feedforward inhibition in the CA3 hippocampus. *Trends Neurosci.*, 26: 631-640.
- Leão RN, Mikulovic S, Leão KE, Munguba H, Gezelius H, Enjin A, Patra K, Eriksson A, Loew LM, & Tort AB. (2012) OLM interneurons differentially modulate CA3 and entorhinal inputs to hippocampal CA1 neurons. *Nat. Neurosci.*, 15: 1524.
- Lee H, Wang C, Deshmukh SS, & Knierim JJ. (2015) Neural population evidence of functional heterogeneity along the CA3 transverse axis: pattern completion versus pattern separation. *Neuron*, 87: 1093-1105.
- Lee S-H, Földy C, & Soltesz I. (2010) Distinct endocannabinoid control of GABA release at perisomatic and dendritic synapses in the hippocampus. *J. Neurosci.*, 30: 7993-8000.
- Leutgeb S, & Leutgeb JK. (2007) Pattern separation, pattern completion, and new neuronal codes within a continuous CA3 map. *Learn. Memory*, 14: 745-757.

- Lien CC, Martina M, Schultz JH, Ehmke H, & Jonas P. (2002) Gating, modulation and subunit composition of voltage-gated K<sup>+</sup> channels in dendritic inhibitory interneurons of rat hippocampus. *The Journal of Physiology*, 538: 405-419.
- Lisman JE. (1997) Bursts as a unit of neural information: making unreliable synapses reliable. *Trends Neurosci.*, 20: 38-43.
- Lisman JE, & Otmakhova NA. (2001) Storage, recall, and novelty detection of sequences by the hippocampus: elaborating on the SOCRATIC model to account for normal and aberrant effects of dopamine. *Hippocampus*, 11: 551-568.
- Lorente de N6 R. (1934) Studies on the structure of the cerebral cortex. II. Continuation of the study of the ammonic system. *Journal für Psychologie und Neurologie*.
- Losonczy A, Bir6 6A, & Nusser Z. (2004) Persistently active cannabinoid receptors mute a subpopulation of hippocampal interneurons. *Proceedings of the National Academy of Sciences*, 101: 1362-1367.
- Lovett-Barron M, Kaifosh P, Kheirbek MA, Danielson N, Zaremba JD, Reardon TR, Turi GF, Hen R, Zemelman BV, & Losonczy A. (2014) Dendritic inhibition in the hippocampus supports fear learning. *Science*, 343: 857-863.
- Magistretti J, Mantegazza M, De Curtis M, & Wanke E. (1998) Modalities of distortion of physiological voltage signals by patch-clamp amplifiers: a modeling study. *Biophys. J.*, 74: 831-842.
- Major G, Larkum ME, & Schiller J. (2013) Active properties of neocortical pyramidal neuron dendrites. *Annu. Rev. Neurosci.*, 36: 1-24.
- Manor Y, Koch C, & Segev I. (1991) Effect of geometrical irregularities on propagation delay in axonal trees. *Biophys. J.*, 60: 1424-1437.
- Margrie TW, Brecht M, & Sakmann B. (2002) In vivo, low-resistance, whole-cell recordings from neurons in the anaesthetized and awake mammalian brain. *Pflügers Archiv*, 444: 491-498.

- Margrie TW, Sakmann B, & Urban NN. (2001) Action potential propagation in mitral cell lateral dendrites is decremental and controls recurrent and lateral inhibition in the mammalian olfactory bulb. *Proceedings of the National Academy of Sciences*, 98: 319-324.
- Marr D. (1969) A theory of cerebellar cortex. *The Journal of physiology*, 202: 437-470. doi:10.1113/jphysiol.1969.sp008820
- McHugh TJ, Jones MW, Quinn JJ, Balthasar N, Coppari R, Elmquist JK, Lowell BB, Fanselow MS, Wilson MA, & Tonegawa S. (2007) Dentate gyrus NMDA receptors mediate rapid pattern separation in the hippocampal network. *Science*, 317: 94-99.
- Miles R, Tóth K, Gulyás AI, Hájos N, & Freund TF. (1996) Differences between somatic and dendritic inhibition in the hippocampus. *Neuron*, 16: 815-823.
- Monyer H, & Markram H. (2004) Interneuron Diversity series: Molecular and genetic tools to study GABAergic interneuron diversity and function. *Trends Neurosci.*, 27: 90-97.
- Mori M, Abegg MH, Gähwiler BH, & Gerber U. (2004) A frequency-dependent switch from inhibition to excitation in a hippocampal unitary circuit. *Nature*, 431: 453.
- Mori M, Gähwiler BH, & Gerber U. (2007) Recruitment of an inhibitory hippocampal network after bursting in a single granule cell. *Proceedings of the National Academy of Sciences*, 104: 7640-7645.
- Nadal MS, Amarillo Y, de Miera EV-S, & Rudy B. (2006) Differential characterization of three alternative spliced isoforms of DPPX. *Brain Res.*, 1094: 1-12.
- Nadal MS, Ozaita A, Amarillo Y, de Miera EV-S, Ma Y, Mo W, Goldberg EM, Misumi Y, Ikehara Y, & Neubert TA. (2003) The CD26-related dipeptidyl aminopeptidase-like protein DPPX is a critical component of neuronal A-type K<sup>+</sup> channels. *Neuron*, 37: 449-461.
- Neher E, & Sakmann B. (1976) Single-channel currents recorded from membrane of denervated frog muscle fibres. *Nature*, 260: 799.

- Neu A, Földy C, & Soltesz I. (2007) Postsynaptic origin of CB1-dependent tonic inhibition of GABA release at cholecystokinin-positive basket cell to pyramidal cell synapses in the CA1 region of the rat hippocampus. *The Journal of physiology*, 578: 233-247.
- Neubrandt M, Oláh VJ, Brunner J, Marosi EL, Soltesz I, & Szabadics J. (2018) Single bursts of individual granule cells functionally rearrange feedforward inhibition. *J. Neurosci.*, 38: 1711-1724.
- Neuhoff H, Neu A, Liss B, & Roeper J. (2002) Ih channels contribute to the different functional properties of identified dopaminergic subpopulations in the midbrain. *J. Neurosci.*, 22: 1290-1302.
- Neunuebel JP, & Knierim JJ. (2012) Spatial firing correlates of physiologically distinct cell types of the rat dentate gyrus. *J. Neurosci.*, 32: 3848-3858.
- Nörenberg A, Hu H, Vida I, Bartos M, & Jonas P. (2010) Distinct nonuniform cable properties optimize rapid and efficient activation of fast-spiking GABAergic interneurons. *Proceedings of the National Academy of Sciences*, 107: 894-899.
- Nusser Z. (2009) Variability in the subcellular distribution of ion channels increases neuronal diversity. *Trends Neurosci.*, 32: 267-274.
- O'Keefe J. (1976) Place units in the hippocampus of the freely moving rat. *Exp. Neurol.*, 51: 78-109.
- O'keefe J, & Nadel L. (1978) *The hippocampus as a cognitive map*: Oxford: Clarendon Press.
- Ohno-Shosaku T, Maejima T, & Kano M. (2001) Endogenous cannabinoids mediate retrograde signals from depolarized postsynaptic neurons to presynaptic terminals. *Neuron*, 29: 729-738.
- Olton DS, Becker JT, & Handelmann GE. (1979) Hippocampus, space, and memory. *Behav. Brain Sci.*, 2: 313-322.
- Olton DS, & Paras BC. (1979) Spatial memory and hippocampal function. *Neuropsychologia*, 17: 669-682.

- Peng H, Ruan Z, Long F, Simpson JH, & Myers EW. (2010) V3D enables real-time 3D visualization and quantitative analysis of large-scale biological image data sets. *Nat. Biotechnol.*, 28: 348.
- Peng H, Tang J, Xiao H, Bria A, Zhou J, Butler V, Zhou Z, Gonzalez-Bellido PT, Oh SW, & Chen J. (2014) Virtual finger boosts three-dimensional imaging and microsurgery as well as terabyte volume image visualization and analysis. *Nature communications*, 5: 4342.
- Perkins KL. (2006) Cell-attached voltage-clamp and current-clamp recording and stimulation techniques in brain slices. *J. Neurosci. Methods*, 154: 1-18.
- Pernía-Andrade AJ, & Jonas P. (2014) Theta-gamma-modulated synaptic currents in hippocampal granule cells in vivo define a mechanism for network oscillations. *Neuron*, 81: 140-152.
- Pongs O, & Schwarz JR. (2010) Ancillary subunits associated with voltage-dependent K<sup>+</sup> channels. *Physiol. Rev.*, 90: 755-796.
- Pouille F, & Scanziani M. (2001) Enforcement of temporal fidelity in pyramidal cells by somatic feed-forward inhibition. *Science*, 293: 1159-1163.
- Pruunsild P, & Timmusk T. (2012) Subcellular localization and transcription regulatory potency of KCNIP/Calsenilin/DREAM/KChIP proteins in cultured primary cortical neurons do not provide support for their role in CRE-dependent gene expression. *J. Neurochem.*, 123: 29-43.
- Rall W, & Segev I. (1985). Space-clamp problems when voltage clamping branched neurons with intracellular microelectrodes. In *Voltage and patch clamping with microelectrodes* (pp. 191-215): Springer.
- Rhodes KJ, Carroll KI, Sung MA, Doliveira LC, Monaghan MM, Burke SL, Strassle BW, Buchwalder L, Menegola M, & Cao J. (2004) KChIPs and Kv4  $\alpha$  subunits as integral components of A-type potassium channels in mammalian brain. *J. Neurosci.*, 24: 7903-7915.

- Rollenhagen A, Sätzler K, Rodríguez EP, Jonas P, Frotscher M, & Lübke JH. (2007) Structural determinants of transmission at large hippocampal mossy fiber synapses. *J. Neurosci.*, 27: 10434-10444.
- Rolls E. (1990). Theoretical and neurophysiological analysis of the functions of the primate hippocampus in memory. Paper presented at the Cold Spring Harbor symposia on quantitative biology.
- Rolls ET. (1990) Functions of the primate hippocampus in spatial processing and memory. *Neurobiology of comparative cognition*: 339-362.
- Roth A, & Häusser M. (2001) Compartmental models of rat cerebellar Purkinje cells based on simultaneous somatic and dendritic patch-clamp recordings. *The Journal of physiology*, 535: 445-472.
- Royer S, Zemelman BV, Losonczy A, Kim J, Chance F, Magee JC, & Buzsáki G. (2012) Control of timing, rate and bursts of hippocampal place cells by dendritic and somatic inhibition. *Nat. Neurosci.*, 15: 769.
- Ruediger S, Vittori C, Bednarek E, Genoud C, Strata P, Sacchetti B, & Caroni P. (2011) Learning-related feedforward inhibitory connectivity growth required for memory precision. *Nature*, 473: 514.
- Salin PA, Scanziani M, Malenka RC, & Nicoll RA. (1996) Distinct short-term plasticity at two excitatory synapses in the hippocampus. *Proceedings of the National Academy of Sciences*, 93: 13304-13309.
- Sanguinetti MC, Johnson JH, Hammerland LG, Kelbaugh PR, Volkman RA, Saccomano NA, & Mueller AL. (1997) Heteropodatoxins: peptides isolated from spider venom that block Kv4. 2 potassium channels. *Mol. Pharmacol.*, 51: 491-498.
- Sasaki T. (2013) The axon as a unique computational unit in neurons. *Neurosci. Res.*, 75: 83-88.



- Scharfman HE. (1995) Electrophysiological evidence that dentate hilar mossy cells are excitatory and innervate both granule cells and interneurons. *J. Neurophysiol.*, 74: 179-194.
- Scharfman HE. (2007) The CA3 “backprojection” to the dentate gyrus. *Prog. Brain Res.*, 163: 627-637.
- Scheibel ME, Crandall PH, & Scheibel AB. (1974) The hippocampal-dentate complex in temporal lobe epilepsy: a Golgi study. *Epilepsia*, 15: 55-80.
- Schmidt-Hieber C, Jonas P, & Bischofberger J. (2007) Subthreshold dendritic signal processing and coincidence detection in dentate gyrus granule cells. *J. Neurosci.*, 27: 8430-8441.
- Scoville WB, & Milner B. (1957) Loss of recent memory after bilateral hippocampal lesions. *Journal of neurology, neurosurgery, and psychiatry*, 20: 11.
- Seikel E, & Trimmer JS. (2009) Convergent modulation of Kv4. 2 channel  $\alpha$  subunits by structurally distinct DPPX and KChIP auxiliary subunits. *Biochemistry*, 48: 5721-5730.
- Senzai Y, & Buzsáki G. (2017) Physiological properties and behavioral correlates of hippocampal granule cells and mossy cells. *Neuron*, 93: 691-704. e695.
- Shibata R, Misonou H, Campomanes CR, Anderson AE, Schrader LA, Doliveira LC, Carroll KI, Sweatt JD, Rhodes KJ, & Trimmer JS. (2003) A fundamental role for KChIPs in determining the molecular properties and trafficking of Kv4. 2 potassium channels. *J. Biol. Chem.*, 278: 36445-36454.
- Shu Y, Hasenstaub A, Duque A, Yu Y, & McCormick DA. (2006) Modulation of intracortical synaptic potentials by presynaptic somatic membrane potential. *Nature*, 441: 761.
- Sigworth F. (1995). Electronic design of the patch clamp. In *Single-channel recording* (pp. 95-127): Springer.

- Sivagnanam S, Majumdar A, Yoshimoto K, Astakhov V, Bandrowski A, Martone M, & Carnevale NT. (2015) Early experiences in developing and managing the neuroscience gateway. *Concurr Comput*, 27: 473-488. doi:10.1002/cpe.3283
- Sokolov EN. (1963) Higher nervous functions: The orienting reflex. *Annu. Rev. Physiol.*, 25: 545-580.
- Somogyi J, Baude A, Omori Y, Shimizu H, Mestikawy SE, Fukaya M, Shigemoto R, Watanabe M, & Somogyi P. (2004) GABAergic basket cells expressing cholecystinin contain vesicular glutamate transporter type 3 (VGLUT3) in their synaptic terminals in hippocampus and isocortex of the rat. *Eur. J. Neurosci.*, 19: 552-569.
- Somogyi P, & Klausberger T. (2005) Defined types of cortical interneurone structure space and spike timing in the hippocampus. *The Journal of physiology*, 562: 9-26.
- Spruston N, Jaffe DB, Williams SH, & Johnston D. (1993) Voltage-and space-clamp errors associated with the measurement of electrotonically remote synaptic events. *J. Neurophysiol.*, 70: 781-802.
- Squire LR. (2009) The legacy of patient HM for neuroscience. *Neuron*, 61: 6-9.
- Staley KJ, Otis TS, & Mody I. (1992) Membrane properties of dentate gyrus granule cells: comparison of sharp microelectrode and whole-cell recordings. *J. Neurophysiol.*, 67: 1346-1358.
- Stanley EF. (2016) The nanophysiology of fast transmitter release. *Trends Neurosci.*, 39: 183-197.
- Stefanelli T, Bertollini C, Lüscher C, Muller D, & Mendez P. (2016) Hippocampal somatostatin interneurons control the size of neuronal memory ensembles. *Neuron*, 89: 1074-1085.
- Stern JE, & Armstrong WE. (1996) Changes in the electrical properties of supraoptic nucleus oxytocin and vasopressin neurons during lactation. *J. Neurosci.*, 16: 4861-4871.

- Stevens CF, & Wang Y. (1995) Facilitation and depression at single central synapses. *Neuron*, 14: 795-802.
- Stevens JR. (1973) An anatomy of schizophrenia? *Arch. Gen. Psychiatry*, 29: 177-189.
- Strange B, & Dolan RJ. (1999) Functional segregation within the human hippocampus. *Mol. Psychiatry*, 4: 508-511.
- Stuart G, Dodt H, & Sakmann B. (1993) Patch-clamp recordings from the soma and dendrites of neurons in brain slices using infrared video microscopy. *Pflügers Archiv*, 423: 511-518.
- Szabadics J, & Soltesz I. (2009) Functional specificity of mossy fiber innervation of GABAergic cells in the hippocampus. *J. Neurosci.*, 29: 4239-4251.
- Szabadics J, Varga C, Brunner J, Chen K, & Soltesz I. (2010) Granule cells in the CA3 area. *J. Neurosci.*, 30: 8296-8307.
- Szabadics J, Varga C, Molnár G, Oláh S, Barzó P, & Tamás G. (2006) Excitatory effect of GABAergic axo-axonic cells in cortical microcircuits. *Science*, 311: 233-235.
- Szabó GG, Papp OI, Máté Z, Szabó G, & Hájos N. (2014) Anatomically heterogeneous populations of CB1 cannabinoid receptor-expressing interneurons in the CA3 region of the hippocampus show homogeneous input–output characteristics. *Hippocampus*, 24: 1506-1523.
- Szentagothai J, & Arbib MA. (1974) Conceptual models of neural organization. *Neurosci. Res. Program Bull.*
- Szoboszlay M, Lőrincz A, Lanore F, Vervaeke K, Silver RA, & Nusser Z. (2016) Functional properties of dendritic gap junctions in cerebellar Golgi cells. *Neuron*, 90: 1043-1056.
- Tang Y-Q, Liang P, Zhou J, Lu Y, Lei L, Bian X, & Wang K. (2013) Auxiliary KChIP4a suppresses A-type K<sup>+</sup> current through endoplasmic reticulum (ER) retention and promoting closed-state inactivation of Kv4 channels. *J. Biol. Chem.*, 288: 14727-14741.

- Tang Y-Q, Yang F, Zhou J, Zheng J, & Wang K. (2014) A-Type Kv4 Channel Closed-State Inactivation is Modulated by the Tetramerization Domain Interacting with Auxiliary KChIP4a. *Biophys. J.*, 106: 15a.
- Tashiro A, Dunaevsky A, Blazeski R, Mason CA, & Yuste R. (2003) Bidirectional regulation of hippocampal mossy fiber filopodial motility by kainate receptors: a two-step model of synaptogenesis. *Neuron*, 38: 773-784.
- Torborg CL, Nakashiba T, Tonegawa S, & McBain CJ. (2010) Control of CA3 output by feedforward inhibition despite developmental changes in the excitation–inhibition balance. *J. Neurosci.*, 30: 15628-15637.
- Toth K, Soares G, Lawrence JJ, Philips-Tansey E, & McBain CJ. (2000) Differential mechanisms of transmission at three types of mossy fiber synapse. *J. Neurosci.*, 20: 8279-8289.
- Urban NN, Henze DA, & Barrionuevo G. (2001) Revisiting the role of the hippocampal mossy fiber synapse. *Hippocampus*, 11: 408-417.
- Usovich MM, Sugimori M, Cherksey B, & Llinás R. (1992) P-type calcium channels in the somata and dendrites of adult cerebellar Purkinje cells. *Neuron*, 9: 1185-1199.
- Veres JM, Nagy GA, Vereczki VK, András T, & Hájos N. (2014) Strategically positioned inhibitory synapses of axo-axonic cells potently control principal neuron spiking in the basolateral amygdala. *J. Neurosci.*, 34: 16194-16206.
- Vida I, & Frotscher M. (2000) A hippocampal interneuron associated with the mossy fiber system. *Proceedings of the National Academy of Sciences*, 97: 1275-1280.
- Viney TJ, Lasztocki B, Katona L, Crump MG, Tukker JJ, Klausberger T, & Somogyi P. (2013) Network state-dependent inhibition of identified hippocampal CA3 axo-axonic cells in vivo. *Nat. Neurosci.*, 16: 1802.
- Vinogradova OS. (2001) Hippocampus as comparator: role of the two input and two output systems of the hippocampus in selection and registration of information. *Hippocampus*, 11: 578-598.

- Vyleta NP, Borges-Merjane C, & Jonas P. (2016) Plasticity-dependent, full detonation at hippocampal mossy fiber–CA3 pyramidal neuron synapses. *Elife*, 5: e17977.
- Vyleta NP, & Jonas P. (2014) Loose coupling between Ca<sup>2+</sup> channels and release sensors at a plastic hippocampal synapse. *Science*, 343: 665-670.
- Wan H, Aggleton JP, & Brown MW. (1999) Different contributions of the hippocampus and perirhinal cortex to recognition memory. *J. Neurosci.*, 19: 1142-1148.
- Wikenheiser AM, & Redish AD. (2015) Hippocampal theta sequences reflect current goals. *Nat. Neurosci.*, 18: 289.
- Wilson RI, Kunos G, & Nicoll RA. (2001) Presynaptic specificity of endocannabinoid signaling in the hippocampus. *Neuron*, 31: 453-462.
- Wilson RI, & Nicoll RA. (2001) Endogenous cannabinoids mediate retrograde signalling at hippocampal synapses. *Nature*, 410: 588.
- Winson J. (1978) Loss of hippocampal theta rhythm results in spatial memory deficit in the rat. *Science*, 201: 160-163.
- Wu HS, Sugihara I, & Shinoda Y. (1999) Projection patterns of single mossy fibers originating from the lateral reticular nucleus in the rat cerebellar cortex and nuclei. *J. Comp. Neurol.*, 411: 97-118.
- Xu X, Sun Y, Holmes TC, & López AJ. (2016) Noncanonical connections between the subiculum and hippocampal CA1. *J. Comp. Neurol.*, 524: 3666-3673.
- Zhou J, Tang Y, Zheng Q, Li M, Yuan T, Chen L, Huang Z, & Wang K. (2015) Different KChIPs compete for heteromultimeric assembly with pore-forming Kv4 subunits. *Biophys. J.*, 108: 2658-2669.
- Zola-Morgan S, Squire LR, Clower RP, & Alvarez-Royo P. (1991) Independence of memory functions and emotional behavior: separate contributions of the hippocampal formation and the amygdala. *Hippocampus*, 1: 207-220.

Zucca S, Griguoli M, Malézieux M, Grosjean N, Carta M, & Mulle C. (2017) Control of spike transfer at hippocampal mossy fiber synapses in vivo by GABAA and GABAB receptor-mediated inhibition. *J. Neurosci.*, 37: 587-598.

## 10. BIBLIOGRAPHY OF CANDIDATES PUBLICATIONS

*Publications related to this thesis:*

Neubrandt M<sup>1</sup>, **Oláh VJ**<sup>1</sup>, Brunner J, Szabadics J. (2017) Feedforward inhibition is randomly wired from individual granule cells onto CA3 pyramidal cells. *Hippocampus*, 27: 1034-1039.

<sup>1</sup> equal contribution

**Oláh VJ**, Lukacsovich D, Winterer J, Arszovszki A, Lőrincz A, Nusser Z, Földy C, Szabadics J. (2020) Functional specification of CCK+ interneurons by alternative isoforms of Kv4.3 auxiliary subunits. *eLife*, 2020;9:e58515.

**Oláh VJ**, Tarcsay G, Brunner J. Modelling the patch clamp experimental setup enables the recovery of native electrophysiological responses (*in preparation*)

*Other publications:*

Neubrandt M, **Oláh VJ**, Brunner J, Marosi EL, Soltesz I, Szabadics J. (2018) Single bursts of individual granule cells functionally rearrange feedforward inhibition. *Journal of Neuroscience*. 37: 1711-1724.

## 11. ACKNOWLEDGEMENTS

First, I would like to thank my supervisor, János Szabadics for all the energy and enthusiasm he put in to helping me not only to obtain invaluable theoretical and practical knowledge, but showing me importance of hard work and precision as well. János supervised my work with patience and devotion and both shaped and inspired my scientific thinking.

I would also like to thank all the present and past members of the Szabadics lab for creating a stimulating work environment, which allowed me to stay inspired and motivated throughout all the years of my undergraduate and graduate years. I express special gratitude towards János Brunner, who was constantly there for me in both scientific and person topics, and showed me a level of excellence which still defines the standards I aim for.

I would like to thank Dóra Hegedűs, Andrea Juszel, Dóra Kókay, Andrea Szabó and Antónia Arszovszki for their excellent and essential technical assistance.

I would also like to thank all my co-authors for the hard work they put into the projects we collaborated on: Máté Neubrandt, János Brunner, David Lukacsovich, Jochen Winterer, Antónia Arszovszki, Andrea Lőrincz, Zoltán Nusser, Csaba Földy, Gergely Tarcsay, Endre Marosi, Ivan Soltesz and Miklós Szoboszlay.

Furthermore, I would also like to thank all members of the Nusser and Makara lab, who both taught and inspired me during the Monday morning Journal Clubs.

Finally, I would like to express my gratitude towards my family, my father, mother and sister, who were constantly supporting me during my scientific career and my entire life. I would like to thank my wife, for the love and care she has for me, even during the hardest times. My wife and my two sons, Dávid and Fülöp are my constant sources of joy, and they give my life both meaning and purpose.